

---

**This manuscript is a preprint** and has been submitted for publication in **Computers & Geosciences**. Please note that, despite having undergone peer-review, the manuscript has yet to be formally accepted for publication. Subsequent versions of this manuscript may have slightly different content. If accepted, the final version of this manuscript will be available via the '*Peer-reviewed Publication DOI*' link on the right-hand side of this webpage. Please feel free to contact any of the authors; we welcome feedback.

---

# Small baseline InSAR time series analysis: unwrapping error correction and noise reduction

Zhang Yunjun<sup>a,\*</sup>, Heresh Fattahi<sup>b</sup>, Falk Amelung<sup>a</sup>

<sup>a</sup> Rosenstiel School of Marine and Atmospheric Science, University of Miami, Miami, Florida, USA

<sup>b</sup> Jet Propulsion Laboratory, California Institute of Technology, Pasadena, California, USA

\*Correspondence to Z. Yunjun, [yzhang@rsmas.miami.edu](mailto:yzhang@rsmas.miami.edu)

## Abstract

We present a review of small baseline interferometric synthetic aperture radar (InSAR) time series analysis with a new processing workflow and software implemented in Python, named MintPy (<https://github.com/insarlab/MintPy>). The time series analysis is formulated as a weighted least squares inversion. The inversion is unbiased for a fully connected network of interferograms without multiple subsets, such as provided by modern SAR satellites with small orbital tube and short revisit time. In the routine workflow, we first invert the interferogram stack for the raw phase time-series, then correct for the deterministic phase components: the tropospheric delay (using global atmospheric models or the delay-elevation ratio), the topographic residual and/or phase ramp, to obtain the noise-reduced displacement time-series. Next, we estimate the average velocity excluding noisy SAR acquisitions, which are identified using an outlier detection method based on the root mean square of the residual phase. The routine workflow includes three new methods to correct or exclude phase-unwrapping errors for two-dimensional algorithms: (i) the bridging method connecting reliable regions with minimum spanning tree bridges (particularly suitable for islands), (ii) the phase closure method exploiting

Authorship statement: HF and ZY developed the mathematical scope. ZY and HF developed the software. ZY and FA processed the data. ZY wrote the manuscript with the help of FA and HF. FA supervised the project.

24 the conservativeness of the integer ambiguity of interferograms triplets (well suited for highly  
25 redundant networks), and (iii) coherence-based network modification to identify and exclude  
26 interferograms with remaining coherent phase-unwrapping errors. We apply the routine  
27 workflow to the Galápagos volcanoes using Sentinel-1 and ALOS-1 data, assess the qualities of  
28 the essential steps in the workflow and compare the result with independent GPS measurements.  
29 We discuss the advantages and limitations of temporal coherence as a reliability measure,  
30 evaluate the impact of network redundancy on the precision and reliability of the InSAR  
31 measurement and its practical implication for interferometric pairs selection. A comparison with  
32 another open-source time series analysis software demonstrates the superior performance of the  
33 approach implemented in MintPy in challenging scenarios.

34

35 **Keywords:** InSAR; time series analysis; phase-unwrapping error; phase correction; Galápagos

## 36 **1. Introduction**

37 Time series Interferometric Synthetic Aperture Radar (InSAR) is a powerful geodetic technique  
38 to extract the temporal evolution of surface deformation from a set of repeated SAR images.  
39 Accuracy and precision of the retrieved surface displacement history are limited by the  
40 decorrelation of the SAR signal, the atmospheric delay and the phase-unwrapping error.  
41 Decorrelation is mainly caused by changes of the surface backscatter characteristics over time  
42 and by the non-ideal acquisition strategy of SAR satellites (Hanssen, 2001; Zebker and  
43 Villasenor, 1992). To overcome the limitations associated with early SAR satellites, including  
44 the relative long revisit time with non-regular acquisitions and the large orbit separation  
45 (baseline) between repeat acquisitions, two groups of InSAR time series techniques have been  
46 developed: persistent scatterer (PS) methods, which focus on the phase-stable point scatterers

47 with applications limited to cities and man-made infrastructures (Ferretti et al., 2001; Hooper et  
48 al., 2004), and distributed scatterer (DS) methods, which relaxed the strict limit on the phase  
49 stability and included areas that are affected by decorrelation through the exploitation of the  
50 redundant network of interferograms. The DS methods are the focus of this paper.

51  
52 Depending on the network of interferograms, DS methods can be divided into two categories.  
53 The first category uses the network of interferograms with small temporal and spatial baselines,  
54 known as small baseline subsets (SBAS) (Berardino et al., 2002; Schmidt and Bürgmann, 2003).  
55 These methods solve a system of linear observation equations using least squares estimation or  
56  $L^1$ -norm minimization (Lauknes et al., 2011). In cases of a non-fully connected network, singular  
57 value decomposition or a regularization constraint (López-Quiroz et al., 2009) is applied to find  
58 physically sound solutions. These methods require phase-unwrapped interferograms. In cases of  
59 low interferometric coherence, an integer least squares estimator can be applied to the wrapped  
60 interferograms, but this estimator is computationally expensive (Samiei-Esfahany et al., 2016).

61  
62 The second category uses the network consisting of all possible interferograms with full  
63 exploitation of the network redundancy (Ferretti et al., 2011; Fornaro et al., 2015; Guarnieri and  
64 Tebaldini, 2008). The solution is provided by the maximum likelihood estimator with  
65 performance close to the Cramér-Rao bound, the highest achievable precision (Guarnieri and  
66 Tebaldini, 2007), or by eigenvalue decomposition of the covariance matrix, which has been  
67 shown to be suboptimal for phase estimation (Ansari et al., 2018; Samiei-Esfahany et al., 2016).  
68 These methods swap the processing order and apply the network inversion as pre-processing  
69 steps for the estimation of optimal phases before phase unwrapping.

70

71 Despite the evident strengths of the full network approaches, especially the capability of phase  
72 estimation on low coherent areas, they remain computationally inefficient relative to the small  
73 baseline network approaches. Herein, we emphasize on the algorithmic efficiency; accordingly,  
74 we implemented a weighted least squares (WLS) estimator based on SBAS method with linear  
75 optimization. This process is known as phase linking or phase triangulation (Ansari et al., 2018;  
76 Ferretti et al., 2011) and referred hereafter as network inversion. The precision of network  
77 inversion depends on the temporal behavior of decorrelation: the small baseline network  
78 approaches provide higher precision when it is fast decorrelation, while the full network  
79 approaches provide higher precision when there is weak but long-term coherence (Ansari et al.,  
80 2017; Samiei-Esfahany et al., 2016).

81  
82 To separate the tropospheric delay from displacement, both PS and DS methods traditionally rely  
83 on spatial-temporal filtering of the phase time-series by taking into account their different  
84 frequency characteristics in time and space and assuming a temporal deformation model  
85 (Berardino et al., 2002; Ferretti et al., 2001), which can be unrealistic in complex natural  
86 environment such as volcanic deformation. Recent developments use global atmospheric models  
87 (GAMs), MERIS, MODIS or GPS wet delay (Jolivet et al., 2011; 2014; Li et al., 2009; Onn and  
88 Zebker, 2006; Yu et al., 2018), or empirical correlation between stratified tropospheric delay and  
89 topography (Bekaert et al., 2015; Doin et al., 2009; Lin et al., 2010) to correct interferograms  
90 before network inversion. Since the contribution of tropospheric delay is a deterministic  
91 component in InSAR phase observation, it is in principle preserved in the estimated phase time-  
92 series and therefore can be mitigated in the time-series domain after network inversion. Similar  
93 swaps of the processing sequence have been applied to phase unwrapping (Guarnieri and  
94 Tebaldini, 2008) and topographic residual correction (Fattahi and Amelung, 2013).

95

96 A disconnected network of interferograms with multiple interferogram subsets biases the time-  
97 series estimation, especially when there is no overlap in temporal or spatial baseline among  
98 interferogram subsets (López-Quiroz et al., 2009). For modern SAR satellites with improved  
99 orbital control and short revisit time such as Sentinel-1, the interferograms network can be easily  
100 fully connected, simplifying the network inversion into an unbiased WLS estimation of an  
101 overdetermined system. This robust inversion allows separating phase corrections from network  
102 inversion.

103

104 Here we present a new processing chain for InSAR time series analysis with phase corrections in  
105 the time-series domain, in contrast to the traditional interferogram domain. We refer the time-  
106 series domain as a series of phases indexed in time order with respect to a common reference  
107 acquisition, in contrast to the interferogram domain where the phases are indexed in acquisition  
108 pairs order. The basic idea is to split the time series analysis into two steps: i) invert network of  
109 interferograms for raw phase time-series and ii) separate tropospheric delay, topographic  
110 residual, timing error and orbital error from raw phase time-series to derive the displacement  
111 time-series. We also present two new methods to correct phase-unwrapping errors in  
112 interferograms unwrapped by two-dimensional phase unwrapping algorithms.

113

114 This paper is organized as follows. We first elaborate the theoretical basis of the weighted least  
115 squares estimator and evaluate the weight functions using simulated data (section 2). The phase-  
116 unwrapping error correction methods are presented in section 3. We then describe the processing  
117 chain (section 4) and apply it to data on the Galápagos volcanoes (section 5), followed by a  
118 discussion of results (section 6) and conclusions (section 7).

## 119 2. Review of weighted least squares estimator

### 120 2.1 Theoretical basis

121 We consider  $N$  SAR images of the same area acquired with similar imaging geometry at times  
122  $(t_1, \dots, t_N)$ , which are used to generate  $M$  interferograms coregistered to a common SAR  
123 acquisition, corrected for earth curvature and topography and spatially phase-unwrapped,  
124 referred to in the following as a stack of unwrapped interferograms. Building on Berardino et al.  
125 (2002), we model the network inversion problem as a system of  $M$  linear observation equations  
126 with the raw phase time-series  $\phi = [\phi^2, \dots, \phi^N]^T$  as the vector of the  $N - 1$  unknown  
127 parameters with reference acquisition at  $t_1$ .  $\phi$  corresponds to the observed physical path  
128 difference or range change from the SAR antenna to a ground target between each acquisition  
129 and the reference one, inclusive of all systematic components including ground deformation,  
130 atmospheric propagation delay and geometrical interferometric phase residuals such as those  
131 caused by inaccuracy in Digital Elevation Models (DEM). For each pixel, the functional model is  
132 described as:

133

$$134 \quad \Delta\phi = \mathbf{A}\phi + \Delta\phi_\varepsilon \quad (1)$$

135

136 where  $\Delta\phi = [\Delta\phi^1, \dots, \Delta\phi^M]^T$  is the interferometric phase vector with  $\Delta\phi^j$  the phase of the  $j$ th  
137 interferogram,  $\mathbf{A}$  is a  $M \times (N - 1)$  design matrix indicating the acquisition pairs used for  
138 interferograms generation. It consists of -1, 0 and 1 for each row with -1 for reference  
139 acquisition, 1 for secondary acquisition and 0 for the rest. An example to generate  $\mathbf{A}$  is provided  
140 in the Supplementary Information section S2.1.  $\Delta\phi_\varepsilon = [\Delta\phi_\varepsilon^1, \dots, \Delta\phi_\varepsilon^M]^T$  is the vector of  
141 interferometric phase residual that does not fulfill the zero phase closure of interferograms

142 triplets. It includes the decorrelation noise, phase contribution due to the change of dielectric  
 143 properties of ground scatterers such as soil moisture (De Zan et al., 2014; Morrison et al., 2011),  
 144 processing inconsistency such as filtering, multilooking, coregistration and interpolation errors  
 145 (Agram and Simons, 2015; Hanssen, 2001), and/or phase-unwrapping errors.

146

147 A fully connected network of interferograms corresponds to a full rank design matrix  $A$ . Then  
 148 the estimation of  $\phi$  can be treated as an unbiased weighted least squares inversion of an  
 149 overdetermined system. The solution of equation (1) can be obtained by minimizing the  $L^2$ -norm  
 150 of the residual phase vector  $\Delta\phi_\epsilon$  as:

151

$$152 \quad \hat{\phi} = \operatorname{argmin} \|\mathbf{W}^{1/2}(\Delta\phi - \mathbf{A}\phi)\|_2 = (\mathbf{A}^T \mathbf{W} \mathbf{A})^{-1} \mathbf{A}^T \mathbf{W} \Delta\phi \quad (2)$$

153

154 where  $\hat{\phi}$  is the estimated raw phase time-series and  $\mathbf{W}$  is a  $M \times M$  diagonal weight matrix,  
 155 discussed in detail below. The misfit between the estimated and true raw phase time-series is  
 156 given as:  $\hat{\phi}_\epsilon = \phi - \hat{\phi}$ . It's propagated from  $\Delta\phi_\epsilon$  through the network of interferograms.

157

158 An alternative objective function to solve equation (1) is minimizing the  $L^2$ -norm of the residual  
 159 of phase velocity of adjacent acquisitions (equation (16) in Berardino et al. (2002)).  
 160 Optimizations with both objective functions give nearly identical solutions for a fully connected  
 161 network. For a non-fully connected network, only the minimum-norm phase velocity gives a  
 162 physically sound solution (this is used by default in the software, although both objective  
 163 functions are supported).

164



165 For each pixel the quality of the inverted raw phase time-series can be assessed using the  
 166 temporal coherence  $\gamma_{temp}$  (Pepe and Lanari, 2006):

167

$$168 \quad \gamma_{temp} = \frac{1}{M} |\mathbf{H}^T \exp[j(\Delta\phi - \mathbf{A}\hat{\phi})]| \quad (3)$$

169

170 where  $j$  is the imaginary unit,  $\mathbf{H}$  is an  $M \times 1$  all-ones column vector. A threshold for temporal  
 171 coherence (0.7 by default) is used to select pixels with reliable network inversion. These pixels  
 172 are referred to in the following as the reliable pixels. Some limitations of this reliability measure  
 173 are discussed in section 6.4. For simplicity, in what follows we add the  $\hat{\phi}^1 = 0$  and refer to the  $N$   
 174 vector  $\hat{\phi} = [\hat{\phi}^1, \dots, \hat{\phi}^N]^T$  hereafter as the inverted raw phase time-series.

175

176 Since contributions of tropospheric delays, topographic residuals and/or phase ramps are  
 177 deterministic components in InSAR phase observations, they are preserved and therefore can be  
 178 mitigated in the time-series domain to obtain the displacement time-series:

179

$$180 \quad \phi_{dis}^i = \hat{\phi}^i - \hat{\phi}_{tropo}^i - \hat{\phi}_{geom}^i - \phi_{resid}^i \quad (4)$$

181

182 where  $i \in [1, \dots, N]$ ,  $\hat{\phi}_{tropo}^i$  represents the estimated phase contribution due to the difference in  
 183 propagation delay through the troposphere between  $t_i$  and  $t_1$ ;  $\hat{\phi}_{geom}^i$  represents the estimated  
 184 geometrical range difference from radar to target caused by the non-zero spatial baseline  
 185 between two orbits at  $t_i$  and  $t_1$ , including the topographic phase residual due to DEM error, phase  
 186 ramp due to orbital error, and possible phase ramp in range direction due to timing error of SAR  
 187 satellite;  $\phi_{resid}^i$  represents the residual phase, including the residual tropospheric delay,

188 uncorrected ionospheric delay, unmodeled non-tectonic ocean tidal loads (DiCaprio and Simons,  
189 2008), the remaining decorrelation noise and/or phase-unwrapping errors inherited from  $\Delta\phi_\varepsilon$ .

190

191 The phase introduced by orbital errors can be modeled as a linear or quadratic ramp. It can be  
192 estimated and removed using GPS (Tong et al., 2013), making InSAR measurement dependent  
193 on GPS. Considering its stochastic behavior and insignificant contribution to the uncertainty of  
194 velocity estimation compared with the atmospheric delay for most SAR satellites with precise  
195 orbits (Fattahi and Amelung, 2014), we do not correct orbital errors.

## 196 **2.2 Implicit assumptions**

197 The presented approach has two implicit simplifications. First, we assume that the residual term  
198  $\Delta\phi_\varepsilon$  in the phase triangulation functional model in equation (1) is zero or strictly controlled to be  
199 negligible during the least squares estimation, which might not be true due to non-  
200 conservativeness of phases in triplets of multilooked interferograms caused by the changes in the  
201 scattering mechanisms and which has been attributed to soil moisture variations between SAR  
202 acquisitions (De Zan et al., 2014), which is especially significant for L-band in densely vegetated  
203 areas (De Zan and Gomba, 2018) and discussed in section 3.2 and 5.3.2.

204

205 Second, we ignored the spatial correlation of decorrelation noise between pixels. This  
206 assumption is only satisfied when the SAR system resolution equals the pixel spacing. It is not  
207 the case in urban areas with strong reflecting structures, or in filtered interferograms with  
208 reduced resolution due to the cropped bandwidth (Agram and Simons, 2015).

### 209 2.3 Choice of weight function

210 Four different interferogram weighting strategies are implemented in the software. The first  
211 strategy is uniform or no weighting, as used in the classic SBAS approach (Berardino et al.,  
212 2002). In this case, the weight matrix  $\mathbf{W}$  is equal to the identity matrix and the WLS inversion  
213 simplifies into an ordinary least squares inversion. The other strategies are three different forms  
214 of coherence weighting, giving observations with high coherence (low variance) more weight  
215 than observations with low coherence (high variance).

216  
217 In the second strategy, interferograms are directly weighted by their spatial coherence at each  
218 pixel (Perissin and Wang, 2012; Pepe et al., 2015). The weight matrix takes the form:

$$219 \quad \quad \quad \mathbf{W} = \text{diag}\{\gamma^1, \dots, \gamma^M\} \quad (5)$$

220  
221 where  $\gamma^j$  is the spatial coherence of the  $j$ th interferogram.

222  
223  
224 In a third strategy, interferograms are weighted by the inverse of the phase variance (Tough et  
225 al., 1995). The matrix takes the form:

$$226 \quad \quad \quad \mathbf{W} = \text{diag}\{1/\sigma_{\Delta\phi^1}^2, \dots, 1/\sigma_{\Delta\phi^M}^2\} \quad (6)$$

227  
228  
229 where  $\sigma_{\Delta\phi^j}^2$  is the phase variance of the  $j$ th interferogram calculated through the integration of the  
230 phase probability distribution function (PDF). For distributed scatterers, the phase PDF is given  
231 by equation (S15) in the Supplementary Information section S3.2 (Tough et al., 1995) and used  
232 in the software. For persistent scatterers, the Cramér-Rao bound of variance is given directly by

233 equation (25) from Rodriguez and Martin (1992). The difference of phase PDFs between  
234 distributed scatterers and persistent scatterers tends to vanish when a large number of looks is  
235 applied (see supp. Fig. S1a). In practice, a lookup table is generated to facilitate the conversion  
236 from spatial coherence to phase variance (see supp. Fig. S1b).

237

238 The fourth strategy for interferogram weighting is the nonparametric Fisher information matrix  
239 (FIM), which accounts for the information loss due to noise and decorrelation, defined as  
240 (Samiei-Esfahany et al., 2016; Seymour and Cumming, 1994):

241

$$242 \quad \mathbf{W} = \text{diag}\left\{\frac{2L\gamma^{1^2}}{1-\gamma^{1^2}}, \dots, \frac{2L\gamma^{M^2}}{1-\gamma^{M^2}}\right\} \quad (7)$$

243

244 where  $L$  is the number of independent looks used for the estimation of spatial coherence  $\gamma^j$ . Note  
245 that FIM is identical to the inverse-variance matrix for persistent scatterers.

## 246 **2.4 Performance assessment of weight functions using data simulations**

247 We evaluate the performance of the different weight functions using simulated data to address  
248 the question of the optimum choice of weighting for phase estimation (Cao et al., 2015). Note  
249 that the maximum achievable precision is bounded by phase decorrelation, indicating the inverse  
250 of phase variance is the optimum choice theoretically (Guarnieri and Tebaldini, 2007).

### 251 **2.4.1 Simulation setting**

252 We generate the stack of interferograms for a sequential interferogram network with 10  
253 connections for each image. We use the temporal and perpendicular spatial baselines from the  
254 Sentinel-1 dataset of section 5. First, we specify an arbitrary temporal deformation model and  
255 generate the corresponding interferometric phases (Fig. 1a). Then we simulate the spatial

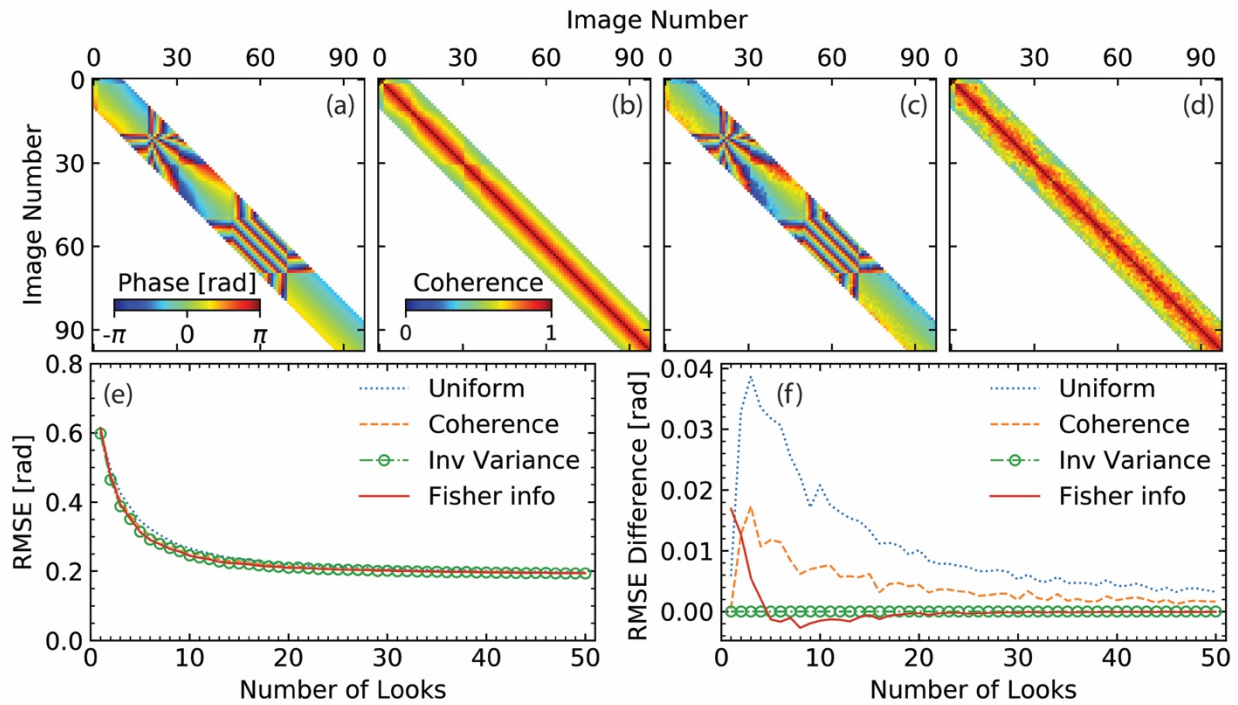
256 coherence of each interferogram using a decorrelation model with exponential decay for  
 257 temporal decorrelation (Fig. 1b) (Hanssen, 2001; Parizzi et al., 2009; Rocca, 2007; Zebker and  
 258 Villasenor, 1992). Next, we simulate the corresponding decorrelation phase noise for a given  
 259 number of looks  $L$  by generating a random number with the PDF of the interferometric phase of  
 260 a distributed scatterer with the given spatial coherence and number of looks and add it to the  
 261 noise-free phases (Fig. 1c, for  $9 \times 3$  looks). The construction of the spatial coherence from the  
 262 decorrelation model and the simulation of the decorrelation noise are described in detail in the  
 263 Supplementary Information section 3. Finally, we estimate the variance of the simulated  
 264 interferometric phase  $\sigma_{\Delta\phi}^2$  using windows of  $5 \times 5$  pixels and transform it to equivalent spatial  
 265 coherence using  $\gamma^j = 1/\sqrt{1 + 2 \cdot L \cdot \sigma_{\Delta\phi}^2}$  (Fig. 1d) (Agram and Simons, 2015). This coherence  
 266 is used to calculate the weights for the inversion.

#### 267 **2.4.2 Performance assessment**

268 To quantify the performance of the time-series estimator for the four different weight functions,  
 269 we evaluate the difference between the inverted phase  $\hat{\phi}^i$  and the specified, true phase  $\phi^i$  using a  
 270 root mean square error (RMSE) given as  $RMSE_{sim} = \sqrt{\sum_{i=1}^N (\hat{\phi}^i - \phi^i)^2 / (N - 1)}$ , where  $N$  is the  
 271 number of acquisitions ( $N = 98$ ).

272  
 273 Fig. 1e shows the mean RMSE for 10,000 realizations for the four different weighting  
 274 approaches as a function of the number of looks. To highlight differences, we also show the  
 275 difference in mean RMSE with respect to inverse-variance weighting (Fig. 1f). The three  
 276 weighting approaches outperform uniform weighting with coherence weighting performing  
 277 poorer than inverse-variance weighting (as shown by a positive difference in RMSE). Compared

278 to inverse-variance weighting, FIM weighting gives similar performance for more than 15 looks  
 279 and mixed performance for fewer looks. Similar mixed and unstable performance of FIM  
 280 weighting for small numbers of looks has also been observed at other simulated scenarios with  
 281 both higher and lower coherences (see supp. Fig. S2). This is different from a previous study  
 282 which supports the superiority of FIM over inverse-variance but considered only 25 looks (Fig. 8  
 283 of Samiei-Esfahany et al., 2016). Thus, we use the inverse of phase variance as the default  
 284 weight function in the software, although all four weighting strategies are supported.



285  
 286 **Figure 1.** Simulations for weight functions performance assessment. Upper panel: a simulated  
 287 network of interferograms. (a-b) simulated (true) unwrapped phase and spatial coherence; (c)  
 288 noise-containing unwrapped phase with  $L = 9 \times 3$ , (d) estimated coherence from the variance of  
 289 (c). Phase data are wrapped into  $[-\pi, \pi)$  for display. (e) Mean RMSE of 10,000 realizations of  
 290 inverted phase time-series as a function of  $L$  as the performance indicator for the four weight  
 291 functions. (f) Same as (e) but the difference in mean RMSE with respect to inverse-variance  
 292 weighting.

### 293 **3. Unwrapping error correction**

294 The inverted raw phase time-series can be potentially biased by wrong integer numbers of cycles  
295 ( $2\pi$  rad) added to the interferometric phase during the two-dimensional phase unwrapping, to  
296 which we refer simply as unwrapping errors. Here we describe two methods to automatically  
297 correct unwrapping errors using constraints from the space and time domain, respectively.

#### 298 **3.1 Bridging of reliable regions**

299 In the space domain, unwrapping errors introduce phase offsets among groups of pixels that are  
300 believed to be free of relative local unwrapping errors. Such a group of pixels are referred to as a  
301 reliable region (see Chen and Zebker (2002) for a quantitative definition). These regions usually  
302 have moderate to high spatial coherence and are separated from each other due to decorrelation  
303 or high deformation phase gradients.

304  
305 We assume that the phase differences between neighboring reliable regions are less than a one-  
306 half cycle ( $\pi$  rad) in magnitude. Then the task of unwrapping error correction is to determine the  
307 integer-cycle phase offsets to be added to each reliable region in order to align phase values  
308 among the regions. We present a bridging scheme to automatically connect reliable regions using  
309 tree searching algorithms. This is similar to region assembly in the secondary network in phase  
310 unwrapping (Carballo and Fieguth, 2002; Chen and Zebker, 2002), but in the tertiary level. To  
311 fulfill the assumption of smooth phase gradients between neighboring reliable regions, one could  
312 remove contributions from the troposphere, DEM error, deformation model, ramps before phase  
313 unwrapping and add them back in after correction. This method is particularly well suited for  
314 correcting unwrapping errors between regions separated by narrow decorrelated features such as  
315 rivers, narrow water bodies or steep topography.

### 316 3.1.1 Algorithm

317 The bridging scheme can be described as a three-step procedure for each interferogram. The first  
318 step is to identify reliable regions using the connected component information from the phase  
319 unwrapping algorithm such as SNAPHU (Chen and Zebker, 2001). Regions smaller than a  
320 preselected size are discarded. For each region, pixels on the boundaries are discarded using the  
321 erosion in morphological image processing with a preselected shape and size. The second step is  
322 to construct directed bridges to connect all reliable regions using the minimum spanning tree  
323 (MST) algorithm minimizing the total bridge length. We use the breadth-first algorithm to  
324 determine the order and direction (Cormen et al., 2009), starting from the largest reliable region.  
325 The third step is to estimate for each bridge the integer-cycle phase offset between the two  
326 regions. For that, we first estimate the phase difference as the difference in median values of  
327 pixels within windows of preselected size centered on the two bridge endpoints. The integer-  
328 cycle phase offset is the integer numbers of cycles to bring down the phase difference into  $[-\pi,$   
329  $\pi)$ . The algorithm has the option to estimate a linear or quadratic phase ramp based on the largest  
330 reliable region, which is removed from the entire interferogram before the offset estimation and  
331 added back after the correction (switched off by default).

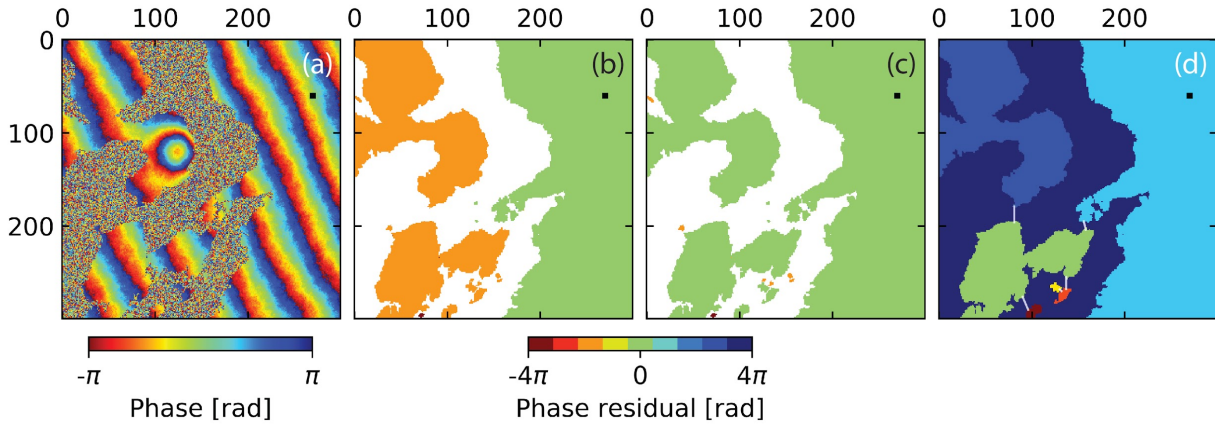
### 332 3.1.2 Simulated data

333 We demonstrate the bridging method using a simulated interferogram of western Kyushu, Japan  
334 (Fig. 2), a region with multiple islands, considering decorrelation noise, ground displacement,  
335 tropospheric turbulence and phase ramps. We specify spatial coherence of 0.6 and 0.001 for  
336 pixels on land and water respectively and simulate the corresponding decorrelation noise (see  
337 section 2.4.1). The simulation for the other phase contributions is shown in supp. Fig. S3. We  
338 wrap the simulated phase (Fig. 2a), unwrap using the SNAPHU algorithm, and apply the  
339 bridging method. Fig. 2b and c show the phase residual  $\Delta\phi_\varepsilon^i$  after phase unwrapping



340 (unwrapping error) without and with unwrapping error correction, respectively. The reduction in  
 341 unwrapping errors (from  $-2\pi$  rad in orange shadings for the islands on the west in Fig. 2b to 0 rad  
 342 in green shadings in Fig. 2c) demonstrates that the method works.

343



344

345 **Figure 2.** Simulation of unwrapping error correction using the bridging method. (a) Simulated  
 346 wrapped phase, (b and c) phase residual (unwrapping error) without and with unwrapping error  
 347 correction, respectively. (d) Reliable regions and bridges (white solid lines) generated based on  
 348 connected components from SNAPHU. White shadings in (b and c): areas not considered by the  
 349 connected components. Black squares represent the reference point.

### 350 3.2 Phase closure of interferograms triplets

351 In the time domain, unwrapping errors could break the consistency of triplets of interferometric  
 352 phases (Biggs et al., 2007). The closure phase is the cyclic product of the unwrapped  
 353 interferometric phases:

354

$$355 C^{ijk} = \Delta\phi^{ij} + \Delta\phi^{jk} - \Delta\phi^{ik} \quad (8)$$

356

357 where  $\Delta\phi^{ij}$ ,  $\Delta\phi^{jk}$  and  $\Delta\phi^{ik}$  are three unwrapped interferometric phases generated from the SAR  
 358 acquisitions at  $t_i$ ,  $t_j$  and  $t_k$ . The integer ambiguity of the closure phase is given as:

359

$$360 \quad C_{int}^{ijk} = (C^{ijk} - \text{wrap}(C^{ijk})) / (2\pi) \quad (9)$$

361

362 where *wrap* is an operator to wrap the input number into  $[-\pi, \pi)$ . A triplet without unwrapping

363 errors has  $C_{int}^{ijk} \equiv 0$ . The number of triplets with non-zero  $C_{int}^{ijk}$  among all triplets is given as:

364  $T_{int} = \sum_{i=1}^T (C_{int}^i \neq 0)$ , where  $T$  is the number of triplets ( $T_{int} \leq T$ ).  $T_{int}$  can be used to detect

365 unwrapping errors.

366

367 Fig. 3 shows the characteristics of unwrapping errors in the closure phase from the Sentinel-1

368 dataset (stack of multilooked unwrapped interferograms) of section 5. The non-zero  $C^{ijk}$  in Fig.

369 3a and b are caused by the interferometric phase residuals (see equation (1)), whereas the non-

370 zero  $C_{int}^{ijk}$  in Fig. 3c are caused by unwrapping errors. Fig. 3d and e shows the distribution of

371  $T_{int}$ . On Isabela island, pixels in non-vegetated area have  $T_{int} = 0$  (dark blue in Fig. 3d) and are

372 free of unwrapping errors; while pixels in vegetated area, such as the light-blue to green area on

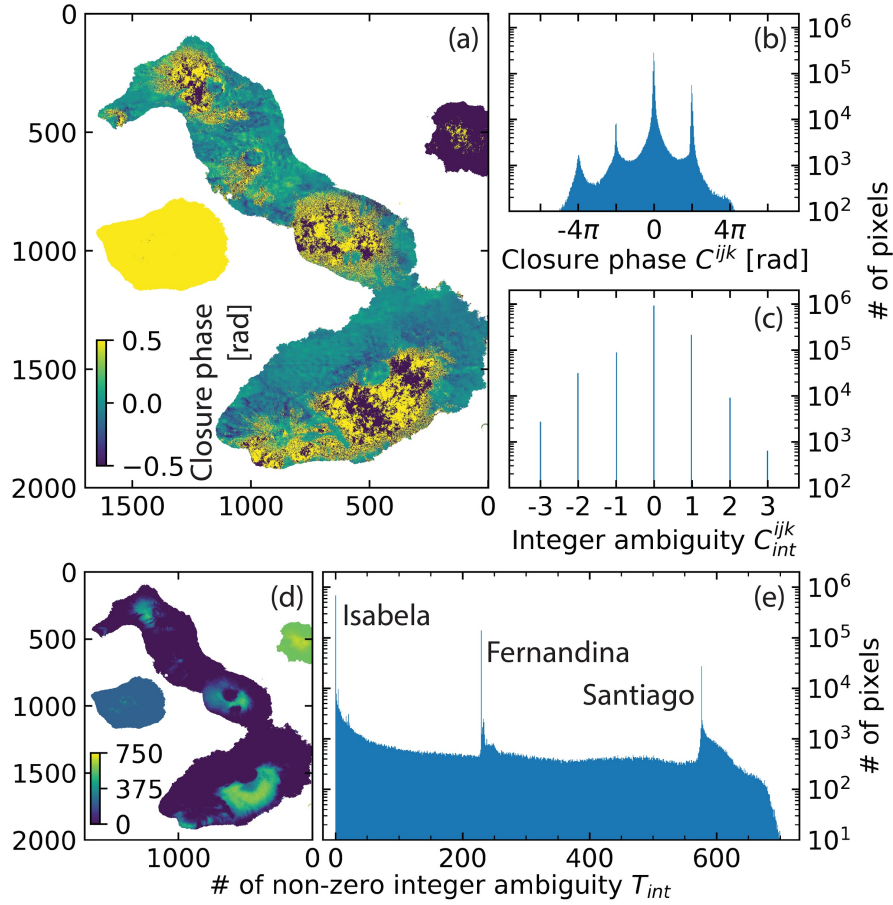
373 Sierra Negra's south flank in Fig. 3d, have wide-distributed  $T_{int}$  values, indicating random

374 unwrapping errors, which are difficult to be corrected. On Fernandina and Santiago island, most

375 pixels share the common  $T_{int}$  of 229 and 576 out of 940 triplets, respectively, indicating

376 unwrapping errors and can be corrected.

377



378

379 **Figure 3.** Characteristics of unwrapping errors in the closure phase. (a) Map and (b) histogram

380 of  $C^{ijk}$  for the interferogram triplet generated from three Sentinel-1 images acquired at 7 March

381 2015, 19 March 2015 and 6 May 2015 from descending track 128. (c) Histogram of  $C_{int}^{ijk}$  for the

382 closure phase in (a and b). The non-zero  $C_{int}^{ijk}$  are caused by unwrapping errors. (d) Map and (e)

383 histogram of  $T_{int}$  (the 475 interferograms from the 98 Sentinel-1 images can be combined to 940

384 triplets). The spikes in (e) at 229 and 576 indicate the unwrapping error in Fernandina and

385 Santiago island respectively.

386

387 Several attempts have been pursued to evaluate the phase unwrapping and correct the

388 unwrapping errors using the close phase information. Hussain et al. (2016) use the close phase to

389 adjust the cost in the three-dimensional phase unwrapping procedure iteratively. Biggs et al.  
 390 (2007) visually identify and correct the unwrapping errors by manually adding the integer-cycle  
 391 phase offsets to badly unwrapped regions of pixels. Built on this idea, we develop an algorithm  
 392 to automatically detect and correct the unwrapping errors in the network of interferograms.

### 393 3.2.1 Algorithm

394 For a redundant network of interferograms, the temporal consistency of the integer ambiguities  
 395 of unwrapped interferometric phases can be expressed for each pixel as:

396

$$397 \quad \mathbf{C}\mathbf{U} + (\mathbf{C}\Delta\phi - \text{wrap}(\mathbf{C}\Delta\phi)) / (2\pi) = 0 \quad (10)$$

398

399 where  $\mathbf{C}$  is a  $T \times M$  design matrix of all possible interferogram triplets,  $\mathbf{U}$  is a  $M \times 1$  vector of  
 400 integer numbers for cycles required to meet the consistency of the interferometric phases. An  
 401 example of  $\mathbf{C}$  is provided in the Supplementary Information section S2.2. Note that equation (10)  
 402 can be ill-posed and does not always has a unique solution, especially when  $T < M$ . Thus,  
 403 regularization is required to obtain an optimal solution. We assume that the solution is more  
 404 likely to be small than large, and more likely to be sparse than dense. Accordingly, we apply the  
 405  $L^1$ -norm regularized least squares optimization (Andersen et al., 2011; Xu, 2017), which is also  
 406 known as least absolute shrinkage and selection operator (LASSO), to obtain the solution as:

407

$$408 \quad \hat{\mathbf{U}} = \text{argmin} \|\mathbf{C}\mathbf{U} + (\mathbf{C}\Delta\phi - \text{wrap}(\mathbf{C}\Delta\phi)) / (2\pi)\|_2 + \alpha \|\mathbf{U}\|_1 \quad (11)$$

409

410 where  $\alpha = 0.01$  is a nonnegative parameter for the trade-off between the  $L^1$  and  $L^2$ -norm term,  
 411 with value chosen based on simulations with various values of  $\alpha$  (see supp. Fig. S4). The

412 corrected unwrapped interferometric phase is given as:  $\Delta\phi_c = \Delta\phi + 2\pi \cdot \text{round}(\hat{U})$ , where  
413 *round* is an operator to round the input number to the nearest integer.

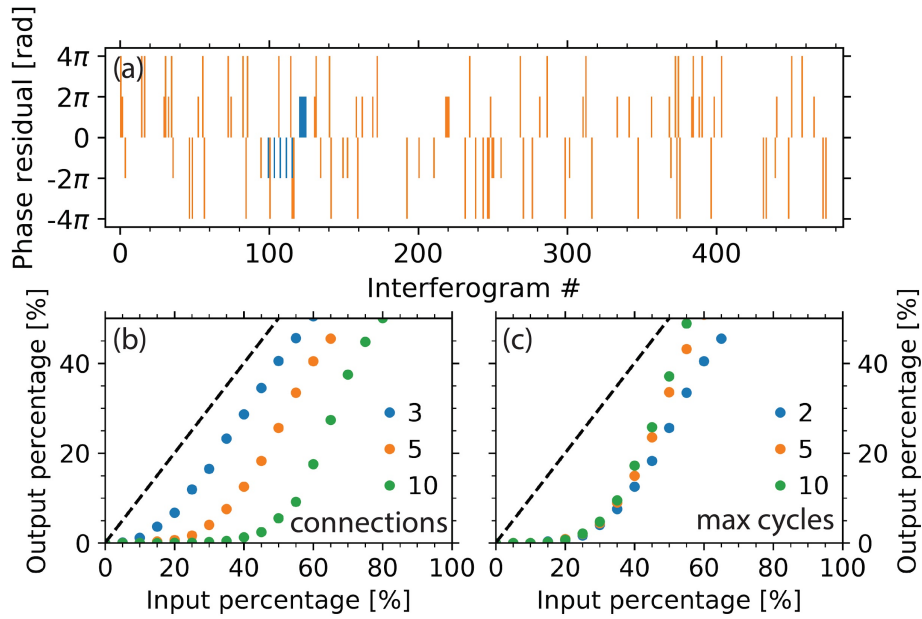
### 414 3.2.2 Simulated data

415 We demonstrate the phase closure method using a simulated interferogram stack for one pixel  
416 (Fig. 4). We first simulate the decorrelation noise and ground deformation (see section 2.4.1) for  
417 an interferogram network with 5 sequential connections using the temporal and perpendicular  
418 spatial baselines from the Sentinel-1 dataset of section 5 below. Then we randomly select 20%  
419 interferograms to add unwrapping errors with randomly selected cycles (maximum of 2) of  
420 magnitude and randomly selected sign (orange bars in Fig. 4a). Next, we apply the phase closure  
421 method and compare the unwrapping errors before and after the correction, as shown in orange  
422 and blue bars in Fig. 4a, respectively. The method decreases the number of interferograms  
423 affected by unwrapping errors from 20% to 2% and reduces the magnitude of the remaining  
424 unwrapping errors (Fig. 4a). We note that the method could potentially introduce new  
425 unwrapping errors to the unwrapped interferograms (blue bars in Fig. 4a where there is no  
426 orange bar).

427

428 We evaluate the performance of the phase closure method by comparing the input and output  
429 percentages of interferograms with unwrapping errors (before and after correction), considering  
430 different input percentages and redundancies of the interferogram network. Fig. 4b shows for  
431 100 realizations the mean output percentage after correction versus the input percentage for  
432 networks with 3, 5 and 10 sequential interferograms. For 5 connections (orange dots in Fig. 4b),  
433 the method fully corrects unwrapping errors if there are less than 20% of interferograms affected;  
434 then the improvement slows down with the increasing input percentage until it reaches a turning  
435 point of 35%, beyond which the improvement is marginal. The maximum input percentages with

436 full correction for 3, 5 and 10 connections are at 5, 20 and 35%, respectively, indicating better  
 437 performance for more redundant networks. Fig. 4c shows the performances for 5 connections  
 438 network with maximum of 2, 5 and 10 cycles of unwrapping errors. The similarity before 30%  
 439 shows that the method is robust for various magnitudes of unwrapping errors. Thus, we conclude  
 440 that the phase closure method is suitable for highly redundant networks of interferograms with  
 441 not too many unwrapping errors.

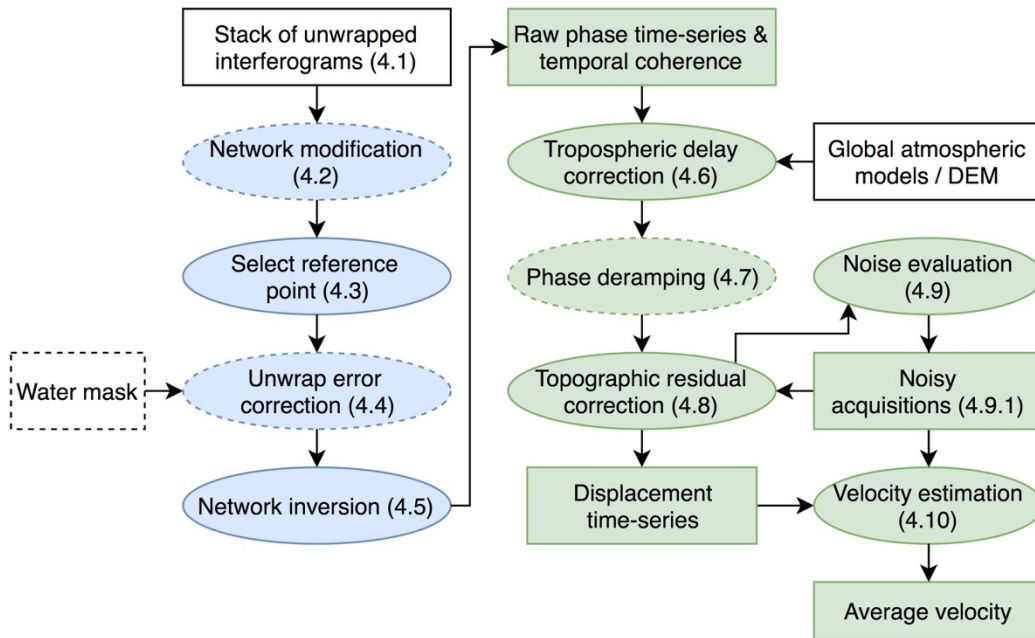


442  
 443 **Figure 4.** Simulations of unwrapping error correction using the phase closure method. (a)  
 444 Unwrapping errors in interferograms before (orange bars, account for 20%) and after  
 445 correction (blue bars, account for 2%). A network of interferograms with 5 sequential  
 446 connections is used. A maximum of 2 cycles of unwrapping errors are added randomly. (b) Mean  
 447 output percentage of 100 realizations of interferograms with unwrapping errors versus the input  
 448 percentage, with a fixed maximum of 2 cycles of unwrapping errors and color coded by network  
 449 redundancy. (c) Same as (b) but with a fixed network of 5 connections and color coded by  
 450 maximum unwrapping error magnitudes.

## 451 4. Workflow of InSAR time series analysis

452 We have implemented a generic routine processing workflow for InSAR time series analysis  
 453 from a stack of unwrapped interferograms to displacement time-series (Fig. 5). The workflow  
 454 consists of two main blocks: (i) correcting unwrapping errors and inversion for the raw phase  
 455 time-series (blue ovals in Fig. 5), and (ii) correcting for phase contributions from different  
 456 sources to obtain the displacement time-series (green ovals in Fig.5). It includes some optional  
 457 steps, which are switched off by default (marked by dashed boundaries in Fig. 5), here we  
 458 present the workflow in its most complete form. Configuration parameters for each step are  
 459 initiated with default values in a customizable text file ([link on GitHub](#)).

460



461

462 **Figure 5.** Routine workflow of InSAR time series analysis. Blue ovals: steps in the interferogram  
 463 domain including unwrapping error correction and network inversion; green ovals: steps in the  
 464 time-series domain including phase corrections for the tropospheric delay, phase ramps, and  
 465 topographic residuals. White rectangles: input data. Green rectangles: output data. Optional  
 466 steps/data are marked by dashed boundaries.

#### 467 **4.1 Starting point: Stack of unwrapped interferograms**

468 As described above, the starting point is a stack of phase-unwrapped interferograms coregistered  
469 to a common SAR acquisition, corrected for earth curvature and topography. We currently  
470 support interferogram stacks produced by ISCE, GAMMA and ROI\_PAC software (Rosen et al.,  
471 2004; Rosen et al, 2012; Werner et al., 2000).

#### 472 **4.2 Network modification**

473 In order to exclude outliers affected by coherent pixels with unwrapping errors, the software  
474 provides network modification to exclude affected interferograms if the spatially averaged  
475 coherence for an area of interest falls below a predefined threshold value (switched off by  
476 default). This is similar to Chaussard et al. (2015) excluding interferograms with a low  
477 percentage of high coherent pixels. An extra constraint could be applied to keep those  
478 interferograms if they are part of the MST network providing the maximum spatially averaged  
479 coherence (Perissin and Wang, 2012) to ensure a fully connected network (switched on by  
480 default). The approach is referred to as coherence-based network modification. This is based on  
481 the empirical observation that reliable regions with unwrapping errors are usually surrounded by  
482 decorrelated areas. The default area of interest is all pixels on land, a customized area of interest  
483 including the decorrelated areas around the reliable regions is usually more effective. The  
484 software also supports other approaches for network modification, such as thresholds of the  
485 temporal and spatial baselines, maximum number of connections for each acquisition, and  
486 exclusion of specific acquisitions, interferograms.

#### 487 **4.3 Reference selection in space**

488 The reference pixel is selected randomly among the pixels with high average spatial coherence  
489 ( $\geq 0.85$  by default) or can be specified using prior knowledge of the study area. The reference



490 pixel should be (i) located in a coherent area; (ii) not affected by strong atmospheric turbulence  
491 such as ionospheric streaks and (iii) close to and with similar elevation as the area of interest to  
492 minimize the impact of the spatially correlated atmospheric delay. For example, Chaussard et al.  
493 (2013) studied volcano deformation using reference points on inactive, neighboring volcanoes.

#### 494 **4.4 Unwrapping error correction**

495 Three methods are available to possibly detect and correct unwrapping errors in the stack of  
496 interferograms. The first method is bridging as described in section 3.1. This method is well  
497 suited for unwrapping errors occurred among islands or on areas separated by steep topography.  
498 The second method is based on the phase closure as described in section 3.2. It's well suited for  
499 unwrapping errors in a highly redundant network of interferograms. Both methods are operated  
500 in the region level, thus are efficient. The third approach is to apply both methods, bridging  
501 followed by phase closure, as they exploit aspects of unwrapping errors in space and time  
502 domain, respectively. The default is no unwrapping error correction.

#### 503 **4.5 Network inversion**

504 The raw phase time-series is solved by minimizing the interferometric phase residual  $\Delta\phi_\varepsilon$ . Then,  
505 the temporal coherence is computed based on equation (3) and used to generate a temporal  
506 coherence mask for pixels with reliable time-series estimation with a predefined threshold (0.7  
507 by default). Pixels in shallow and water bodies are masked out if shallow mask and water body  
508 mask are available.

##### 509 **4.5.1 Phase masking**

510 In order to exclude outliers affected by decorrelation, the software provides masking options  
511 (switched off by default) based on the spatial coherence (default threshold of 0.4) or using the  
512 connected component information from phase unwrapping. Note that masking based on spatial

513 coherence is equivalent to weighting with a step function, thus phase masking is recommended  
514 only when unweighted inversion is applied.

515

516 After masking, the pixels may have different numbers of interferograms. We use not only the  
517 pixels that are coherent in all interferograms (Agram and Simons, 2015), but relax the pixel  
518 selection criterion and also use pixels with fewer interferograms as long as a predefined  
519 minimum number of interferograms is available for each SAR acquisition (1 by default). Note  
520 that with this pixel selection strategy after masking, the network inversion result is not sensitive  
521 to the few very low coherent interferograms in a redundant network, giving robust and consistent  
522 spatial coverage.

#### 523 **4.6 Tropospheric delay correction**

524 Two different approaches for tropospheric delay correction are available. In the first approach,  
525 the tropospheric delay is estimated using Global Atmospheric Models (GAMs). The estimated  
526 relative double path tropospheric delay at  $t_i$  between a given pixel  $p$  and a reference pixel is  
527 given in radians as:

528

$$529 \quad \hat{\phi}_{tropo}^i(p) = (\delta L_p^i - \delta L_p^1) \frac{4\pi}{\lambda} - (\delta L_{ref}^i - \delta L_{ref}^1) \frac{4\pi}{\lambda} \quad (12)$$

530

531 where  $i \in [1, \dots, N]$ ,  $\delta L_x^i$  is the integrated absolute single path tropospheric delay at  $t_i$  on pixels  $x$   
532 in meters in satellite line-of-sight (LOS) direction ( $\delta L_p^1$  for  $t_1$ ) and  $\lambda$  is the radar wavelength in  
533 meters. The supported datasets include ERA-5 and ERA-Interim from European Center for  
534 Medium-Range Weather Forecast, NARR (North American Regional Reanalysis) from NOAA

535 and MERRA (Modern-Era Retrospective Analysis) from NASA (applied by default, using  
536 PyAPS software from Jolivet et al. (2011; 2014)).

537

538 The second approach is based on the empirical linear relationship between the InSAR phase  
539 delay and elevation (Doin et al., 2009) which in areas with strong topographic variations  
540 sometimes outperforms corrections using GAMs. On the other hand, the empirical approach  
541 cannot distinguish between the stratified tropospheric delay and the ground deformation  
542 correlated with topography such as at volcanoes.

#### 543 **4.7 Phase deramping**

544 Phase ramps are caused by residual tropospheric and ionospheric delays and to a lesser extent, by  
545 orbital errors. For long spatial wavelength deformation signals such as interseismic deformation,  
546 ramps should not be removed. Instead, physical and statistical approaches should be applied to  
547 correct the ionospheric delay (Fattahi et al., 2017; Gomba et al., 2016; Liang et al., 2018) and/or  
548 assess the measurement uncertainties (Fattahi and Amelung, 2014; 2015; Fattahi et al., 2017).  
549 For short spatial wavelengths deformation signals such as volcanic deformation, landslides, and  
550 urban subsidence it is recommended to estimate and then to remove linear or quadratic ramps  
551 from the displacement time-series at each acquisition on the reliable pixels (default is no ramp  
552 removal).

#### 553 **4.8 Topographic residual correction**

554 The systematic topographic phase residual caused by a DEM error is estimated based on the  
555 proportionality with the perpendicular baseline time-series (Fattahi and Amelung, 2013). The  
556 original method assumes a cubic temporal deformation model, which is not able to capture high-  
557 frequency displacement components, such as offsets caused by earthquakes or volcanic

558 eruptions. The software provides options to account for permanent displacement jumps using  
 559 step functions (Hetland et al., 2012) and to generalize polynomial functions with a user-defined  
 560 polynomial order  $N_{poly}$ . The DEM error  $z_\varepsilon$  for each pixel is then given by:

$$562 \quad \hat{\phi}^i - \hat{\phi}_{tropo}^i = \left( \frac{B_\perp^i}{r \sin(\theta)} z_\varepsilon + \sum_{k=0}^{N_{poly}} c_k (t_i - t_1)^k / k! + \sum_{l \in I_s} s_l H(t_i - t_l) \right) \frac{-4\pi}{\lambda} + \phi_{resid}^i \quad (13)$$

563  
 564 where  $i \in [1, \dots, N]$ ,  $B_\perp^i$  is the perpendicular baseline between  $t_i$  and  $t_1$ ,  $r$  is the slant range  
 565 between the target and the radar antenna,  $\theta$  is the incidence angle,  $H(t_i - t_l)$  is a Heaviside step  
 566 function centered at  $t_l$ ,  $I_s$  is a set of indices describing offsets at specific prior selected times.  $z_\varepsilon$ ,  
 567  $c_k$  and/or  $s_l$  are the unknown parameters, which can be estimated by minimizing the  $L^2$ -norm of  
 568 residual phase time-series  $\phi_{resid} = [\phi_{resid}^1, \dots, \phi_{resid}^N]^T$ . An example design matrix and the  
 569 numerical solution of least squares estimation are provided in the Supplementary Information  
 570 section 2.3. The necessity of the step function(s) in the presence of deformation jump(s) is  
 571 demonstrated in supp. Fig. S5 (default is no step function with  $N_{poly} = 2$ ).

572  
 573 As we are interested in the estimation of  $z^\varepsilon$ , the assumed deformation model does not need to be  
 574 a comprehensive representation of the deformation processes. Note, however, that equation (13)  
 575 offers the possibility to parametrize the geophysical processes using more complex models, e.g.  
 576 using the regularization functions from Hetland et al. (2012).

#### 577 **4.9 Residual phase for noise evaluation**

578 The estimate of residual phase  $\hat{\phi}_{resid}$ , a by-product of equation (13), is the phase component that  
 579 can neither be corrected nor be modeled as ground deformation, thus, is used to characterize the

580 noise level of the InSAR time-series. For each SAR acquisition, we compute the root mean  
 581 square (RMS) of the residual phase as:

582

$$583 \quad RMS^i = \sqrt{\frac{1}{N_\Omega} \sum_{p \in \Omega} (\hat{\phi}_{resid}^i(p) \cdot \frac{\lambda}{-4\pi})^2} \quad (14)$$

584

585 where  $i = [1, \dots, N]$ ,  $\hat{\phi}_{resid}^i(p)$  represent the residual phase at  $t_i$  for pixel  $p$ ,  $\Omega$  is the set of  
 586 reliable pixels selected based on temporal coherence during the network inversion with the total  
 587 number of  $N_\Omega$ . Due to the inadequate knowledge of the long spatial wavelength phase component  
 588 in  $\hat{\phi}_{resid}$ , we focused on the noise evaluation of the short spatial wavelength phase component  
 589 only, including residual tropospheric turbulence, uncorrected ionospheric turbulence, and  
 590 remaining decorrelation noise. Therefore, we remove a quadratic ramp from the residual phase of  
 591 each acquisition before calculating the RMS (Lohman and Simons, 2005).

#### 592 **4.9.1 Identifying noisy SAR acquisitions**

593 Assuming the residual tropospheric delay in  $\hat{\phi}_{resid}$  is stochastic and Gaussian distributed in time  
 594 (Fattahi and Amelung, 2015), we can treat the noisy SAR acquisitions contaminated by severe  
 595 atmospheric turbulence as outliers. Following Rousseeuw and Hubert (2011), we calculate the  
 596 median absolute deviation (MAD) value and mark a SAR acquisition as noisy if its RMS value is  
 597 larger than the predefined cutoff (3 MADs by default giving 99.7% confidence). Note that we  
 598 assume a zero-mean value for the distribution considering the positive nature of RMS. The  
 599 automatically identified noisy acquisitions will be excluded in the topographic residual  
 600 estimation (during re-run) and velocity estimation.

#### 601 **4.9.2 Selecting the optimal reference date**

602 The SAR acquisition with the smallest RMS value can be interpreted as the date with minimum  
603 atmospheric turbulence and is used as the reference date. We note that changing the reference is  
604 equivalent to adding a constant to the displacement time series, which does not change the  
605 velocity or any other information derived from the displacement time series.

#### 606 **4.10 Average velocity estimation**

607 For applications with interest on the deformation rate, the velocity  $v$  is estimated as the slope of  
608 the best fitting line to the displacement time-series, given as  $\phi_{dis}^i \cdot \lambda / (-4\pi) = v \cdot t_i + c, i =$   
609  $1, \dots, N$ , where  $c$  is an unknown offset constant. Noisy SAR acquisitions are excluded by default  
610 during the estimation. The standard deviation of the estimated velocity is given by equation (10)  
611 from Fattahi and Amelung (2015).

### 612 **5. Application to Galápagos volcanoes, Ecuador**

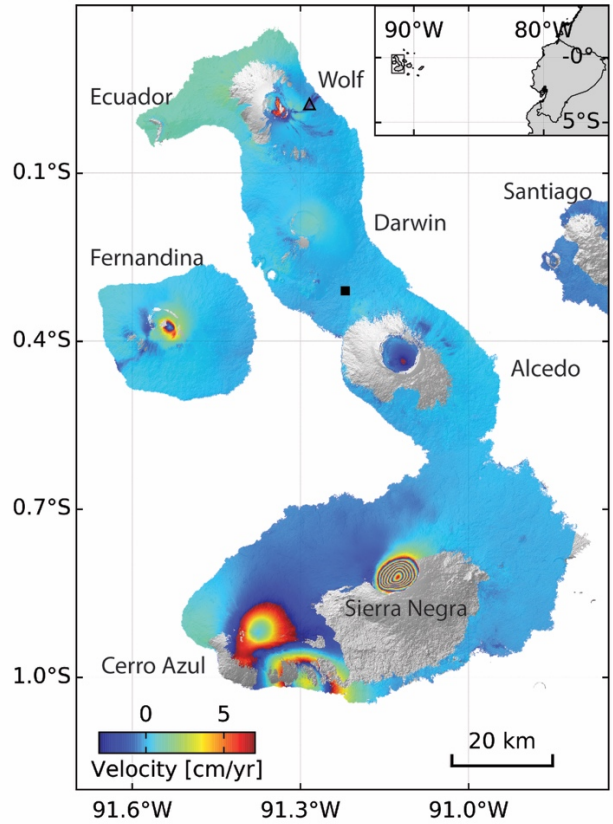
613 We apply the routine workflow outlined in the previous section to the Western Galápagos  
614 Islands, Ecuador, located around 1000 km west of Ecuador mainland (Fig. 6 inset). We consider  
615 interferogram stacks from the Sentinel-1 and ALOS-1 satellite. For Sentinel-1 (we consider the  
616 December 2014 to June 2018 period) we use the stack Sentinel processor (Fattahi et al, 2016)  
617 within ISCE (Rosen et al, 2012) for processing the stack of interferograms; we pair each SAR  
618 image with its five nearest neighbors back in time (sequential network); we multilook each  
619 interferogram by 15 and 5 looks in range and azimuth direction respectively, filter using a  
620 Goldstein filter with a strength of 0.2 ([configuration file](#)). For ALOS-1 we use ROI\_PAC (Rosen  
621 et al., 2004) for processing the stack of interferograms; we select interferometric pairs with small  
622 temporal (1800 days) and spatial baselines (1800 m) and with over 15% of Centroid doppler

623 frequency overlap in azimuth direction; we multilook each interferogram by 8 and 16 looks in  
624 range and azimuth direction respectively, filter using a Goldstein filter with a strength of 0.5 and  
625 an adaptive smoothing with a width of 4 pixels ([configuration file](#)). We remove the topographic  
626 phase component using SRTM DEM (SRTMGL1, ~30m, 1 arc second with void-filled; Farr et  
627 al., 2007). The interferograms are phase-unwrapped using the minimum cost flow method (Chen  
628 and Zebker, 2001). In the routine workflow for the Sentinel-1 dataset we correct unwrapping  
629 errors using the bridging and phase closure methods. In the routine workflow for the ALOS-1  
630 dataset we exclude interferograms using coherence-based network modification with a  
631 customized area of interest (blue rectangle in Fig. 10b) and correct unwrapping errors using the  
632 bridging method. We remove linear phase ramps from both datasets.

633  
634 The Islands host seven active volcanoes characterized by large summit calderas with several km  
635 radii and by distinguished nonlinear deformation behavior. The surface coverage ranges from  
636 bare lava flows to dense vegetation. We discuss observations of Sierra Negra, Cerro Azul,  
637 Alcedo, Wolf and Fernandina volcanoes. Sierra Negra erupted on 26 June 2018, Wolf volcano in  
638 May 2015 and Fernandina volcano in September 2017 and June 2018.

639  
640 Products of the routine workflow include the mean LOS velocity (Fig. 6) and the displacement  
641 time-series (Fig. 7, shown for Fernandina island only). The center of Sierra Negra caldera  
642 uplifted at a mean rate of 60 cm/yr (Fig. 6) but the uplift rate varied with time (Fig. 7). The  
643 deformation at Cerro Azul volcano was caused by a sill intrusion in March 2017 (Bagnardi and  
644 Hooper, 2018).

645

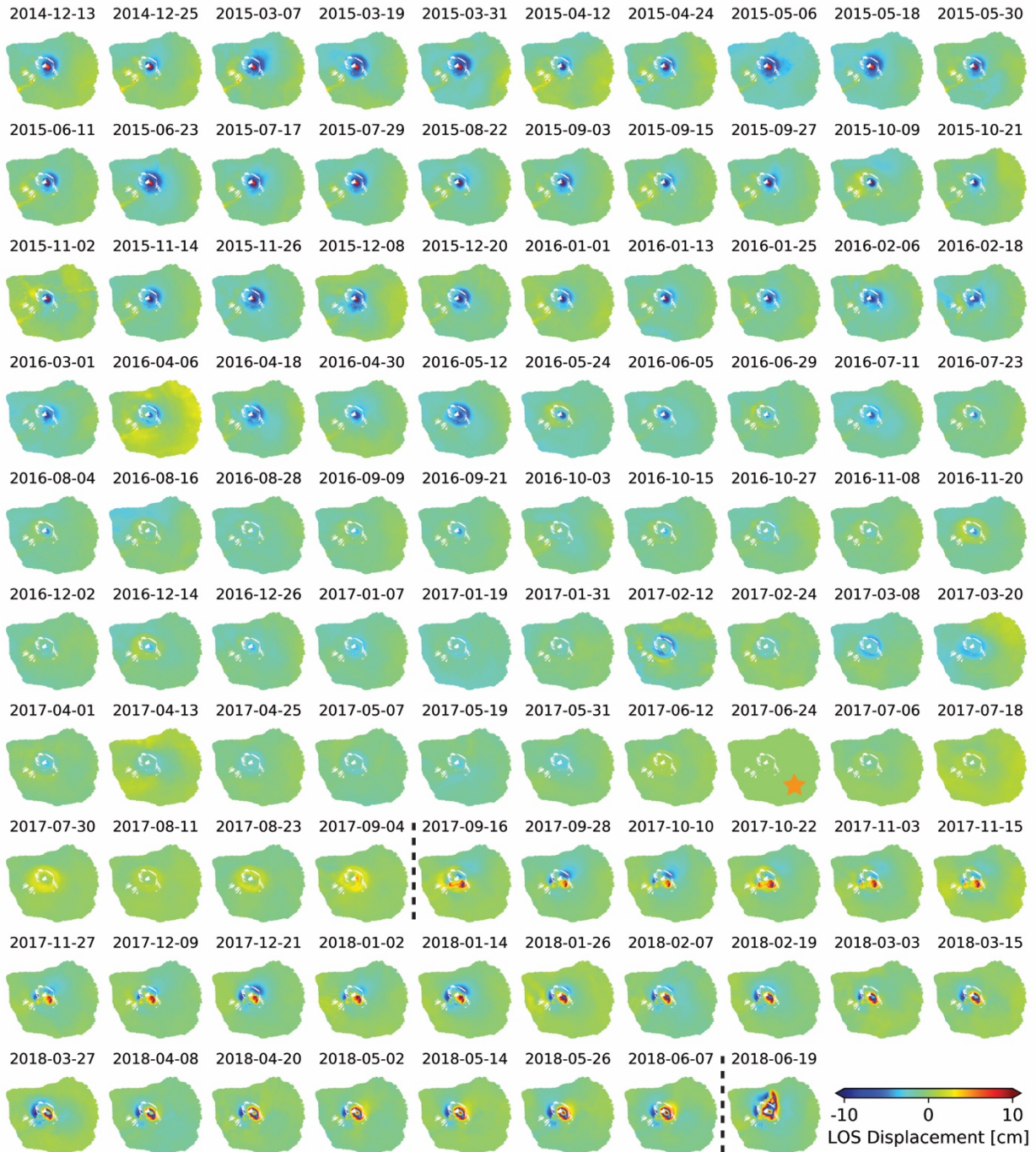


646

647 **Figure 6.** Mean LOS velocity at Isabela, Fernandina, and Santiago (main image), the  
 648 westernmost islands in the Galápagos archipelago (inset). The velocity is estimated from 98  
 649 Sentinel-1 descending track 128 SAR acquisitions from December 2014 to 19 June 2018 and  
 650 wrapped into  $[-3, 7)$  cm/yr for display so that one color-cycle represents 10 cm/yr displacement  
 651 velocity. Black square represents the reference point. Black triangle indicates the location of the  
 652 pixel covered by the lava flow of the 2015 Wolf eruption used in Fig. 15b and c. Dark blue in  
 653 Santiago island indicates biased velocity estimation caused by remaining unwrapping errors.  
 654 The southeast part of the caldera of Volcán Alcedo has been subsiding at a rate of  $-3.1$  cm/yr.  
 655 The center of Fernandina caldera uplifted by 14 cm before the September 2017 eruption,  
 656 subsided during the eruption and uplifted by 35 cm until the June 2018 eruption (Fig. 7).

657





658

659 **Figure 7.** Displacement time-series on Fernandina volcano with Sentinel-1 data. Dashed lines:

660 eruption events on September 2017 and June 2018. Orange star: automatically selected

661 reference date. The reference point is on Isabela island (black square in Fig. 6). Data are

662 wrapped into  $[-10, 10)$  cm for display.

## 663 5.1 Comparison with GPS

664 To validate the InSAR measurements we use the continuous GPS measurements at stations in the  
665 Sierra Negra caldera (circles in Fig. 8a; Blewitt et al., 2018). All three GPS components in east,  
666 north and vertical directions are used to project displacements into InSAR LOS direction. Both  
667 InSAR and GPS time-series are referenced to station GV01 in space and a common reference  
668 date in time. The InSAR data for each GPS point is obtained by linear interpolation (InSAR pixel  
669 size is  $64 \times 70 \text{ m}^2$ ). The InSAR and GPS total displacements for the period of interest (Fig. 8a)  
670 and the displacement time-series (Fig. 8b) agree very well, except for GV10 discussed below. To  
671 quantify the agreement, we assume the GPS time-series as truth and compute the coefficient of  
672 determination  $R^2$  between InSAR time-series and GPS time-series and the RMSE given as:

673

$$674 \quad RMSE_{InSAR} = \sqrt{\frac{\sum_{i=1}^{N_{comm}} (d_{InSAR}^i - d_{GPS}^i)^2}{(N_{comm} - 1)}} \quad (15)$$

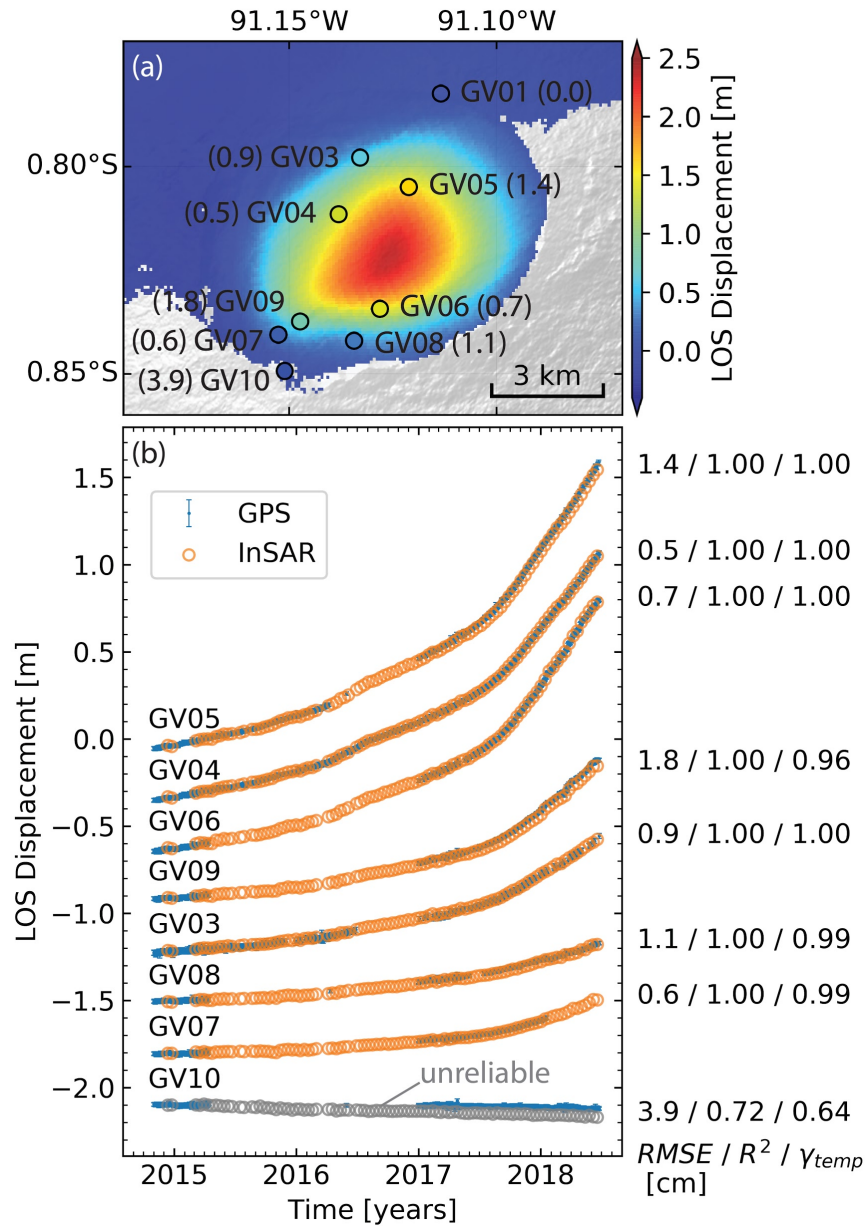
675

676 where  $d_{InSAR}^i = \phi_{dis}^i \cdot \frac{\lambda}{-4\pi}$  and  $d_{GPS}^i$  are the InSAR and GPS time-series in LOS direction,  
677 respectively, at the  $i_{th}$  common date.  $N_{comm}$  is the total number of common dates.

678

679 The temporal coherence at the GPS stations varies from 0.96 to 1.0 (Fig. 8b) indicating reliable  
680 InSAR measurements at these locations (except GV10). The  $R^2$  at the GPS stations are 1.0 and  
681 the RMSE varies from 0.5 to 1.8 cm (Fig. 8b), confirming the good agreement of the two  
682 measurements. The exception is station GV10 ( $R^2$  of 0.72 and RMSE of 3.9 cm), which is  
683 eliminated during posterior quality assessment due to low temporal coherence of 0.64 (below the  
684 threshold of 0.7). This station is located in a more densely vegetated area outside the caldera on

685 the rim where decorrelation due to vegetation affects the interferometric coherence (see supp.  
 686 Fig. S6).  
 687



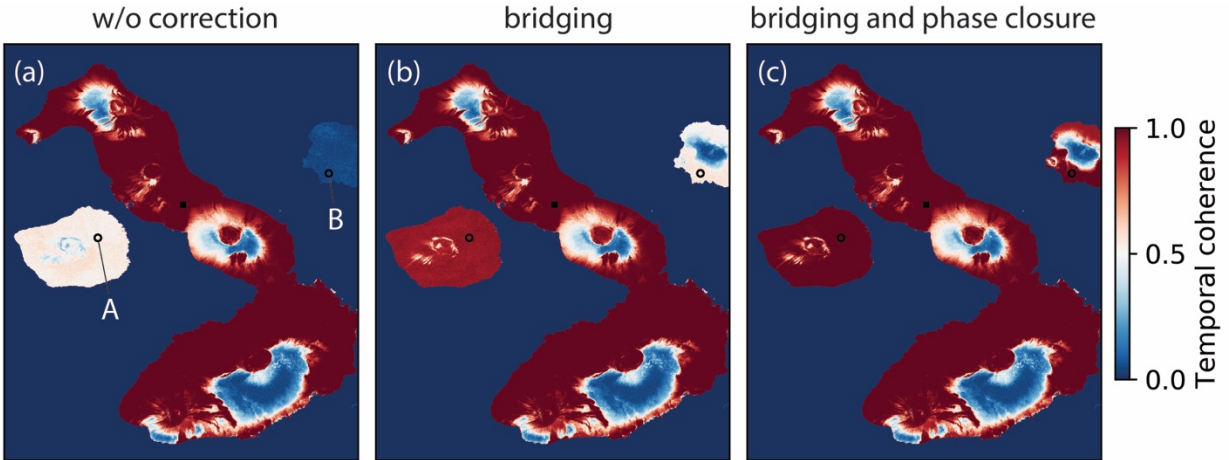
688  
 689 **Figure 8.** Comparing InSAR with GPS. (a) Total displacements in LOS direction for Sierra  
 690 Negra caldera from InSAR and GPS during 13 December 2014 - 19 June 2018. Circles: GPS  
 691 stations colored by displacement. Positive displacements indicate motion towards the satellite.

692 *(b) Displacement time-series from InSAR and GPS relative to GV01 (shifted for display). Blue*  
693 *GPS error bars: three sigma uncertainties (in LOS direction propagated from the uncertainties*  
694 *in east, north and up direction). 12 April 2015 is selected as the common reference because this*  
695 *SAR acquisition is characterized by small residual phase RMS. Gray circles: unreliable InSAR*  
696 *time-series with temporal coherence less than 0.7 (masked out by default).*

## 697 **5.2 Assessment of unwrapping error correction**

698 The islands of Fernandina and Santiago exhibit unwrapping errors relative to Isabela island due  
699 to the water separation. The unwrapping errors are represented by the low temporal coherence of  
700 about 0.49 and 0.07 for Fernandina and Santiago with Sentinel-1 dataset, respectively (pixel A  
701 and B in Fig. 9a). Since there is no indication of localized submarine deformation between  
702 Isabela and Fernandina or between Isabela and Santiago during the time period of Sentinel-1  
703 dataset, we believe the phase differences among the three islands fulfill the bridging assumption  
704 (less than  $\pi$  rad in magnitude). Thus, we applied the bridging method followed by the phase  
705 closure method to correct the potential unwrapping errors in the interferogram stack (Fig. 9). The  
706 bridging method leads to increased temporal coherence of 0.96 and 0.55 at these two points,  
707 respectively (Fig. 9b). The phase closure method leads to further increased temporal coherence  
708 of 1.00 and 1.00, respectively (Fig. 9c).

709  
710 We note that for Santiago, however, the phase closure method did not fully correct the large  
711 amount of unwrapping errors, resulting in a biased average velocity of -0.5 cm/yr (Fig. 6). This is  
712 due to the assumption of sparse unwrapping errors in the phase closure method with  $L^1$ -norm  
713 regularized least squares optimization. Conversely temporal coherence after the phase closure  
714 correction can be partly biased.



715

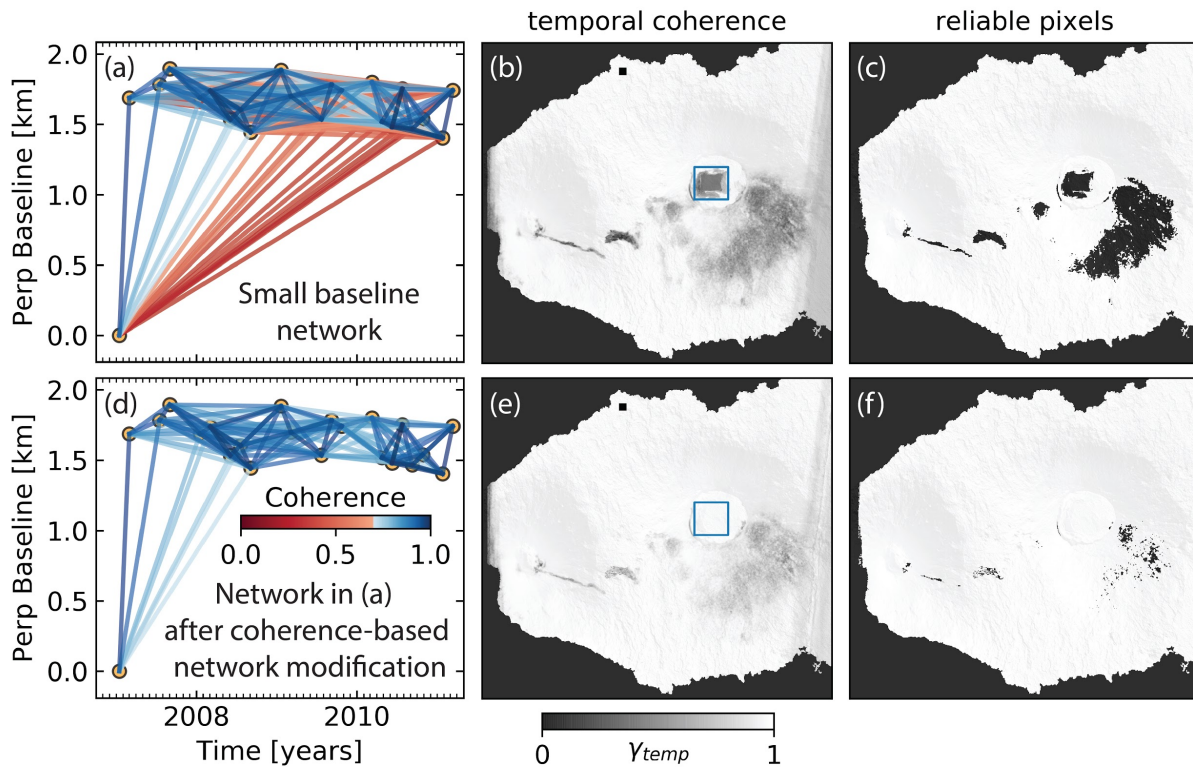
716 **Figure 9.** *Assessment of unwrapping error correction. Temporal coherence of the Sentinel-1*  
 717 *dataset from the network inversion of the interferogram stack (a) before the unwrapping error*  
 718 *correction, (b) after the unwrapping error correction with bridging and (c) with bridging and*  
 719 *phase closure. Black squares indicate the reference point.*

720 **5.3 Assessment of network inversion**

721 **5.3.1 Temporal coherence**

722 The quality of the network inversion can be evaluated posteriorly using the temporal coherence.  
 723 In Fig. 10, we compare for the ALOS-1 dataset the temporal coherence obtained by inverting a  
 724 network of small baseline interferograms using uniform weighting (classic SBAS; Fig. 10a-c)  
 725 with that obtained by inverting a network obtained by coherence-based network modification (an  
 726 option of the routine workflow) using inverse-variance weighting (Fig. 10d-f). The first approach  
 727 assumes an oversimplified linear relationship between the spatial coherence of each  
 728 interferogram and its spatial and temporal baseline (Hooper et al., 2007; Zebker and Villasenor,  
 729 1992); while the second approach uses the observed spatial coherence on the manually specified  
 730 area of interest (blue rectangle in Fig. 10b and d). This approach more reliably identifies the  
 731 coherent interferograms, especially when the simple decorrelation model does not apply, e.g.

732 vegetated areas, long temporal baseline interferograms on Sierra Negra caldera with low  
 733 coherence due to high deformation phase gradient (Baran et al., 2005). The improvement in  
 734 temporal coherence using the second approach leads to additional reliable pixels (Fig. 10c and f).



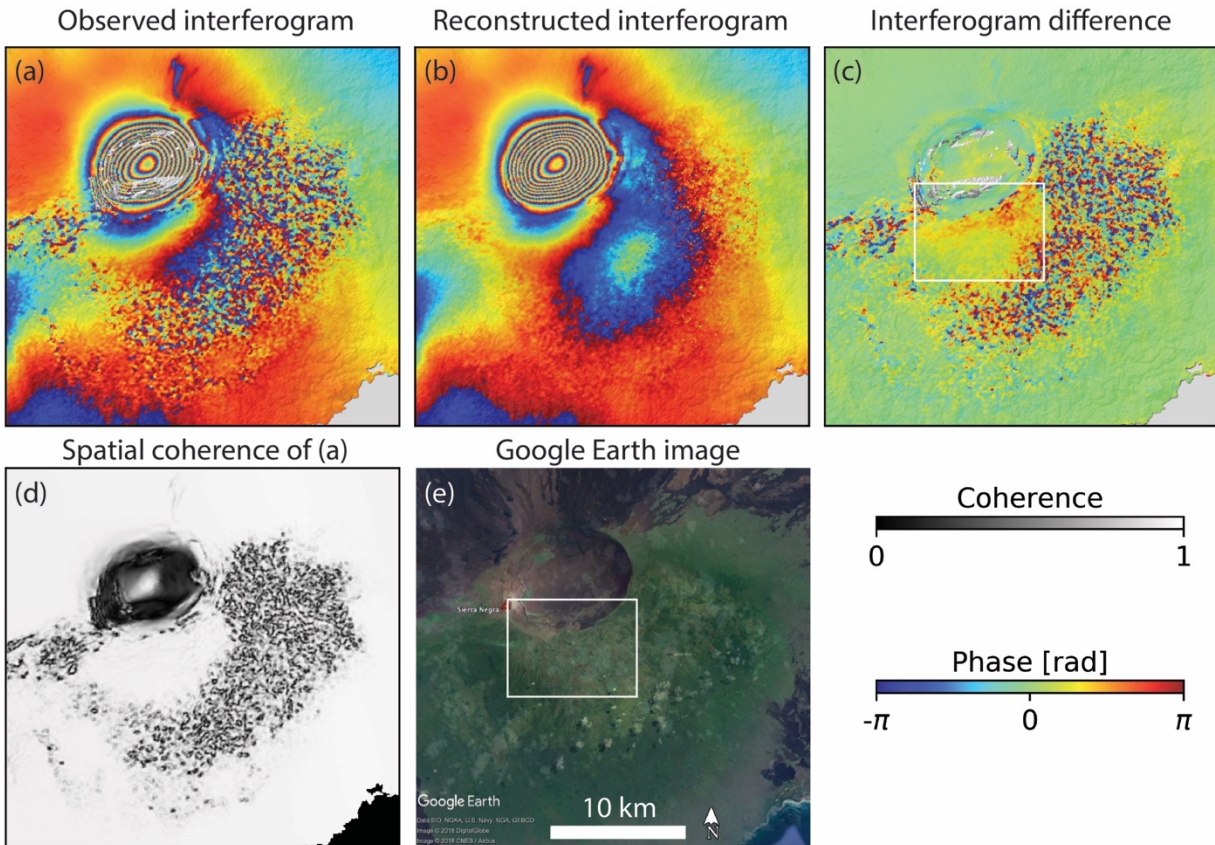
735  
 736 **Figure 10.** Impact of network modification on temporal coherence for ALOS-1 dataset. (a)  
 737 Network configuration, (b) temporal coherence and (c) reliable pixels with temporal  
 738 coherence > 0.7 from inversion of small baseline network with uniform weighting. (d-e): same as  
 739 (a-c) but from inversion of a network obtained by coherence-based network modification with  
 740 inverse-variance weighting. Lines in (a) and (d) represent interferograms colored by the average  
 741 spatial coherence within the Sierra Negra caldera (blue rectangle in (b, d)). Black squares in (b,  
 742 e) indicate the reference point.

### 743 **5.3.2 Inverted raw phase**

744 The temporal filtering performed by the inversion of a redundant network of interferograms is  
745 illustrated by comparing an observed interferogram with the interferogram reconstructed from  
746 the inverted raw phase time-series (referred to by some authors as linked phase). Fig. 11 shows  
747 an ALOS-1 interferogram with 3.5 years temporal baseline. The observed and the reconstructed  
748 interferograms (Fig. 11a and b) are very similar except south and east of the caldera, where the  
749 observed interferogram is incoherent but not the reconstructed interferogram as shown by the  
750 high-frequency noise in the interferogram difference (Fig. 11c). This area is forested and  
751 characterized by a low spatial coherence (Fig. 11d and e). This example, although with extreme  
752 temporal baselines, demonstrates how the network inversion filters out the temporal  
753 decorrelation noise (Ansari, 2017; Guarnieri and Tebaldini, 2008; Pepe et al., 2015;).

754

755 There is a difference in the north of the decorrelating area (yellow colors marked by white  
756 rectangle in Fig. 11c). These areas are lightly vegetated (Fig. 11e), the discrepancy in phase is  
757 likely caused by the soil or tree moisture considering its sensitivity to L-band SAR data (De Zan  
758 and Gamba, 2018) and land cover (Fig. 11e).



759

760 **Figure 11.** Spatial inspection of the inverted raw phase. (a) Observed interferometric phase and  
 761 (b) reconstructed phase from the inverted raw phase time-series; (c) difference between (a) and  
 762 (b); (d) observed spatial coherence; (e) optical image from Google Earth. The ALOS-1  
 763 interferogram has temporal baseline of 3.5 years (2 Mar 2007 - 10 Sep 2010) and perpendicular  
 764 baseline of 219 m. In (a) part of the caldera is masked out during phase unwrapping because of  
 765 low coherence. White rectangles in (c and e): areas likely affected by soil or tree moisture. The  
 766 phase is wrapped into  $[-\pi, \pi)$  for display.

#### 767 5.4 Noisy SAR acquisitions

768 Noisy acquisitions with severe atmospheric delays or decorrelation noise could potentially bias  
 769 the estimation of topographic residuals, the average velocity or coefficients of any temporal

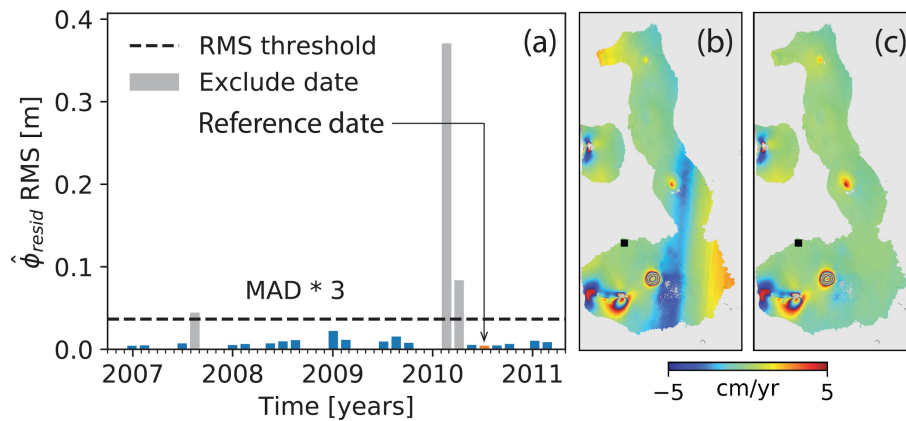


770 deformation model. In the routine workflow, they are automatically identified and excluded in  
 771 the estimations.

772

773 Fig. 12 shows the impact of noisy acquisitions on the average velocity estimation for the L-band  
 774 ALOS-1 dataset. Several acquisitions are severely contaminated by ionospheric streaks and  
 775 identified by high residual phase RMS value (gray bars in Fig. 12a). Comparing the estimated  
 776 average velocities from displacement time-series with noisy acquisitions (Fig. 12b) and without  
 777 noisy acquisitions (Fig. 12c) reveals that excluding the noisy acquisitions significantly reduces  
 778 the estimation bias. The residual phase time-series  $\hat{\phi}_{resid}$  estimated from equation (13) is shown  
 779 in supp. Fig. S7.

780



781

782 **Figure 12.** Impact of noisy acquisitions on velocity estimation. (a) RMS of the residual phase  
 783 estimates  $\hat{\phi}_{resid}$  for each acquisition in the ALOS-1 dataset calculated using equation (14).  
 784 Dashed line: threshold (three times MAD of the RMS time-series by default). Gray bars: noisy  
 785 acquisitions with RMS larger than the threshold. (b and c): estimated average LOS velocities  
 786 from displacement time-series with and without noisy acquisitions, respectively. Velocities are  
 787 wrapped into  $[-5, 5)$  cm/yr for display.

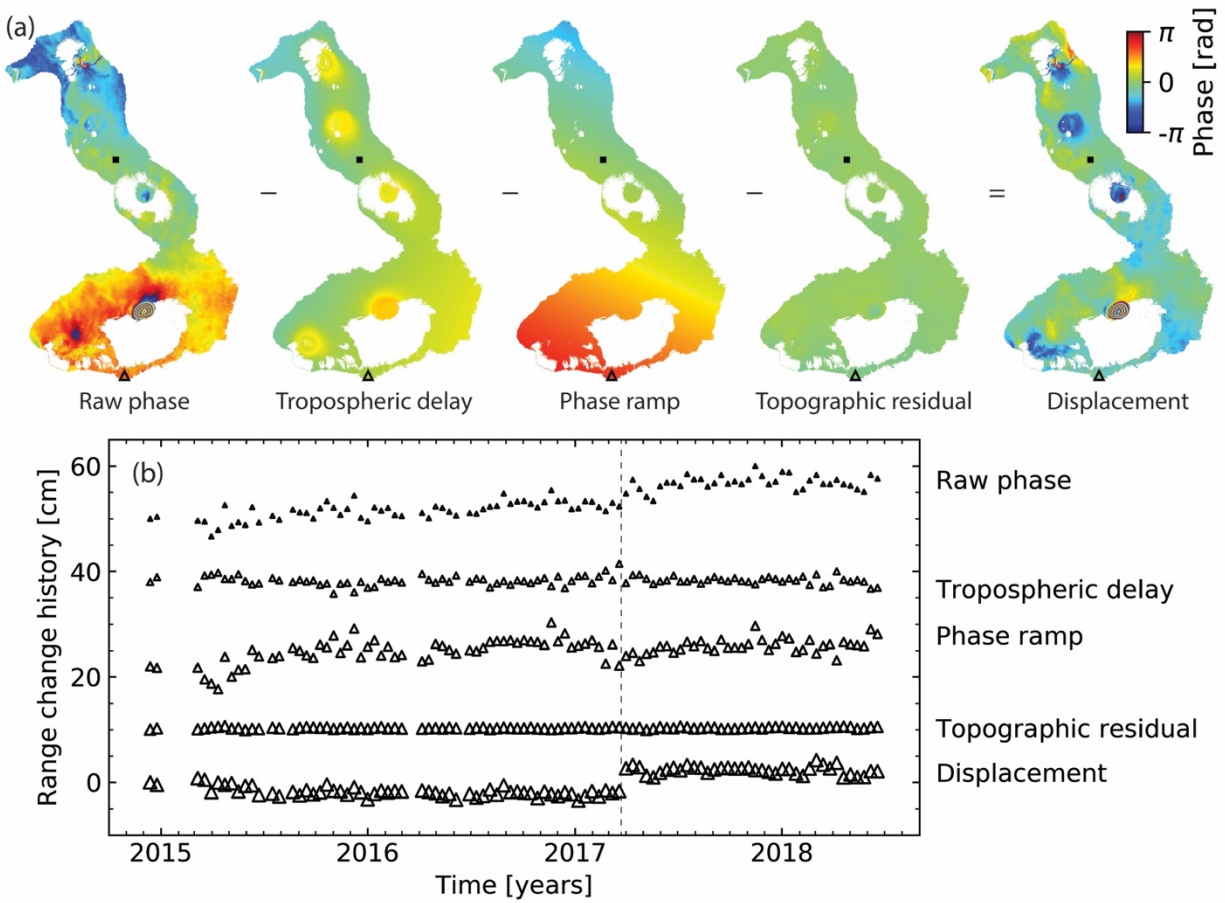
## 788 6. Discussion

### 789 6.1 Phase corrections in the time-series domain

790 In the presented approach the phase corrections are applied in the time-series domain in contrast  
791 to other approaches where they are applied in the interferogram domain (Agram et al., 2013;  
792 Berardino et al., 2002). Both types of approaches give identical results, but the time-series  
793 domain approach has two advantages: first, it is computationally more efficient because it uses  
794  $N-1$  unwrapped phases, in contrast to the much larger number of interferograms for the  
795 interferogram domain approach (up to  $N \times (N - 1)/2$  for all possible interferograms); second,  
796 the impact of the corrections is readily evaluated in both the spatial and temporal domains.

797

798 Fig. 13 upper panel (a) shows how the displacement at one acquisition is obtained by subtracting  
799 the estimations of the tropospheric delay, of the phase ramp and of the topographic residual from  
800 the raw phase. The time-series for a pixel along the southern coast of Isabela demonstrates the  
801 power of the corrections (Fig. 13b). The area experienced a sill intrusion in March 2017 (dashed  
802 line in Fig. 13b; Bagnardi and Hooper, 2018). The permanent ground displacement of 5 cm in  
803 LOS direction is difficult to discern in the raw phase time series but becomes visible after  
804 applying the three corrections. Note that this pixel is far away from the intrusion in the first stage  
805 and only affected by the intrusion in the second stage, thus showing only one jump in the  
806 displacement time-series. For Sentinel-1 the topographic residuals are small (less than 4 cm in  
807 this dataset) due to the small orbital tube but this is different for other sensors (Fattahi and  
808 Amelung, 2013).



809

810 **Figure 13.** Illustration of phase corrections in the time-series domain: (a) at one acquisition (12  
 811 May 2016; the reference date is 27 September 2015); (b) at one pixel (southern flank of Cerro  
 812 Azul, marked as a triangle in the upper panel;  $[W91.1917^\circ, S1.0352^\circ]$ ). Displacements are  
 813 obtained by subtracting the estimated tropospheric delay, phase ramp and topographic residual  
 814 from the raw phase (equation (4)). Black square in (a) indicates the reference point. Data are  
 815 wrapped into  $[-\pi, \pi)$  for display. All range change histories in (b) start at zero but are shifted  
 816 for display. The permanent displacement due to a sill intrusion in March 2017 (marked as  
 817 dashed line) is visible after phase corrections.

## 818 **6.2 Order of phase corrections**

819 In our proposed workflow the tropospheric delay correction using external independent GAMs  
820 should be applied first. The order of the other phase corrections is interchangeable because they  
821 exploit different aspects of the InSAR data. Empirical tropospheric delay correction based on  
822 delay-elevation ratio removes signals correlating with the topography. Phase deramping removes  
823 signals correlating with the spatial coordinates (linearly or quadratically). Topographic residual  
824 correction removes signals correlating in time with the perpendicular baseline. We recommend  
825 applying phase deramping before topographic residual correction so that the estimated step  
826 functions do not have to be deramped again.

## 827 **6.3 Interferogram network redundancy**

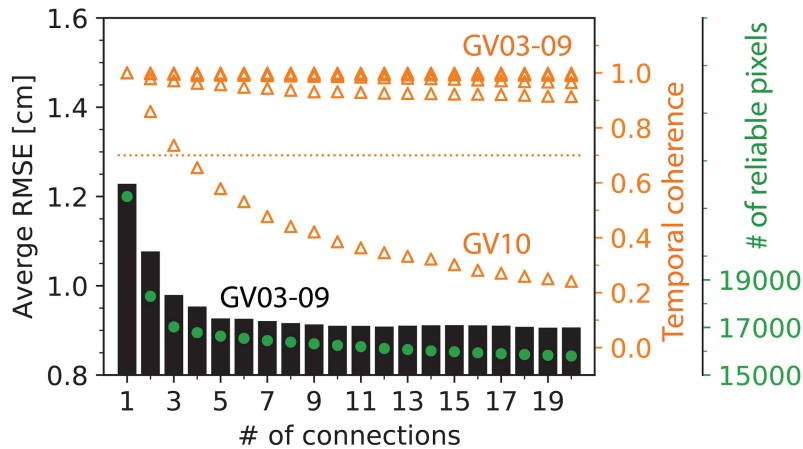
828 We consider stacks of Sentinel-1 interferograms from section 5 with different numbers of  
829 sequential connections for each acquisition to assess the impact of network redundancy on the  
830 estimation of (i) the displacement time-series and (ii) the temporal coherence (the reliability  
831 measure). We compute the RMSE of the InSAR time-series at the GPS stations within Sierra  
832 Negra caldera, assuming that the GPS measurements are the truth (see section 5.1; Fig. 14) and  
833 examine the temporal coherence for these pixels. We also count the number of reliable pixels  
834 (spatial coverage; temporal coherence above 0.7).

835  
836 The average RMSE (bars in Fig. 14; GV10 excluded) decreases (improves) with the increasing  
837 number of sequential connections rapidly until 5 connections then slowly until the reduction  
838 become negligible. The temporal coherence (orange triangles in Fig. 14) stays at high values  
839 (above 0.9) for all stations, except for GV10, for which it decreases to 0.65 at 4 connections and  
840 to 0.24 at 20 connections. The low temporal coherence indicates that this is not a reliable pixel. It  
841 also has a relatively large RMSE (Fig. 8b in section 5.1). This example shows that increasing

842 network redundancy leads to improved identification of reliable pixels. For this specific dataset,  
 843 a network of interferograms with 5 connections give a good balance among precision, reliability  
 844 and spatial coverage (green dots in Fig. 14).

845  
 846 We note that in this case decorrelation noise is the dominant error source. Unwrapping errors  
 847 remaining after unwrapping error correction were excluded by removal of affected  
 848 interferograms using coherence-based network modification (see supp. Fig. S8). Still remaining  
 849 unwrap errors were suppressed by the weighting. Thus, more observations always help to reduce  
 850 the stochastic decorrelation noise, resulting in a more accurate estimation of the displacement  
 851 measurement (lower RMSE) and of the reliability measure (temporal coherence).

852



853  
 854 **Figure 14.** Average RMSE of InSAR time-series (black bars), temporal coherence (orange  
 855 triangles) at GPS stations and number of reliable pixels (green dots) as functions of the number  
 856 of sequential connections. Dotted orange line: temporal coherent threshold of 0.7.

857  
 858 As a practical implication, more interferograms are always preferred if the computing capacity  
 859 allows (Ansari et al., 2017). Since we cannot get the estimated spatial coherence before the

860 interferogram generation (due to the imperfect coherence model), generating a more redundant  
861 network provides room to exclude low coherent interferograms especially those containing  
862 reliable regions with unwrapping errors and still keep the network redundancy (temporal  
863 coherence would always be one and meaningless if the system of network inversion is not  
864 overdetermined, shown as orange triangles in Fig. 14 at 1 connection). In addition, a more  
865 redundant network could potentially lead to a better unwrapping error correction based on phase  
866 closure. Thus, we recommend using relatively relaxed interferogram selection thresholds (more  
867 connections in sequential networks, larger temporal and perpendicular baselines in small baseline  
868 networks) to generate more potentially coherent interferograms.

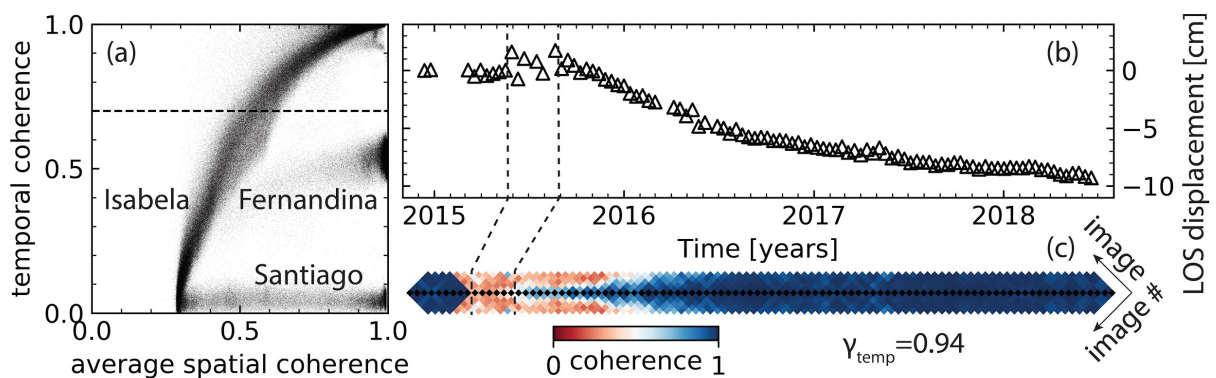
#### 869 **6.4 Temporal coherence as the reliability measure**

870 We discuss the advantages and limitations of using the temporal coherence as the reliability  
871 measure (Fig. 15). An advantage is that the temporal coherence accounts for phase-unwrapping  
872 errors and is therefore a more robust reliability measure for the estimated raw phase time-series  
873 than average spatial coherence. Fig. 15a shows how the temporal coherence is affected by  
874 unwrapping errors. In the absence of unwrapping errors (pixels on Isabela island) the temporal  
875 and average spatial coherence are correlated but not when unwrapping errors are present (pixels  
876 on Fernandina and Santiago islands). The improvements in temporal coherence by phase-  
877 unwrapping error correction is illustrated in Fig. 9.

878

879 However, a limitation is that the temporal coherence cannot capture temporal variations of the  
880 reliability of the phase time-series. Fig. 15b and c show the displacement time-series and  
881 coherence matrix of a pixel that was covered by a lava flow during the 2015 Wolf eruption  
882 (marked as a black triangle in Fig. 6). The surface change brings down the spatial coherence to  
883 0.3 during May-July 2015 (red grids in Fig. 15c), resulting in coherent, connected interferogram

884 networks only before and after the lava flow emplacement. This, however, has negligible impact  
 885 on the temporal coherence. With a temporal coherence of 0.94 the pixel is considered reliable  
 886 although valid displacement measurements were possible only before and after the flow  
 887 emplacement (after flow emplacement the pixel shows surface subsidence due to lava cooling).  
 888 A three-dimensional reliability measure such as the covariance matrix of decorrelation noise  
 889 (Agram and Simons, 2015) is more meaningful in this case of partially coherent scatterers, but  
 890 this is beyond the scope of this manuscript.



891  
 892 **Figure 15.** Advantage and limitation of temporal coherence as reliability measure. (a) Temporal  
 893 coherence versus average spatial coherence for land pixels of the Sentinel-1 dataset without  
 894 unwrapping error correction. Dashed line: default temporal coherence threshold of 0.7. Three  
 895 point clouds represent pixels on Isabela, Fernandina and Santiago islands. (b and c)  
 896 Displacement time-series and the diagonal section of coherence matrix of a pixel on the lava  
 897 flow of the 2015 Wolf eruption located at  $[W91.2838^\circ, N0.0232^\circ]$  (black triangle in Fig. 6).  
 898 Reference pixel is located  $\sim 600$  m to the west  $[W91.2891^\circ, N0.0243^\circ]$ . The coherence matrix is  
 899 rotated  $45^\circ$  anticlockwise and shows the five diagonals below and above the main diagonal.  
 900 Dashed lines: period of lava flow emplacement.

## 901 **6.5 Comparing MintPy with GIANt**

902 We compare the performance of the MintPy routine workflow with the classic SBAS approach  
903 (Berardino et al, 2002), the New Small Baseline Subset (NSBAS) approach (Doin et al., 2011;  
904 López-Quiroz et al., 2009) and the Multiscale InSAR Time-Series approach (Hetland et al.,  
905 2012), as implemented in the Generic InSAR Analysis Toolbox (GIANt) (Agram et al., 2013)  
906 and referred to as G-SBAS, G-NSBAS, and G-TimeFun, respectively. We use the Galápagos  
907 Sentinel-1 dataset and a spatial coherence threshold of 0.25 (as commonly done with GIANt,  
908 Agram and Simons, 2015) for all approaches including MintPy. Tropospheric delays are  
909 corrected from the ERA-Interim model using the PyAPS software (Jolivet et al., 2011).

910

911 In the following we discuss the differences between the four approaches (summarized in table 1).  
912 We demonstrate the impact on the displacement time-series using three pixels (Fig. 16i): a high  
913 coherent pixel (pixel A), a low coherent pixel (pixel B) and a high coherent pixel with  
914 unwrapping errors and complex displacement (pixel C). The coherence matrices of the three  
915 pixels are shown in Fig. 16j. For the high coherent pixel A, all approaches give nearly identical  
916 results.

### 917 **6.5.1 Initial pixel selection**

918 MintPy selects pixels which have for every SAR acquisition a minimum number of coherent  
919 interferograms (1 by default); G-SBAS and G-TimeFun select pixels that are coherent in all  
920 interferograms; while G-NSBAS selects pixels with a predefined total minimum number of  
921 coherent interferograms (we use a minimum of 300 out of 475). This leads to differences in the  
922 spatial measurement coverage between the four approaches (Fig. 16e-h). Compared with G-  
923 SBAS and G-TimeFun, MintPy has better coverage within the calderas of Alcedo and  
924 Fernandina and along Alcedo's flank. G-NSBAS has the best spatial coverage among all



925 approaches. The spatial coverages are shown by the distribution of the number of interferograms  
926 for pixels selected by the four approaches (Fig. 16a-d).

### 927 **6.5.2 Weighted network inversion**

928 MintPy uses weighting (the inverse-variance by default) during the network inversion while the  
929 other three approaches in GIANt do not. The impact on the estimated displacement time-series is  
930 not negligible when there is significant quality variation among the observations. One example is  
931 the displacement time-series of the low coherent pixel B in Fig. 16i. This is confirmed by the  
932 nearly identical result between G-NSBAS and MintPy without weighting (see supp. Fig. S9a).  
933 Note that the asymmetric red grids along the horizontal black grids in Fig. 16j indicate the  
934 masked out interferogram due to spatial coherence thresholding, thus, only MintPy and G-  
935 NSBAS give estimation results.

### 936 **6.5.3 Unwrapping error correction**

937 MintPy supports bridging and phase closure methods to correct unwrapping errors in the  
938 interferograms, which GIANt does not. Unwrap errors introduce bias in the estimated phase  
939 ramps and displacement time-series. One example is the difference of the displacement time-  
940 series on pixel C in Fig. 16i between MintPy and G-(N)SBAS. This is confirmed by the nearly  
941 identical result between G-(N)SBAS and MintPy without unwrapping error correction (see supp.  
942 Fig. S9b). The bias introduced by unwrapping errors is also evident in the velocity field at the  
943 west side of Fernandina volcano (Fig. 16e-h).

### 944 **6.5.4 No deformation model**

945 MintPy and G-SBAS do not assume temporal deformation model in network inversion. G-  
946 NSBAS and G-TimeFun require temporal deformation models: G-NSBAS uses the model only  
947 when the network is not fully connected in order to link multiple subsets of interferograms; while

948 G-TimeFun requires over-complete, potentially redundant models, which can be added manually  
 949 by user (Agram et al., 2013; Hetland et al., 2012). Thus, with the default configuration in this  
 950 case, G-TimeFun did not resolve the displacement jump due to the September 2017 Fernandina  
 951 eruption (pixel C in Fig. 16i).

### 952 **6.5.5 Reliable pixel selection**

953 In contrast to approaches in GIANt, MintPy assesses the quality of the inverted phase time-series  
 954 using temporal coherence and masks out unreliable pixels (gray area in Fig. 16a). We note that a  
 955 higher temporal coherence threshold (0.8 instead of the default 0.7) is used because the spatial  
 956 coherence thresholding reduces the number of interferograms for unreliable pixels, bringing up  
 957 the temporal coherence value.

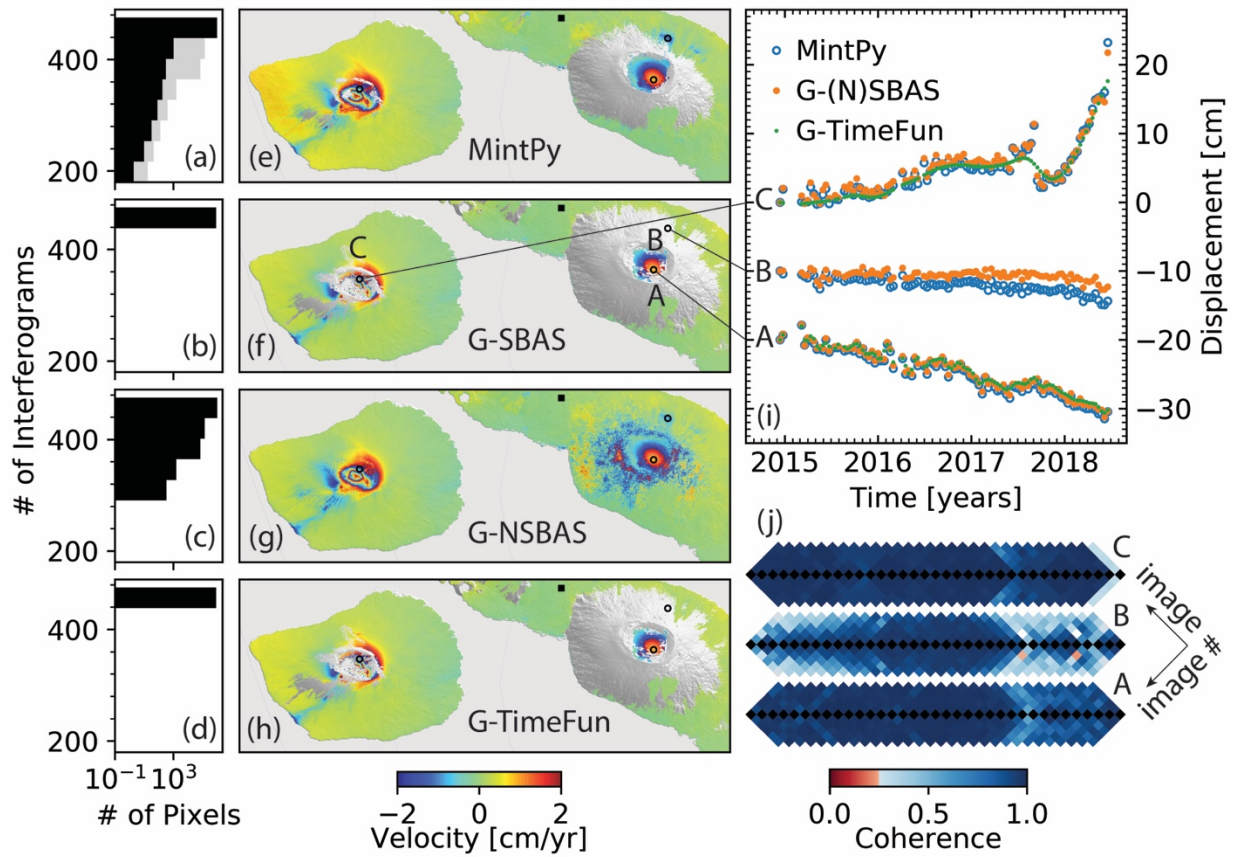
958

959 **Table 1.** Summary of the differences of time-series analysis approaches in MintPy and GIANt.  
 960 All approaches use small baseline network of unwrapped interferograms and linear optimization  
 961 time-series estimator.

Aspect	MintPy	G-SBAS	G-NSBAS	G-TimeFun
initial pixel selection	a minimum number of coherent interferograms for every acquisition	coherent in all interferograms	a total minimum number of coherent interferograms	coherent in all interferograms
weighted inversion	yes	no	no	no

unwrapping error correction	bridging / phase closure	no	no	no
posterior quality assessment	yes	no	no	no
prior deformation model	no	no	yes	yes
phase correction operation	time-series domain	interferogram domain	interferogram domain	interferogram domain

962



963  
964

**Figure 16.** Comparison of MintPy with GIANT approaches for the Sentinel-1 dataset for the

965 Galápagos. (a-d): Distribution of the number of interferograms for pixels used (number of pixels

966 *for each interferogram bin) by the four time-series approaches on the entire Isabela and*  
967 *Fernandina islands in log scale. Gray area in (a): unreliable pixels (pixels processed but*  
968 *discarded because of low temporal coherence). (e-h): LOS velocity estimated from the*  
969 *displacement time-series produced by the four time-series approaches on Fernandina and*  
970 *Alcedo volcano. Velocities are wrapped into  $[-2, 2)$  cm/yr for display. Black squares: reference*  
971 *point. (i): Displacement time-series for pixels marked in (e-h). (j): Coherence matrix for pixels in*  
972 *(i) (rotated to make the matrix diagonal line horizontal; only showed the main diagonal and the*  
973 *five diagonals below and above; only showed the data from 7 May 2017 - 19 June 2018). The*  
974 *lower and upper half: interferograms before and after phase masking, respectively. The*  
975 *asymmetric red grids between the upper and lower half for pixel B indicate masked out*  
976 *interferograms with spatial coherence  $< 0.25$ .*

## 977 **7. Summary and conclusions**

978 We have reviewed the mathematical formulation for the weighted network inversion and for the  
979 post-inversion phase corrections for time series analysis of small baseline InSAR stacks. In  
980 contrast to some persistent scatterer methods, the presented approach does not require prior  
981 deformation models or temporal filtering and is therefore well suited to extract nonlinear  
982 displacements. Reliable pixels are identified using the temporal coherence. Noisy acquisitions  
983 with severe atmospheric turbulence are identified using an outlier detection method based on the  
984 median absolute deviation of the residual phase RMS and are excluded during the estimations of  
985 topographic residual and average velocity.

986

987 Our workflow includes two methods to correct for, and one method to exclude remaining phase-  
988 unwrapping errors. The first unwrapping error correction method is bridging. This method uses

989 MST bridges to connect the reliable regions of each interferogram, assuming that the phase  
990 differences between neighboring regions are less than  $\pi$  rad in magnitude. This method is  
991 particularly well-suited for islands and/or areas with steep topography. The second method is the  
992 phase closure method. This method exploits the conservativeness of the integer ambiguities of  
993 interferograms triplets. A sparse solution for the phase-unwrapping integer ambiguity is obtained  
994 using the  $L^1$ -norm regularized least squares approximation. Coherent phase-unwrapping errors  
995 can be identified using the distribution of the number of triplets with non-zero integer ambiguity  
996 of the closure phase. Best results are obtained by combining these two methods.

997

998 The method to exclude remaining coherent phase-unwrapping errors is coherence-based network  
999 modification. In this approach affected interferograms are identified and excluded using a  
1000 threshold of spatial coherence calculated over a customized area of interest that includes the low  
1001 coherent areas surrounding the areas with coherent phase-unwrapping error.

1002

1003 We have applied the routine workflow to ALOS-1 and Sentinel-1 data acquired over the  
1004 Galápagos volcanoes. The InSAR result shows very good agreement with independent GPS  
1005 measurements. A comparison with the algorithms implemented in the GIANt software shows  
1006 similar performance in the high coherent areas but superior performance in the low coherent  
1007 areas and the high coherent areas with phase-unwrapping errors or complex displacement  
1008 because of unwrapping error correction, weighted network inversion, initial and reliable pixel  
1009 selection using temporal coherence.

1010

1011 We investigated how some configurations of the routine workflow affect the precision and  
1012 accuracy of the InSAR measurement using real and/or simulated data. The conclusions are:

1013  
1014  
1015  
1016  
1017  
1018  
1019  
1020  
1021  
1022  
1023  
1024  
1025  
1026  
1027  
1028  
1029  
1030  
1031  
1032  
1033  
1034  
1035

1. Inverse-variance weighting gives the most robust and one of the best performances for network inversion among four different weighting functions: uniform, coherence, inverse-variance and Fisher information matrix.
2. For interferogram networks with 3, 5 and 10 sequential connections, the phase closure method fully corrects for phase-unwrapping errors if less than 5, 20 and 35% of the interferograms are affected by phase-unwrapping errors, respectively (with maximum errors of 2 cycles). This shows that the phase closure method performs better for more redundant networks.
3. Increasing the network redundancy improves the network inversion and the estimation of temporal coherence (as long as phase-unwrapping errors have been corrected or excluded), resulting in more accurate estimation of the displacement time-series and identification of reliable pixels. Thus, we recommend using more connections in sequential networks, and to use larger temporal and perpendicular baselines in small baseline networks.
4. The order of the InSAR-data-dependent phase corrections (the empirical tropospheric delay correction based on the delay-elevation ratio, topographic residual correction and phase deramping) is interchangeable and has negligible impact on the noise-reduced displacement time-series.
5. Temporal coherence is a more robust reliability measure than average spatial coherence because it accounts for phase-unwrapping errors. However, it does not capture temporal variations of the reliability of the phase time-series, limiting its usefulness for partially coherent scatterers.

## 1036 **Acknowledgments**

1037 The Sentinel-1 data were provided by ESA and made available by Alaska Satellite Facility  
1038 (ASF). The ALOS-1 data were provided by JAXA and made available by ASF via the Seamless  
1039 SAR Archive (SSARA), a service provided by the UNAVCO facility. GPS data was provided by  
1040 the Nevada Geodetic Laboratory (University of Nevada, Reno). We thank Yunmeng Cao from  
1041 the Central South University for the discussion on the decorrelation noise and the order of  
1042 various phase corrections, Sara Mirzaee from University of Miami (UM) for the discussion on  
1043 full network inversion techniques, Xiaohua Xu and David Sandwell from Scripps Institution of  
1044 Oceanography for the discussion on the sparse solution of the integer ambiguity of the closure  
1045 phase. We thank Scott Baker from UNAVCO, Joshua Zahner, David Grossman and Alfredo  
1046 Terrero from UM for code contributions. This work was supported by NASA Headquarters  
1047 under the Earth and Space Science Fellowship program (Grant No. NNX15AN13H), the NISAR  
1048 Science Team (Grant No. NNX16AK52G) and National Science Foundation's Geophysics  
1049 program (Grant No. EAR1345129). Part of the research was carried out at the Jet Propulsion  
1050 Laboratory, California Institute of Technology, under a contract with the National Aeronautics  
1051 and Space Administration.

## 1052 **Computer code availability**

1053 The presented workflow is implemented as the Miami INsar Time-series software in PYthon  
1054 (MintPy), with open-source code, wiki and tutorials in Jupyter Notebook freely available on  
1055 GitHub (<https://github.com/insarlab/MintPy>; ~22 M in size) under GNU Generic Public License  
1056 version 3. Figures in this manuscript are plotted using Jupyter Notebook ([link on GitHub](#)). Test  
1057 data from different InSAR processors are freely available on Zenodo ([link 1](#); [link 2](#); [link 3](#)).

1058 Time-series products from the routine workflow in this manuscript are available here:  
1059 <https://insarmaps.miami.edu>.

## 1060 **Appendix A: List of symbols and acronyms**

### 1061 **Table A1. List of acronyms**

1062	DS	Distributed scatterer.
1063	FIM	Fisher information matrix.
1064	GAM	Global atmospheric model.
1065	GIAnt	Generic InSAR Analysis Toolbox.
1066	G-SBAS	Small baseline subset in GIAnt.
1067	G-NSBAS	New small baseline subset in GIAnt.
1068	G-TimeFun	Multiscale InSAR Time-Series in GIAnt.
1069	LASSO	Least absolute shrinkage and selection operator
1070	LOS	Line of sight.
1071	MAD	Median absolute deviation.
1072	MST	Minimum spanning tree.
1073	PDF	Probability density function.
1074	PS	Persistent scatterer.
1075	RMS	Root mean square.
1076	RMSE	Root mean square error.
1077	SBAS	Small baseline subset.
1078	SLC	Single look complex.
1079	SNAPHU	Statistical-cost, Network-flow Algorithm for Phase Unwrapping.
1080	WLS	Weighted least squares.



1081

1082 **Table A2. List of symbols**

1083	Symbol	Parameter
1084	-----	
1085	$A$	Design matrix for network inversion in size of $M \times (N - 1)$ .
1086	$C$	Design matrix for the closure phase of interferogram triplets.
1087	$D$	Design matrix for the constraint of unwrapping error-free interferograms.
1088	$H$	All-one column matrix in size of $M \times 1$ .
1089	$L$	Number of looks in range and azimuth directions in total.
1090	$M$	Number of interferograms.
1091	$N$	Number of SAR acquisitions.
1092	$T$	Number of interferogram triplets.
1093	$U$	Matrix of the phase-unwrapping integer ambiguity in size of $M \times 1$ .
1094	$W$	Weight matrix for network inversion in size of $M \times M$ .
1095	$C^{ijk}$	Closure phase of the interferograms triplet formed from acquisitions at $t_i$ , $t_j$ , and $t_k$ .
1096	$C_{int}^{ijk}$	Integer ambiguity of $C^{ijk}$ .
1097	$T_{int}$	Number of triplets with non-zero $C_{int}^{ijk}$ among all triplets.
1098	$\Delta\phi^j$	Interferometric phase of the $j_{th}$ unwrapped interferogram.
1099	$\Delta\phi_\varepsilon^j$	Interferometric phase residual of the $j_{th}$ unwrapped interferogram.
1100	$\Delta\phi$	Vector of the interferometric phase of all interferograms.
1101	$\Delta\phi_\varepsilon$	Vector of the interferometric phase residual of all interferograms.
1102	$\phi^i$	Raw phase between the $i_{th}$ and the $I_{st}$ acquisition.
1103	$\phi$	Vector of raw phase of all acquisitions (raw phase time-series).

1104	$\hat{\phi}$	The estimated vector of raw phase time-series.
1105	$\phi_{dis}^i$	Phase due to the displacement between the $i_{th}$ and the $I_{st}$ acquisition.
1106	$\hat{\phi}_{tropo}^i$	Estimated tropospheric delay between the $i_{th}$ and the $I_{st}$ acquisition.
1107	$\hat{\phi}_{geom}^i$	Estimated geometrical range difference between the $i_{th}$ and the $I_{st}$ acquisition
1108		caused by the non-zero spatial baseline.
1109	$\phi_{resid}^i$	Residual phase remained between the $i_{th}$ and the $I_{st}$ acquisition.
1110	$\phi_{resid}$	Vector of the residual phase of all acquisitions (residual phase time-series)
1111	$\hat{\phi}_{resid}(p)$	Estimated vector of the residual phase time-series on pixel $p$ .
1112	$\delta L_p^i$	Integrated absolute single path tropospheric delay between the $i_{th}$ and the $I_{st}$
1113		acquisition on pixel $p$ in meters.
1114	$\hat{\phi}_{trop}^i(p)$	Estimated phase of the relative double path tropospheric delay between the $i_{th}$ and
1115		the $I_{st}$ acquisition on pixel $p$ with respect to pixel $ref$ .
1116	$\sigma_{\Delta\phi_j}^2$	Variance of the interferometric phase of the $j_{th}$ interferogram.
1117	$\gamma^j$	Spatial coherence of $j_{th}$ interferogram.
1118	$\gamma_{temp}$	Temporal coherence.
1119	$\lambda$	Radar wavelength in meters.
1120	$z_\epsilon$	Topographic residual in meters.

## 1121 **Reference**

- 1122 Agram, P. S., R. Jolivet, B. Riel, Y. N. Lin, M. Simons, E. Hetland, M. P. Doin, and C. Lasserre, 2013. New Radar  
1123 Interferometric Time Series Analysis Toolbox Released, *Eos, Transactions American Geophysical Union*, 94(7),  
1124 69-70, doi :10.1002/2013EO070001.

1125 Agram, P., and M. Simons, 2015. A noise model for InSAR time series, *Journal of Geophysical Research: Solid*  
1126 *Earth*, 120(4), 2752-2771, doi:10.1002/2014JB011271.

1127 Andersen, M., J. Dahl, Z. Liu, and L. Vandenberghe, 2011. Interior-point methods for large-scale cone  
1128 programming, in *Optimization for machine learning*, edited by S. Sra, S. Nowozin and S. J. Wright, MIT Press.

1129 Ansari, H., F. D. Zan, and R. Bamler, 2017. Sequential Estimator: Toward Efficient InSAR Time Series Analysis,  
1130 *IEEE Transactions on Geoscience and Remote Sensing*, 55(10), 5637-5652, doi:10.1109/TGRS.2017.2711037.

1131 Ansari, H., F. D. Zan, and R. Bamler, 2018. Efficient Phase Estimation for Interferogram Stacks, *IEEE Transactions*  
1132 *on Geoscience and Remote Sensing*, 56(7), 4109-4125, doi:10.1109/TGRS.2018.2826045.

1133 Bagnardi, M., and A. Hooper, 2018. Inversion of Surface Deformation Data for Rapid Estimates of Source  
1134 Parameters and Uncertainties: A Bayesian Approach, *Geochemistry, Geophysics, Geosystems*, 19,  
1135 doi:10.1029/2018GC007585.

1136 Baran, I., M. Stewart, and S. Claessens, 2005. A new functional model for determining minimum and maximum  
1137 detectable deformation gradient resolved by satellite radar interferometry, *IEEE Transactions on Geoscience and*  
1138 *Remote Sensing*, 43(4), 675-682, doi:10.1109/TGRS.2004.843187.

1139 Bekaert, D. P. S., A. Hooper, and T. J. Wright, 2015. A spatially-variable power-law tropospheric correction  
1140 technique for InSAR data, *Journal of Geophysical Research: Solid Earth*, 120(2), 1345-1356,  
1141 doi:10.1002/2014JB011558.

1142 Berardino, P., G. Fornaro, R. Lanari, and E. Sansosti, 2002. A new algorithm for surface deformation monitoring  
1143 based on small baseline differential SAR interferograms, *Geoscience and Remote Sensing, IEEE Transactions*  
1144 *on*, 40(11), 2375-2383, doi:10.1109/TGRS.2002.803792.

1145 Biggs, J., T. Wright, Z. Lu, and B. Parsons, 2007. Multi-interferogram method for measuring interseismic  
1146 deformation: Denali Fault, Alaska, *Geophysical Journal International*, 170(3), 1165-1179, doi:10.1111/j.1365-  
1147 246X.2007.03415.x.

1148 Blewitt, G., W.C. Hammond, C. Kreemer, 2018. Harnessing the GPS Data Explosion for Interdisciplinary Science,  
1149 *Eos*, 99, doi:10.1029/2018EO104623.

1150 Cao, N., H. Lee, and H. C. Jung, 2015. Mathematical Framework for Phase-Triangulation Algorithms in  
1151 Distributed-Scatterer Interferometry, *IEEE Geoscience and Remote Sensing Letters*, 12(9), 1838-1842,  
1152 doi:10.1109/LGRS.2015.2430752.

1153 Carballo, G. F., and P. W. Fieguth, 2002. Hierarchical network flow phase unwrapping, *IEEE Transactions on*  
1154 *Geoscience and Remote Sensing*, 40(8), 1695-1708, doi:10.1109/TGRS.2002.800279.

1155 Chaussard, E., F. Amelung, and Y. Aoki, 2013. Characterization of open and closed volcanic systems in Indonesia  
1156 and Mexico using InSAR time series, *Journal of Geophysical Research: Solid Earth*, 118(8), 3957-3969,  
1157 doi:10.1002/jgrb.50288.

1158 Chaussard, E., R. Bürgmann, H. Fattahi, R. M. Nadeau, T. Taira, C. W. Johnson, and I. Johanson, 2015. Potential  
1159 for larger earthquakes in the East San Francisco Bay Area due to the direct connection between the Hayward and  
1160 Calaveras Faults, *Geophysical Research Letters*, 42(8), 2734-2741, doi:10.1002/2015GL063575.

1161 Chen, C. W., and H. A. Zebker, 2001. Two-dimensional phase unwrapping with use of statistical models for cost  
1162 functions in nonlinear optimization, *JOSA A*, 18(2), 338-351, doi:10.1364/JOSAA.18.000338.

1163 Chen, C. W., and H. A. Zebker, 2002. Phase unwrapping for large SAR interferograms: statistical segmentation and  
1164 generalized network models, *Geoscience and Remote Sensing, IEEE Transactions on*, 40(8), 1709-1719,  
1165 doi:10.1109/TGRS.2002.802453.

1166 Cormen, T. H., C. E. Leiserson, R. L. Rivest, and C. Stein, 2009. *Introduction to algorithms*, MIT press. Chap. 22.2

1167 De Zan, F., A. Parizzi, P. Prats-Iraola, and P. López-Dekker, 2014. A SAR Interferometric Model for Soil Moisture,  
1168 *IEEE Transactions on Geoscience and Remote Sensing*, 52(1), 418-425, doi:10.1109/TGRS.2013.2241069.

1169 De Zan, F., and G. Gomba, 2018. Vegetation and soil moisture inversion from SAR closure phases: First  
1170 experiments and results, *Remote Sensing of Environment*, 217, 562-572, doi:10.1016/j.rse.2018.08.034.

1171 DiCaprio, C. J., and M. Simons, 2008. Importance of ocean tidal load corrections for differential InSAR,  
1172 *Geophysical Research Letters*, 35(22), doi:10.1029/2008GL035806.

1173 Doin, M. P., C. Lasserre, G. Peltzer, O. Cavalié, and C. Doubre, 2009. Corrections of stratified tropospheric delays  
1174 in SAR interferometry: Validation with global atmospheric models, *Journal of Applied Geophysics*, 69(1), 35-50,  
1175 doi:10.1016/j.jappgeo.2009.03.010.

1176 Farr, T. G., et al., 2007. The Shuttle Radar Topography Mission, *Reviews of Geophysics*, 45(2),  
1177 doi:10.1029/2005RG000183.

1178 Fattahi, H., and F. Amelung, 2013. DEM Error Correction in InSAR Time Series, *Geoscience and Remote Sensing,*  
1179 *IEEE Transactions on*, 51(7), 4249-4259, doi:10.1109/TGRS.2012.2227761.

1180 Fattahi, H., and F. Amelung, 2014. InSAR uncertainty due to orbital errors, *Geophysical Journal International*,  
1181 199(1), 549-560, doi:10.1093/gji/ggu276.

1182 Fattahi, H., and F. Amelung, 2015. InSAR bias and uncertainty due to the systematic and stochastic tropospheric  
1183 delay, *Journal of Geophysical Research: Solid Earth*, 120(12), 8758-8773, doi:10.1002/2015JB012419.

1184 Fattahi, H., P. Agram, and M. Simons, 2016. A Network-Based Enhanced Spectral Diversity Approach for TOPS  
1185 Time-Series Analysis, *IEEE Transactions on Geoscience and Remote Sensing*, 55(2), 777-786,  
1186 doi:10.1109/TGRS.2016.2614925.

1187 Fattahi, H., M. Simons, and P. Agram, 2017. InSAR Time-Series Estimation of the Ionospheric Phase Delay: An  
1188 Extension of the Split Range-Spectrum Technique, *IEEE Transactions on Geoscience and Remote Sensing*,  
1189 55(10), 5984-5996, doi:10.1109/TGRS.2017.2718566.

1190 Ferretti, A., C. Prati, and F. Rocca, 2001. Permanent scatterers in SAR interferometry, *Geoscience and Remote*  
1191 *Sensing, IEEE Transactions on*, 39(1), 8-20, doi:10.1109/36.898661.

1192 Ferretti, A., A. Fumagalli, F. Novali, C. Prati, F. Rocca, and A. Rucci, 2011. A New Algorithm for Processing  
1193 Interferometric Data-Stacks: SqueeSAR, *Geoscience and Remote Sensing, IEEE Transactions on*, 49(9), 3460-  
1194 3470, doi:10.1109/tgrs.2011.2124465.

1195 Gomba, G., A. Parizzi, F. D. Zan, M. Eineder, and R. Bamler, 2016. Toward Operational Compensation of  
1196 Ionospheric Effects in SAR Interferograms: The Split-Spectrum Method, *IEEE Transactions on Geoscience and*  
1197 *Remote Sensing*, 54(3), 1446-1461, doi:10.1109/TGRS.2015.2481079.

1198 Guarnieri, A. M., and S. Tebaldini, 2007. Hybrid Cramér–Rao bounds for crustal displacement field estimators in  
1199 SAR interferometry, *Signal Processing Letters, IEEE*, 14(12), 1012-1015, doi:10.1109/LSP.2007.904705.

1200 Guarnieri, A. M., and S. Tebaldini, 2008. On the exploitation of target statistics for SAR interferometry applications,  
1201 *Geoscience and Remote Sensing, IEEE Transactions on*, 46(11), 3436-3443, doi:10.1109/TGRS.2008.2001756.

1202 Hanssen, R. F., 2001. *Radar interferometry: data interpretation and error analysis*, Kluwer Academic Pub,  
1203 Dordrecht, Netherlands.

1204 Hetland, E., P. Musé, M. Simons, Y. Lin, P. Agram, and C. DiCaprio, 2012. Multiscale InSAR time series (MInTS)  
1205 analysis of surface deformation, *Journal of Geophysical Research: Solid Earth*, 117(B2),  
1206 doi:10.1029/2011JB008731.

1207 Hooper, A., H. Zebker, P. Segall, and B. Kampes, 2004. A new method for measuring deformation on volcanoes and  
1208 other natural terrains using InSAR persistent scatterers, *Geophysical Research Letters*, 31(23), L23611,  
1209 doi:10.1029/2004GL021737.

1210 Hooper, A., P. Segall, and H. Zebker, 2007. Persistent scatterer interferometric synthetic aperture radar for crustal  
1211 deformation analysis, with application to Volcán Alcedo, Galápagos, *Journal of Geophysical Research: Solid*  
1212 *Earth*, 112(B7), doi:10.1029/2006JB004763.

1213 Hussain, E., A. Hooper, T. J. Wright, R. J. Walters, and D. P. S. Bekaert, 2016. Interseismic strain accumulation  
1214 across the central North Anatolian Fault from iteratively unwrapped InSAR measurements, *Journal of*  
1215 *Geophysical Research: Solid Earth*, 121(12), 9000-9019, doi:10.1002/2016JB013108.

1216 Jolivet, R., R. Grandin, C. Lasserre, M. P. Doin, and G. Peltzer, 2011. Systematic InSAR tropospheric phase delay  
1217 corrections from global meteorological reanalysis data, *Geophysical Research Letters*, 38(17), L17311,  
1218 doi:10.1029/2011GL048757.

1219 Jolivet, R., P. S. Agram, N. Y. Lin, M. Simons, M. P. Doin, G. Peltzer, and Z. Li, 2014. Improving InSAR geodesy  
1220 using global atmospheric models, *Journal of Geophysical Research: Solid Earth*, 119(3), 2324-2341,  
1221 doi:10.1002/2013JB010588.

1222 Lauknes, T. R., H. A. Zebker, and Y. Larsen, 2011. InSAR Deformation Time Series Using an  $L_1$ -Norm Small-  
1223 Baseline Approach, *IEEE Transactions on Geoscience and Remote Sensing*, 49(1), 536-546,  
1224 doi:10.1109/TGRS.2010.2051951.

1225 Li, Z., E. Fielding, P. Cross, and R. Preusker, 2009. Advanced InSAR atmospheric correction: MERIS/MODIS  
1226 combination and stacked water vapour models, *International Journal of Remote Sensing*, 30(13), 3343-3363,  
1227 doi:10.1080/01431160802562172.

1228 Liang, C., Z. Liu, E. J. Fielding, and R. Bürgmann, 2018. InSAR Time Series Analysis of L-Band Wide-Swath SAR  
1229 Data Acquired by ALOS-2, *IEEE Transactions on Geoscience and Remote Sensing*, 56(8), 4492-4506,  
1230 doi:10.1109/TGRS.2018.2821150.

1231 Lin, Y. n. N., M. Simons, E. A. Hetland, P. Muse, and C. DiCaprio, 2010. A multiscale approach to estimating  
1232 topographically correlated propagation delays in radar interferograms, *Geochemistry, Geophysics, Geosystems*,  
1233 11(9), doi:10.1029/2010GC003228.

1234 Lohman, R. B., and M. Simons, 2005. Some thoughts on the use of InSAR data to constrain models of surface  
1235 deformation: Noise structure and data downsampling, *Geochemistry, Geophysics, Geosystems*, 6(1),  
1236 doi:10.1029/2004GC000841.

1237 López-Quiroz, P., M.-P. Doin, F. Tupin, P. Briole, and J.-M. Nicolas, 2009. Time series analysis of Mexico City  
1238 subsidence constrained by radar interferometry, *Journal of Applied Geophysics*, 69(1), 1-15,  
1239 doi:10.1016/j.jappgeo.2009.02.006.

1240 Morrison, K., J. C. Bennett, M. Nolan, and R. Menon, 2011. Laboratory Measurement of the DInSAR Response to  
1241 Spatiotemporal Variations in Soil Moisture, *IEEE Transactions on Geoscience and Remote Sensing*, 49(10),  
1242 3815-3823, doi:10.1109/TGRS.2011.2132137.

1243 Onn, F., and H. A. Zebker, 2006. Correction for interferometric synthetic aperture radar atmospheric phase artifacts  
1244 using time series of zenith wet delay observations from a GPS network, *Journal of Geophysical Research: Solid  
1245 Earth*, 111(B9), n/a-n/a, doi:10.1029/2005JB004012.

1246 Parizzi, A., X. Cong, and M. Eineder, 2009. First Results from Multifrequency Interferometry. A comparison of  
1247 different decorrelation time constants at L, C, and X Band, *ESA Scientific Publications(SP-677)*, 1-5.

1248 Pepe, A., and R. Lanari, 2006. On the extension of the minimum cost flow algorithm for phase unwrapping of  
1249 multitemporal differential SAR interferograms, *Geoscience and Remote Sensing, IEEE Transactions on*, 44(9),  
1250 2374-2383, doi:10.1109/TGRS.2006.873207.

1251 Pepe, A., Y. Yang, M. Manzo, and R. Lanari, 2015. Improved EMCF-SBAS Processing Chain Based on Advanced  
1252 Techniques for the Noise-Filtering and Selection of Small Baseline Multi-Look DInSAR Interferograms,  
1253 *Geoscience and Remote Sensing, IEEE Transactions on*, PP(99), 1-24, doi:10.1109/TGRS.2015.2396875.

1254 Perissin, D., and T. Wang, 2012. Repeat-pass SAR interferometry with partially coherent targets, *Geoscience and  
1255 Remote Sensing, IEEE Transactions on*, 50(1), 271-280, doi:10.1109/tgrs.2011.2160644.

1256 Rocca, F., 2007. Modeling interferogram stacks, *IEEE Transactions on Geoscience and Remote Sensing*, 45(10),  
1257 3289-3299, doi:10.1109/TGRS.2007.902286.

1258 Rosen, P. A., S. Hensley, G. Peltzer, and M. Simons, 2004. Updated repeat orbit interferometry package released,  
1259 *Eos Trans. AGU*, 85(5), 47-47, doi:10.1029/2004EO050004.

1260 Rosen, P. A., E. Gurrola, G. F. Sacco, and H. Zebker, 2012. The InSAR scientific computing environment, paper  
1261 presented at EUSAR 2012, 23-26 April 2012.

1262 Rodriguez, E., and J. Martin, 1992. Theory and design of interferometric synthetic aperture radars, paper presented  
1263 at IEE Proceedings F (Radar and Signal Processing), IET, doi:10.1049/ip-f-2.1992.0018.

1264 Rousseeuw, P. J., and M. Hubert, 2011. Robust statistics for outlier detection, *Wiley Interdisciplinary Reviews: Data  
1265 Mining and Knowledge Discovery*, 1(1), 73-79, doi:10.1002/widm.2.

1266 Samiei-Esfahany, S., J. E. Martins, F. v. Leijen, and R. F. Hanssen, 2016. Phase Estimation for Distributed  
1267 Scatterers in InSAR Stacks Using Integer Least Squares Estimation, *IEEE Transactions on Geoscience and*  
1268 *Remote Sensing*, 54(10), 5671-5687, doi:10.1109/TGRS.2016.2566604.

1269 Schmidt, D. A., and R. Bürgmann, 2003. Time-dependent land uplift and subsidence in the Santa Clara valley,  
1270 California, from a large interferometric synthetic aperture radar data set, *Journal of Geophysical Research: Solid*  
1271 *Earth*, 108(B9), doi:10.1029/2002JB002267.

1272 Seymour, M. S., and I. G. Cumming, 1994. Maximum likelihood estimation for SAR interferometry, paper  
1273 presented at Geoscience and Remote Sensing Symposium, 1994. IGARSS '94, 8-12 Aug 1994,  
1274 doi:10.1109/IGARSS.1994.399711.

1275 Tong, X., D. T. Sandwell, and B. Smith-Konter, 2013. High-resolution interseismic velocity data along the San  
1276 Andreas Fault from GPS and InSAR, *Journal of Geophysical Research: Solid Earth*, 118(1), 369-389,  
1277 doi:10.1029/2012JB009442.

1278 Tough, R. J. A., D. Blacknell, and S. Quegan, 1995. A Statistical Description of Polarimetric and Interferometric  
1279 Synthetic Aperture Radar Data, *Proceedings: Mathematical and Physical Sciences*, 449(1937), 567-589,  
1280 doi:10.1098/rspa.1995.0059.

1281 Werner, C., U. Wegmüller, T. Strozzi, and A. Wiesmann, 2000. Gamma SAR and interferometric processing  
1282 software, paper presented at *Proceedings of the ERS-Envisat symposium*, Gothenburg, Sweden.

1283 Xu, X., 2017. Earthquake Cycle Study with Geodetic Tools, Ph.D. Dissertation, University of California, San Diego,  
1284 La Jolla, CA, 181 pp.

1285 Yu, C., Z. Li, and N. T. Penna, 2018. Interferometric synthetic aperture radar atmospheric correction using a GPS-  
1286 based iterative tropospheric decomposition model, *Remote Sensing of Environment*, 204, 109-121,  
1287 doi:10.1016/j.rse.2017.10.038.

1288 Zebker, H. A., and J. Villasenor, 1992. Decorrelation in interferometric radar echoes, *Geoscience and Remote*  
1289 *Sensing, IEEE Transactions on*, 30(5), 950-959, doi:10.1109/36.175330.

1290



1 Supplementary Information for

2 **Small baseline InSAR time series analysis: unwrapping error**  
3 **correction and noise reduction**

4  
5 Zhang Yunjun<sup>a</sup>, Heresh Fattahi<sup>b</sup>, Falk Amelung<sup>a</sup>

6  
7 <sup>a</sup> Rosenstiel School of Marine and Atmospheric Science, University of Miami, Miami, Florida, USA

8 <sup>b</sup> Jet Propulsion Laboratory, California Institute of Technology, Pasadena, California, USA

9 **Content of this file**

10 Section S1. Supplemental figure S1 to S9 and table S1.

11 Section S2. Design matrices.

12 Section S3. Decorrelation noise simulation.

13 Section S4. Additional software features

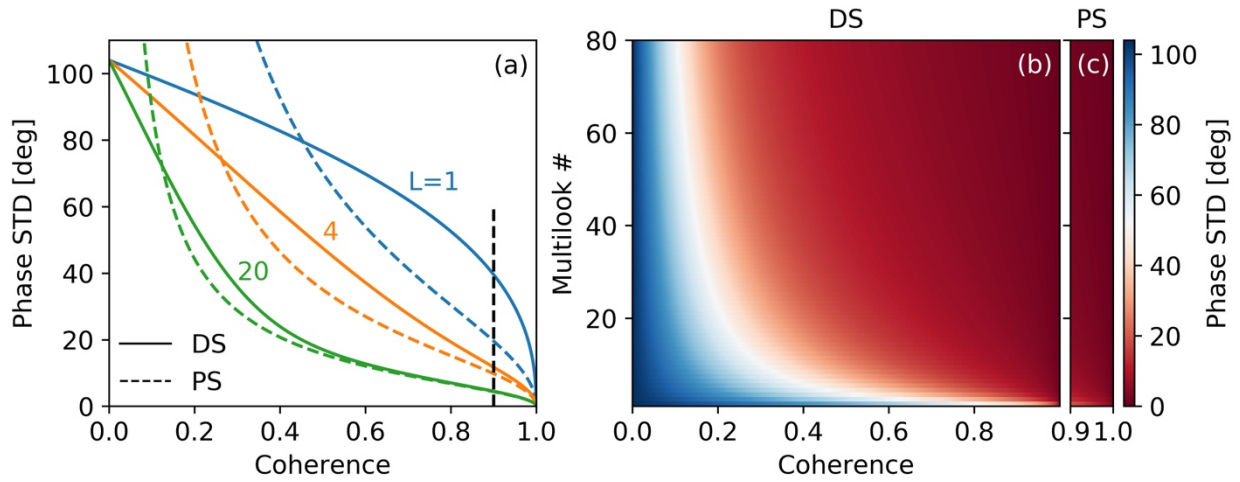
14 Supplemental references.

15 **S1. Supplemental figures and tables**

16 This section provides figures S1 to S9 and table S1. Fig. S1 shows the standard deviation of the  
17 interferometric phase as a function of the spatial coherence and number of looks. Fig. S2  
18 demonstrates the performance of four weighting functions in different temporal decorrelation  
19 settings using the mean RMSE of 10,000 realizations of the inverted phase time-series as a  
20 function of the number of looks. Fig. S3 demonstrates the simulation of the unwrapped  
21 interferogram for unwrapping error correction with the bridging method, considering the ground  
22 deformation, tropospheric turbulence, phase ramps and decorrelation noise. Fig. S4 shows the

23 output percentage of interferograms with unwrapping errors as a function of the LASSO  
24 parameter to find its suitable value range. Fig. S5 demonstrates the necessity of adding the step  
25 function during the topographic residual correction in the presence of displacement jump using  
26 both simulated and read data. Fig. S6 shows the coherence matrix of Sentinel-1 dataset for GPS  
27 stations within Sierra Negra. Fig. S7 shows the estimated residual phase time-series. Fig. S8  
28 shows the coherence-based network modification for the Sentinel-1 data used in the discussion  
29 of the network redundancy in section 6.3. Fig. S9 compares the displacement time-series from  
30 the approaches in GIANt and MintPy with and without unwrapping error correction and  
31 weighted network inversion. Table S1 summaries the information of SAR data used in the paper  
32 and their configurations for InSAR stack processing.

33



34

35 **Figure S1.** Phase standard deviation versus spatial coherence for PS and DS. Related to equation

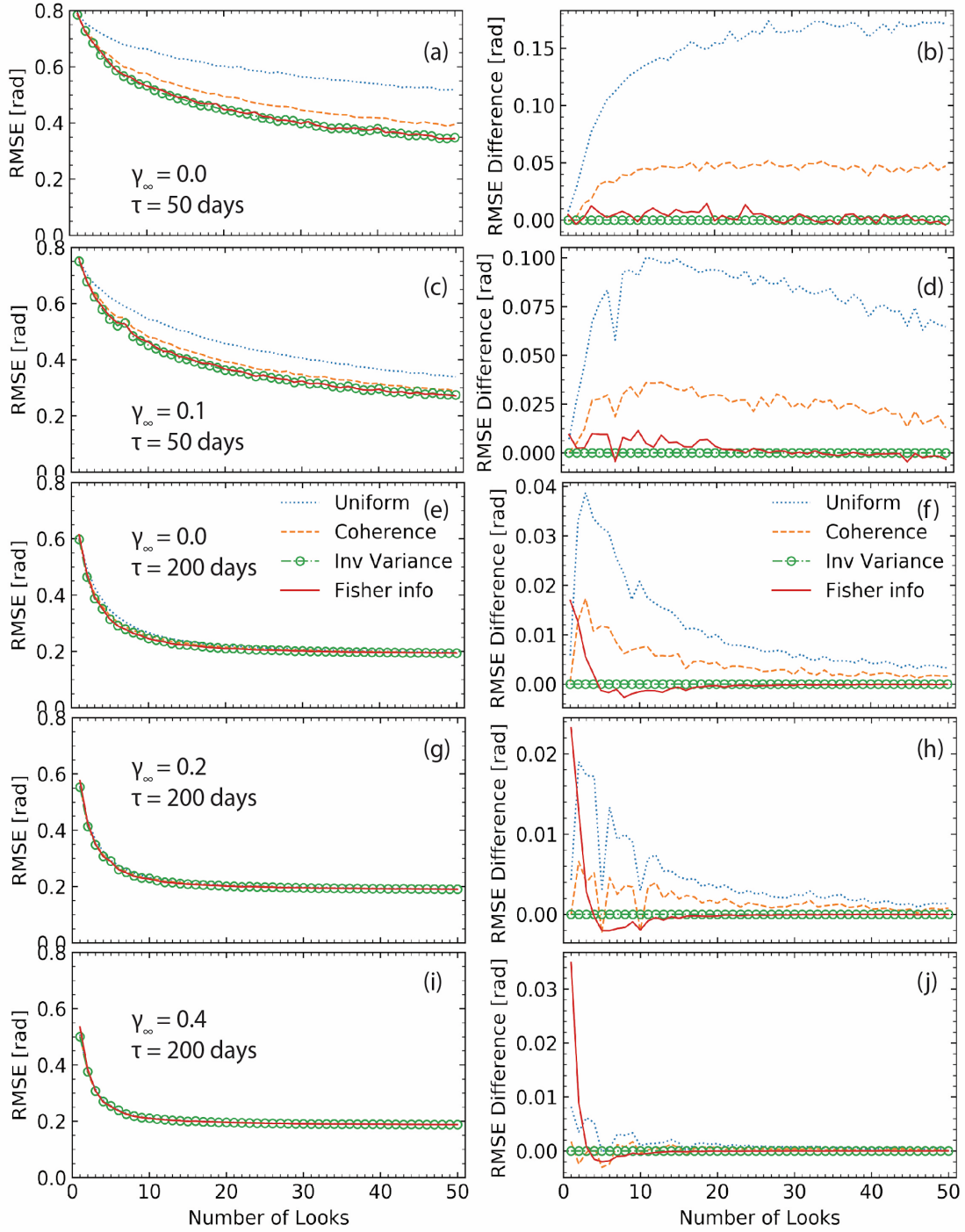
36 (6). (a) Standard deviation of interferometric phase as function of coherence for DS (solid lines)

37 and PS (dashed lines) with 1, 4 and 20 looks. The black dashed line marks the effective boundary

38 for PS ( $0.9 < |\gamma| \leq 1$ ). (b) Lookup table to convert spatial coherence to phase standard deviation

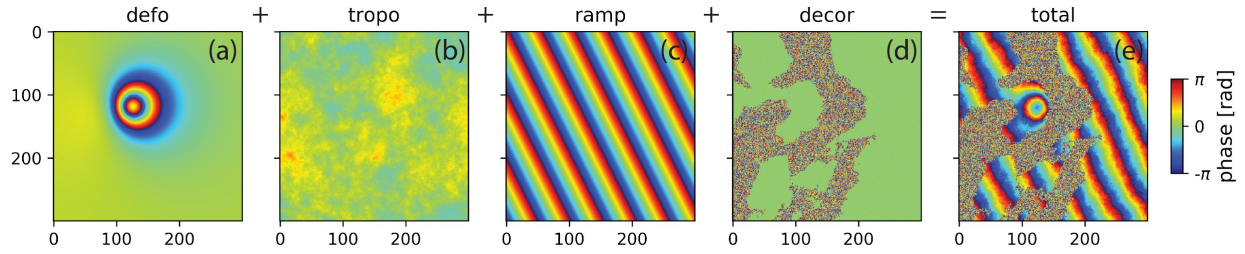
39 for number of looks in  $[1, 80]$ .

40



41

42 **Figure S2.** Performance indicator for four weighting functions based on (left panel) the mean  
 43 RMSE of 10,000 realizations of inverted phase time-series as a function of the number of looks.  
 44 Related to Fig. 1. Right panel: same as left panel but shown in differential RMSE with respect to  
 45 inverse-variance weighting. From top to bottom for different temporal decorrelation settings.



46

47 **Figure S3.** Simulate interferogram for unwrapping error correction with the bridging method.

48 Related to Fig. 2. We consider an area of 300 by 300 pixels with spatial resolution of 62 m in

49 both directions, illustrated by radar echoes in a Sentinel-1-like geometry in descending orbit

50 (with an incidence angle of 34 deg and heading angle of -168 deg). (a) Deformation phase

51 caused by a Mogi source ( $x = 120$  row,  $y = 120$  col,  $z = 2$  km under the surface with a volume

52 change of  $10^6$  m<sup>3</sup>), (b) tropospheric turbulence modeled as an isotropic two-dimensional surface

53 with a power law behavior (the multiplier of spectrum amplitude  $p_0=1e-3$ , assuming a flat area

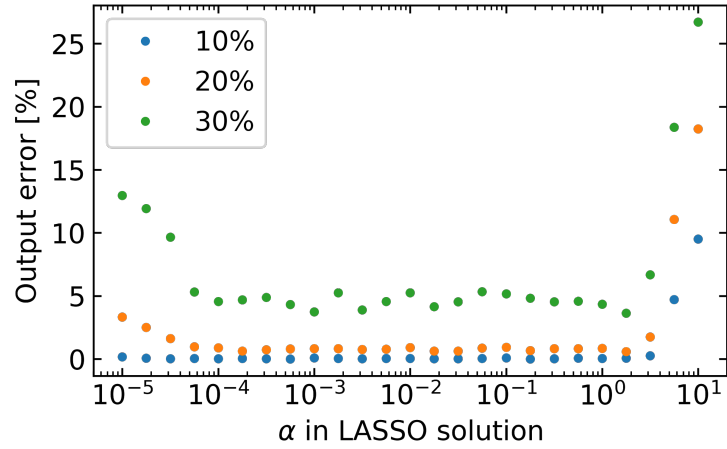
54 without stratified tropospheric delay; Hanssen, 2001), (c) phase ramp modeled as a linear

55 surface, and (d) simulated decorrelation noise (see section S3). The water body mask is rescaled

56 from the real DEM in western Kyushu, Japan. We specify the spatial coherence of 0.6 and 0.001

57 for pixels on land and water respectively with the number of looks of 15 by 5.

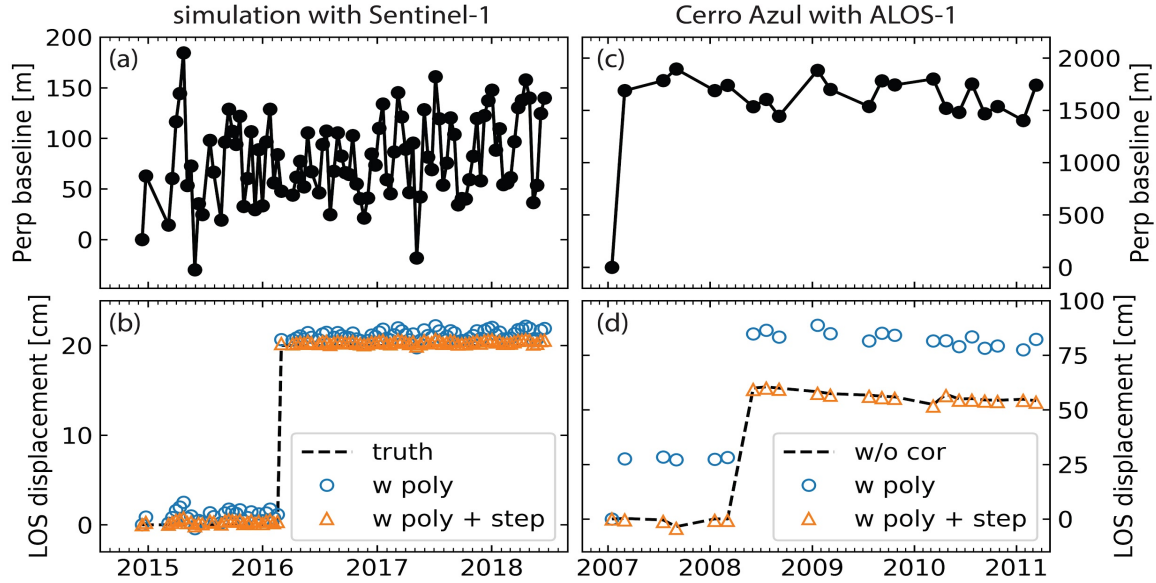
58



59

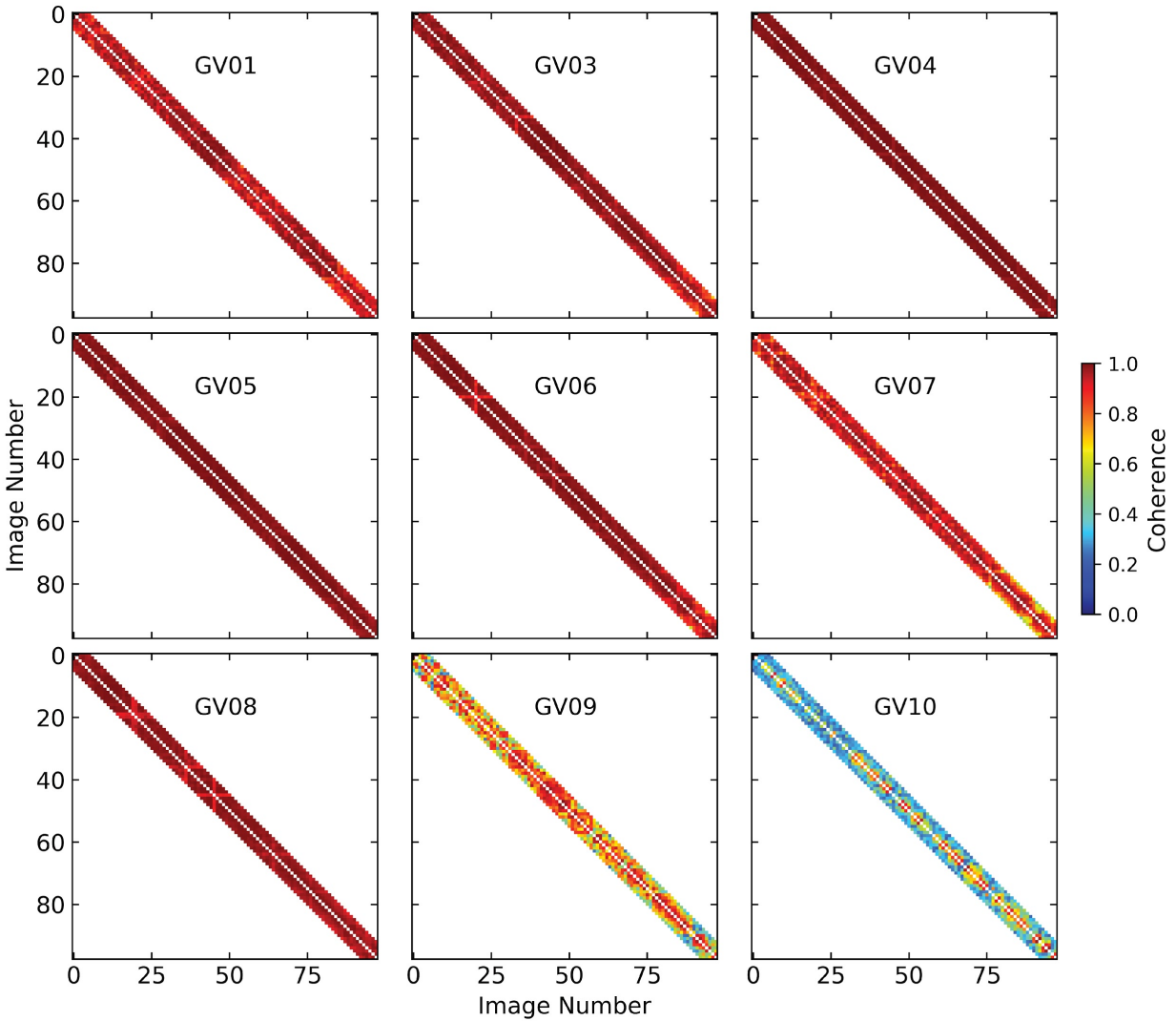
60 **Figure S4.** Optimal LASSO parameter  $\alpha$ . Related to equation (11) and Fig. 4. Mean output  
 61 percentage of 100 realization of interferograms with unwrapping errors after correction as a  
 62 function of the nonnegative  $\alpha$  value for different input percentage of interferograms with  
 63 unwrapping errors. The network of interferograms is the same as Fig. 4a. The simulation result  
 64 shows that any number of  $\alpha$  in  $[10^{-4}, 10^0]$  works. We choose  $10^{-2}$  as default value.

65



66

67 **Figure S5.** Illustration of the step function in topographic residual correction in presence of  
68 displacement jumps. Related to equation (13) in section 4.8. (a and b) Perpendicular baseline  
69 history (from the Sentinel-1 data of section 5) and an arbitrary displacement time-series using  
70 simulated data (with a permanent displacement jump at 1 March 2016 with a magnitude of 20  
71 cm, shown as the dashed black line in (b), in addition to the topographic residual contribution  
72 from a DEM error of 50 m). Blue empty circles and orange triangles represent displacement  
73 time-series after topographic residual correction assuming quadratic model without and with a  
74 step function, respectively. (c and d) Same as (a and b) but (i) using ALOS-1 data for one pixel  
75 on Cerro Azul located at  $[W91.270^\circ, S0.928^\circ]$  and (ii) the black dashed line for the displacement  
76 time-series without topographic residual correction. In both simulated and real data, the  
77 disagreement between the low-frequency quadratic model and the high-frequency displacement  
78 jump leads to biased estimation of the topographic residual (Du et al., 2007) and adding a step  
79 function could effectively eliminate this estimation bias. This estimation bias is amplified in the  
80 first ALOS-1 acquisition by its large perpendicular baseline (the difference between black  
81 dashed line and the blue empty circles in (d)).

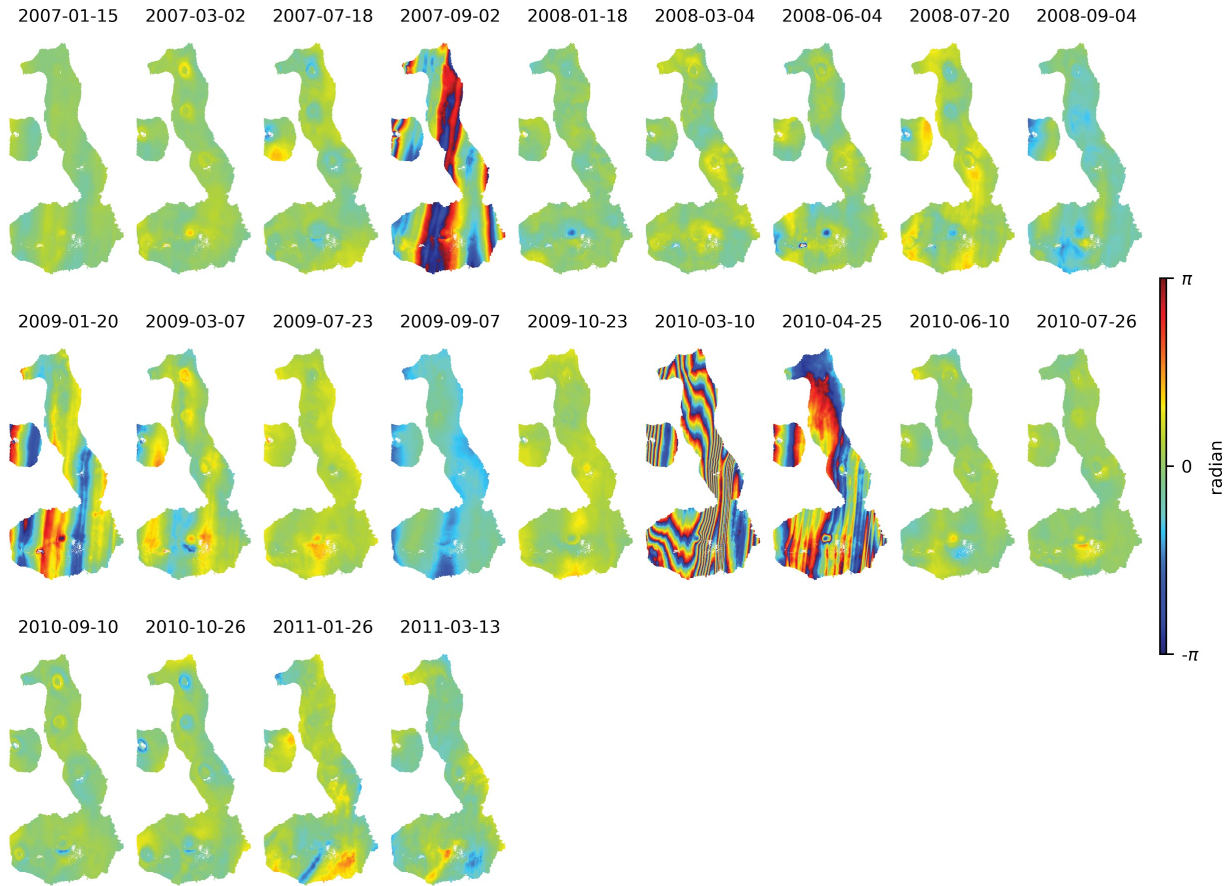


82

83 **Figure S6.** Coherence matrix of Sentinel-1 dataset for GPS stations within Sierra Negra. Related  
 84 to Fig. 8 in section 5.1. Both X and Y axis indicate number of SAR acquisitions. Station GV10 is  
 85 located in a densely vegetated area outside the caldera on the rim, resulting in fast decorrelation  
 86 with low spatial coherence on interferograms with more than 2 lags.

87

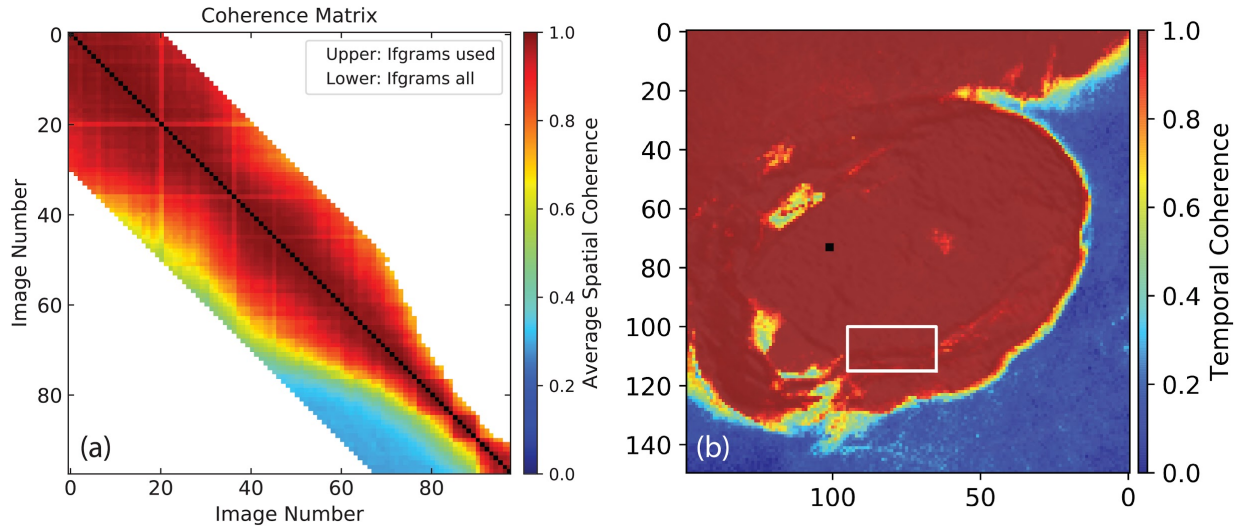




88

89 **Figure S7.** The estimated residual phase time-series  $\hat{\phi}_{resid}$  of ALOS-1 dataset. Related to  
 90 equation (13-14) in section 4.7 and Fig. 12 in section 5.4. A quadratic phase ramp has been  
 91 estimated and removed from each acquisition. This is used in equation (14) to calculate the  
 92 residual phase RMS value. Phases on 2 September 2007, 10 March 2010 and 25 April 2010 are  
 93 severely contaminated by ionospheric streaks and are automatically identified as outliers. Phase  
 94 on 2- January 2009 is contaminated by ionosphere also but is not identified as outlier due to its  
 95 relatively small magnitude.

96



97

98 **Figure S8.** Coherence-based network modification for Sentinel-1 data used in section 6.3 in

99 Sierra Negra. Related to Fig. 14 in section 6.3. (a) Coherence matrix of the customized area of

100 interest along the trap door fault within Sierra Negra caldera (marked by the white rectangle in

101 (b)). The upper triangle shows the interferogram kept after the network modification; while the

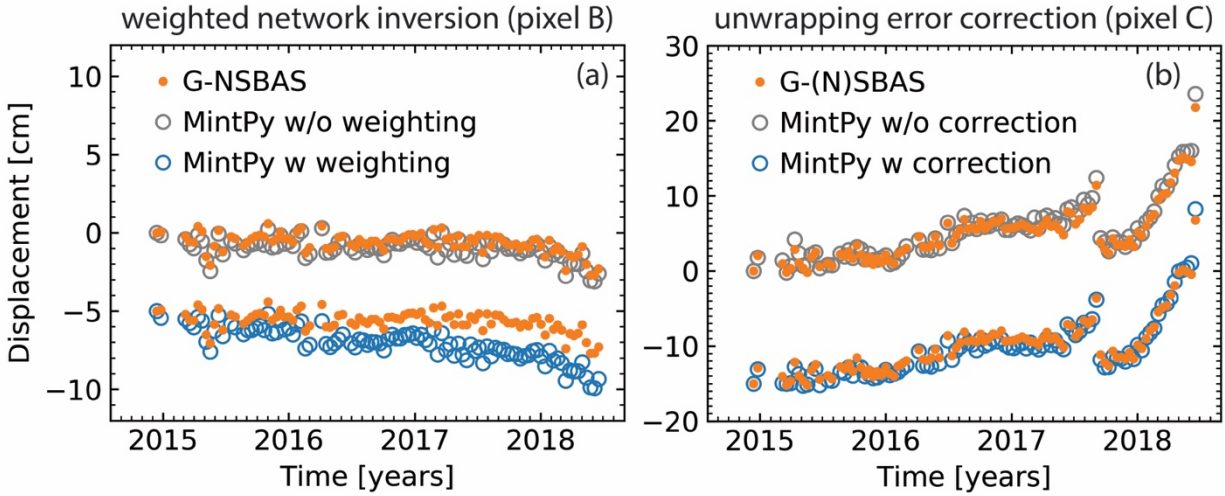
102 lower triangle shows all the generated interferograms. A network of interferograms with 30

103 sequential connections (2475 in total) are generated from 98 SAR acquisitions. A maximum of

104 20 connections are shown in Fig. 14 only. (b) Temporal coherence of the network inversion from

105 the interferogram stack with a maximum of 20 connections.

106



107

108 **Figure S9.** Impact of (a) weighted network inversion and (b) unwrapping error correction on the  
 109 displacement time-series. Related to Fig. 16 in section 6.5. The comparison within (a) shows that  
 110 the difference on pixel B (Alcedo's flank) between MintPy and G-NSBAS is caused by the  
 111 weighting during the network inversion. The comparison within (b) shows that the difference on  
 112 pixel C (Fernandina's crater) between MintPy and G-(N)SBAS is caused by the unwrapping  
 113 error correction.

114

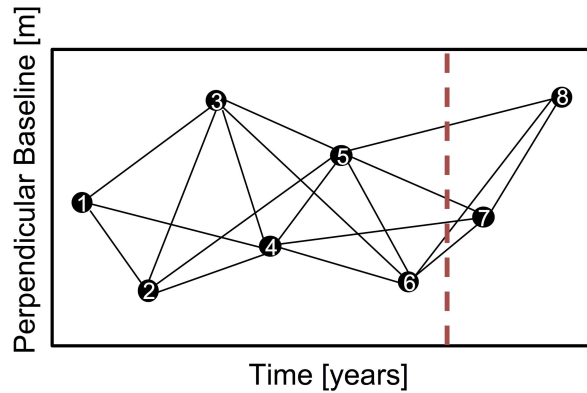
115 **Table S1.** SAR dataset information with parameters used in InSAR stack processing

Satellite	ALOS-1	Sentinel-1A/B
Orbit direction	Ascending	Descending
Track number	133	128 (swath 1 & 2)
Start / end date (# of acquisitions)	2007-01-15 / 2011-03-13 (22)	2014-12-13 / 2018-06-19 (98)
Network selection criteria (# of Interferograms)	$B_{temp} \leq 1800$ days $B_{\perp} \leq 1800$ m (228)	Sequential with 5 connections (475)
# of looks in range / azimuth direction	$8 \times 16$	$15 \times 5$
Ground pixel size in range / azimuth direction (m)	$60 \times 51$	$62 \times 70$
InSAR Processor	ROI_PAC	ISCE
Phase Unwrapping	SNAPHU	SNAPHU

116

## 117 S2. Design matrices

118 This section shows examples to generate the design matrices used in the software. A demo set of  
119  $N = 8$  SAR images acquired at  $[t_1, \dots, t_8]$  is used as the example. A stack of  $M = 18$  interferograms  
120 is selected using the sequential method with 3 connections. An earthquake or volcanic eruption  
121 event occurred between  $t_6$  and  $t_7$  (red dashed line), which caused a permanent ground  
122 displacement offset.



123

124 **Figure S10.** Network configuration of the demo dataset. Red dashed line marks the time of a  
125 displacement offset due to an earthquake or volcanic eruption.

### 126 S2.1 Network inversion

127 To generate the design matrix  $\mathbf{A}$  for network inversion used in equation (1) in section 2.1, we  
128 first generate a  $M \times N$  matrix. For each row, it consists -1, 0 and 1 with -1 for the reference  
129 acquisition, 1 for the secondary acquisition and 0 for the rest. Due to the relative nature of  
130 InSAR measurement, the phase on the reference date (the first date by default) cannot be  
131 resolved, thus, we can only solve  $[\phi^2, \dots, \phi^N]$  instead of  $[\phi^1, \dots, \phi^N]$  and the corresponding  
132 column (the first column by default) is eliminated in the design matrix  $\mathbf{A}$ , which results in size of  
133  $M \times (N - 1)$ .

134

135

$$\mathbf{A} = \begin{bmatrix} -1 & 1 & 0 & 0 & 0 & 0 & 0 & 0 \\ -1 & 0 & 1 & 0 & 0 & 0 & 0 & 0 \\ -1 & 0 & 0 & 1 & 0 & 0 & 0 & 0 \\ 0 & -1 & 1 & 0 & 0 & 0 & 0 & 0 \\ 0 & -1 & 0 & 1 & 0 & 0 & 0 & 0 \\ 0 & -1 & 0 & 0 & 1 & 0 & 0 & 0 \\ 0 & 0 & -1 & 1 & 0 & 0 & 0 & 0 \\ 0 & 0 & -1 & 0 & 1 & 0 & 0 & 0 \\ 0 & 0 & -1 & 0 & 0 & 1 & 0 & 0 \\ 0 & 0 & 0 & -1 & 1 & 0 & 0 & 0 \\ 0 & 0 & 0 & -1 & 0 & 1 & 0 & 0 \\ 0 & 0 & 0 & -1 & 0 & 0 & 1 & 0 \\ 0 & 0 & 0 & 0 & -1 & 1 & 0 & 0 \\ 0 & 0 & 0 & 0 & -1 & 0 & 1 & 0 \\ 0 & 0 & 0 & 0 & -1 & 0 & 0 & 1 \\ 0 & 0 & 0 & 0 & 0 & -1 & 1 & 0 \\ 0 & 0 & 0 & 0 & 0 & -1 & 0 & 1 \\ 0 & 0 & 0 & 0 & 0 & 0 & -1 & 1 \end{bmatrix} \tag{S1}$$

136

137 **S2.2 Phase closure of interferograms triplets**

138 Design matrix  $\mathbf{C}$  describe the combination of interferograms to form the triplets used in equation  
 139 (10) in section 3.2 for the phase closure unwrapping error correction. An example of  $\mathbf{C}$  is shown  
 140 below based on the demo network with number of triplets  $T = 16$ .

141

142  $[ 1 -1 0 1 0 0 0 0 0 0 0 0 0 0 0 0 0 ]$

143  $[ 1 0 -1 0 1 0 0 0 0 0 0 0 0 0 0 0 0 ]$

144  $[ 0 1 -1 0 0 0 1 0 0 0 0 0 0 0 0 0 0 ]$

145  $[ 0 0 0 1 -1 0 1 0 0 0 0 0 0 0 0 0 0 ]$

146  $[ 0 0 0 1 0 -1 0 1 0 0 0 0 0 0 0 0 0 ]$

147  $[ 0 0 0 0 1 -1 0 0 0 1 0 0 0 0 0 0 0 ]$

148  $[ 0 0 0 0 0 0 1 -1 0 1 0 0 0 0 0 0 0 ]$

149  $\mathbf{C} = [ 0 0 0 0 0 0 1 0 -1 0 1 0 0 0 0 0 0 ] \tag{S2}$

$$\begin{aligned}
150 & \quad [0 \ 0 \ 0 \ 0 \ 0 \ 0 \ 0 \ 0 \ 1 \ -1 \ 0 \ 0 \ 0 \ 1 \ 0 \ 0 \ 0 \ 0 \ 0] \\
151 & \quad [0 \ 0 \ 0 \ 0 \ 0 \ 0 \ 0 \ 0 \ 0 \ 0 \ 1 \ -1 \ 0 \ 1 \ 0 \ 0 \ 0 \ 0 \ 0] \\
152 & \quad [0 \ 0 \ 0 \ 0 \ 0 \ 0 \ 0 \ 0 \ 0 \ 0 \ 1 \ 0 \ -1 \ 0 \ 1 \ 0 \ 0 \ 0 \ 0] \\
153 & \quad [0 \ 0 \ 0 \ 0 \ 0 \ 0 \ 0 \ 0 \ 0 \ 0 \ 0 \ 1 \ -1 \ 0 \ 0 \ 0 \ 1 \ 0 \ 0] \\
154 & \quad [0 \ 0 \ 0 \ 0 \ 0 \ 0 \ 0 \ 0 \ 0 \ 0 \ 0 \ 0 \ 1 \ -1 \ 0 \ 1 \ 0 \ 0] \\
155 & \quad [0 \ 0 \ 0 \ 0 \ 0 \ 0 \ 0 \ 0 \ 0 \ 0 \ 0 \ 0 \ 0 \ 1 \ 0 \ -1 \ 0 \ 1 \ 0] \\
156 & \quad [0 \ 0 \ 0 \ 0 \ 0 \ 0 \ 0 \ 0 \ 0 \ 0 \ 0 \ 0 \ 0 \ 0 \ 1 \ -1 \ 0 \ 0 \ 1] \\
157 & \quad [0 \ 0 \ 0 \ 0 \ 0 \ 0 \ 0 \ 0 \ 0 \ 0 \ 0 \ 0 \ 0 \ 0 \ 0 \ 1 \ -1 \ 1] \\
158 &
\end{aligned}$$

### 159 S2.3 Topographic residual correction

160 Design matrix  $\mathbf{G}$  is used in equation (13) for topographic residual correction in section 4.8. It is  
161 in size of  $N \times (1 + N_{poly} + N_{step})$ , where  $N_{poly}$  is the user-defined polynomial order  $N_{poly}$  (2 by  
162 default),  $N_{step}$  is the number of Heaviside step functions (0 by default) describing offsets at  
163 specific prior selected times. An example of  $\mathbf{G}$  is shown below based on the demo network.

$$\begin{aligned}
164 & \\
165 & \quad \mathbf{G} = \begin{bmatrix} \frac{4\pi}{\lambda} \frac{B_{\perp}^1}{r \sin(\theta)} & 1 & (t_1 - t_1) & \frac{(t_1 - t_1)^2}{2} & 0 \\ \frac{4\pi}{\lambda} \frac{B_{\perp}^2}{r \sin(\theta)} & 1 & (t_2 - t_1) & \frac{(t_2 - t_1)^2}{2} & 0 \\ \frac{4\pi}{\lambda} \frac{B_{\perp}^3}{r \sin(\theta)} & 1 & (t_3 - t_1) & \frac{(t_3 - t_1)^2}{2} & 0 \\ \frac{4\pi}{\lambda} \frac{B_{\perp}^4}{r \sin(\theta)} & 1 & (t_4 - t_1) & \frac{(t_4 - t_1)^2}{2} & 0 \\ \frac{4\pi}{\lambda} \frac{B_{\perp}^5}{r \sin(\theta)} & 1 & (t_5 - t_1) & \frac{(t_5 - t_1)^2}{2} & 0 \\ \frac{4\pi}{\lambda} \frac{B_{\perp}^6}{r \sin(\theta)} & 1 & (t_6 - t_1) & \frac{(t_6 - t_1)^2}{2} & 0 \\ \frac{4\pi}{\lambda} \frac{B_{\perp}^7}{r \sin(\theta)} & 1 & (t_7 - t_1) & \frac{(t_7 - t_1)^2}{2} & 1 \\ \frac{4\pi}{\lambda} \frac{B_{\perp}^8}{r \sin(\theta)} & 1 & (t_8 - t_1) & \frac{(t_8 - t_1)^2}{2} & 1 \end{bmatrix} \quad (S3)
\end{aligned}$$

166

167 Then equation (13) can be formed as a linear system with  $N$  equations as below:

168

$$169 \quad \hat{\phi} - \hat{\phi}_{tropo} = \mathbf{G}X + \phi_{resid} \quad (S4)$$

170

171 where  $X = [z_\varepsilon, c_0, c_1, c_2, s_7]^T$  is the vector of unknown parameters,  $\hat{\phi}$ ,  $\hat{\phi}_{tropo}$  and  $\phi_{resid}$  are the  
172  $N \times 1$  inverted raw phase time-series, estimated tropospheric delay time-series and residual  
173 phase time-series, respectively. We apply the least squares estimation to obtain the solution as:

174

$$175 \quad \hat{X} = (\mathbf{G}^T \mathbf{G})^{-1} \mathbf{G}^T (\hat{\phi} - \hat{\phi}_{tropo}) \quad (S5)$$

$$176 \quad \hat{\phi}_{resid} = \hat{\phi} - \hat{\phi}_{tropo} - \mathbf{G}\hat{X} \quad (S6)$$

177

178 The estimated residual phase  $\hat{\phi}_{resid}$  is used to characterize the noise of phase time-series using  
179 equation (14) in section 4.9. The noise-reduced displacement time-series is given as:

180

$$181 \quad \phi_{dis}^i = \hat{\phi}^i - \hat{\phi}_{tropo}^i - \frac{-4\pi}{\lambda} \frac{B_\perp^i}{r \sin(\theta)} \hat{z}_\varepsilon \quad (S7)$$

182

183 where  $i = 1, \dots, N$  and  $\hat{z}_\varepsilon$  is the estimated DEM error in  $\hat{X}$ .

## 184 **S2.4 Average velocity estimation**

185 For each pixel, the average velocity is estimated as  $d^i = vt_i + c$ , where  $d^i = -\frac{\lambda}{4\pi} \phi_{dis}^i$  is the  
186 displacement at  $t_i$  in meters,  $v$  is the unknown velocity and  $c$  is the unknown offset. The solution



187 can be obtained using least squares approximation. An example of the design matrix  $E$  is shown  
 188 below based on the demo network.

189

190

$$E = \begin{bmatrix} t_1 - t_1 & 1 \\ t_2 - t_1 & 1 \\ t_3 - t_1 & 1 \\ t_4 - t_1 & 1 \\ t_5 - t_1 & 1 \\ t_6 - t_1 & 1 \\ t_7 - t_1 & 1 \\ t_8 - t_1 & 1 \end{bmatrix} \quad (\text{S8})$$

191

192 For linear displacement, the uncertainty of the estimated velocity  $\sigma_v$  is given by equation (10) in  
 193 Fattahi and Amelung (2015) as:

194

195

$$\sigma_v = \sqrt{\frac{\sum_{i=1}^N (\phi_{dis}^i - \hat{\phi}_{dis}^i)^2}{(N-2) \sum_{i=1}^N (t_i - \bar{t})^2}} \quad (\text{S9})$$

196

197 where  $\hat{\phi}_{dis}^i$  is the predicted linear displacement at  $i_{th}$  acquisition  $\bar{t}$  is the mean value of time in  
 198 years.

### 199 **S3. Decorrelation noise simulation**

#### 200 **S3.1 Coherence model**

201 We simulate the coherence for a stack of interferograms on one pixel using a decorrelation  
 202 model with exponential decay for temporal decorrelation. The spatial coherence  $\gamma^j$  of the  $j_{th}$   
 203 interferogram can be expressed as (Zebker and Villasenor, 1992; Hanssen, 2001; Parizzi et al.,  
 204 2009):

205

$$206 \quad \gamma = \gamma_{geom} \cdot \gamma_{DC} \cdot \gamma_{temporal} \quad (S10)$$

207

208 where  $\gamma_{geom}$  represents the geometric decorrelation,  $\gamma_{DC}$  represents the Doppler centroid  
 209 decorrelation,  $\gamma_{temporal}$  represents the temporal decorrelation, given by the equations below.

210 Note that the thermal decorrelation  $\gamma_{thermal}$  is served as the instantaneous decorrelation in  
 211 temporal decorrelation  $\gamma_{temporal}$  (Parizzi et al., 2009).

212

$$213 \quad \gamma_{geom} = \begin{cases} 1 - \frac{|B_{\perp}|}{B_{\perp}^{crit}}, & |B_{\perp}| \leq B_{\perp}^{crit} \\ 0, & |B_{\perp}| > B_{\perp}^{crit} \end{cases} \quad (S11)$$

$$214 \quad \gamma_{DC} = \begin{cases} 1 - \frac{|\Delta f_{DC}|}{B_{az}}, & |\Delta f_{DC}| \leq B_{az} \\ 0, & |\Delta f_{DC}| > B_{az} \end{cases} \quad (S12)$$

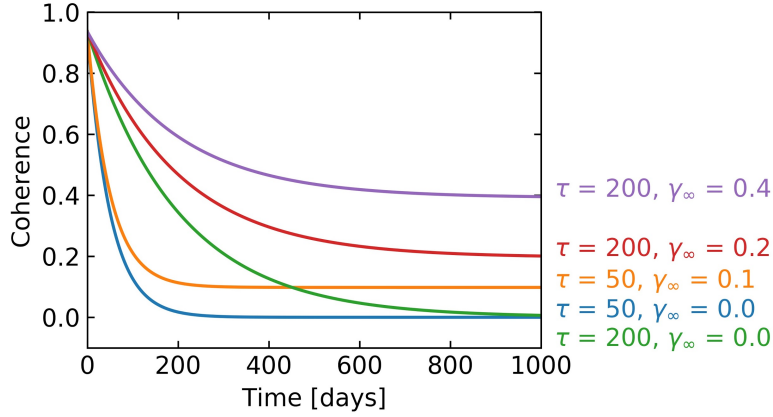
$$215 \quad \gamma_{temporal}(t) = (\gamma_{thermal} - \gamma_{\infty})e^{-t/\tau} + \gamma_{\infty} \quad (S13)$$

$$216 \quad \gamma_{thermal} = \frac{1}{1-SNR^{-1}} \quad (S14)$$

217

218 The critical perpendicular baseline  $B_{\perp}^{crit} = \lambda \frac{B_{rg}}{c} R \cdot \tan(\theta)$  is the baseline causing a spectral  
 219 shift equal to the radar bandwidth  $B_{rg}$  in range direction (Zebker and Villasenor, 1992; Hanssen,  
 220 2001), where  $\lambda$  is the radar wavelength,  $c$  is the speed of light,  $R$  is the distance between radar  
 221 antenna and ground target and  $\theta$  is the incidence angle,  $SNR$  is the thermal signal-to-noise ratio  
 222 of radar receiver.  $\tau$  is the time constant which depends on radar wavelength  $\lambda$ , it's the time for  
 223 coherence to drop down to  $1/e$ , i.e. 0.36, from its initial value (Parizzi et al., 2009; Rocca, 2007).  
 224  $\gamma_{\infty}$  is the long-term coherence, or minimum attainable coherence value, which converged over  
 225 time, usually with high value in urban area and low value in vegetated area. Note that this model

226 does not consider the seasonal behavior of temporal decorrelation, volume decorrelation, and  
 227 processing-induced decorrelation. For a given set of SAR acquisitions, the geometric and  
 228 Doppler centroid decorrelation is almost constant among all pixels. All parameters are deployed  
 229 with typical parameters of Sentinel-1 SAR sensor.  
 230



231  
 232 **Figure S11.** Simulated coherence as a function of temporal baseline, color coded by different  $\tau$   
 233 and  $\gamma_\infty$  setting used in Fig. S2.

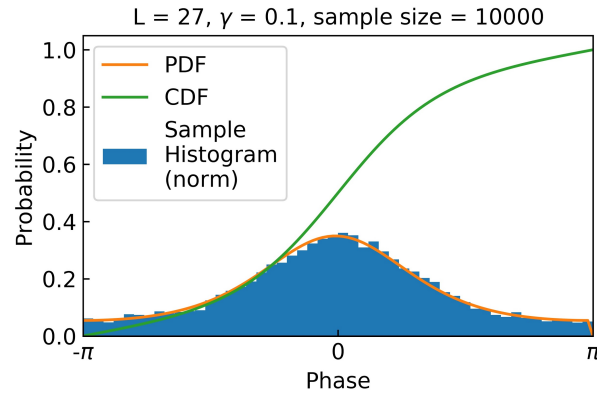
### 234 S3.2 Simulate decorrelation noise from coherence

235 For distributed scatterers (DS) in natural, vegetated terrain the interferometric phase exhibits  
 236 highly unpredictable speckle characteristics. Its phase can be appropriately modeled by a random  
 237 process, complex, stationary, circular Gaussian process in the case of SAR image. Applying the  
 238 central limit theorem, the probability density function  $pdf(\Delta\phi)$  of interferometric phase is  
 239 obtained using equation (66) from Tough et al., 1995; equation (4.2.23) from Hanssen, 2001):

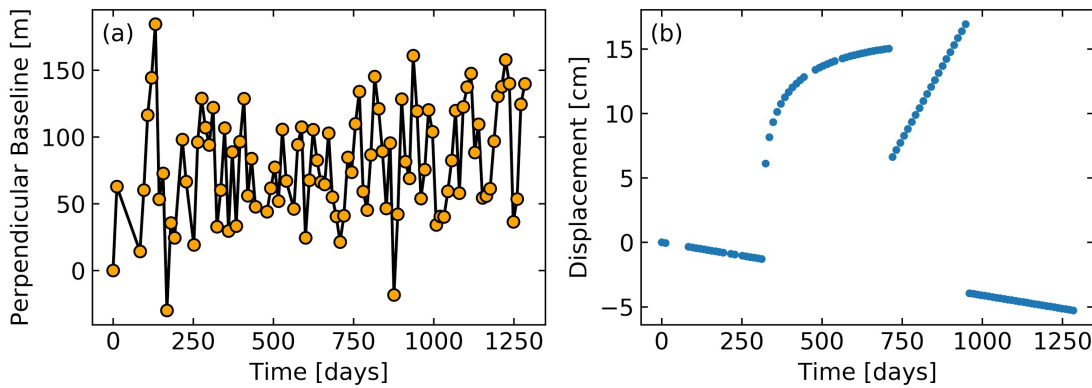
$$241 \quad pdf(\Delta\phi) = \frac{(1-|\gamma|^2)^L}{2\pi} \left\{ \frac{\Gamma(2L-1)}{[\Gamma(L)]^2 2^{2(L-1)}} \times \left[ \frac{(2L-1)\beta}{(1-\beta^2)^{L+\frac{1}{2}}} \left( \frac{\pi}{2} + \arcsin\beta \right) + \frac{1}{(1-\beta^2)^L} \right] + D \right\} \quad (S15)$$

$$242 \quad D = \frac{1}{2^{(L-1)}} \sum_{r=0}^{L-2} \frac{\Gamma(L-\frac{1}{2})}{\Gamma(L-\frac{1}{2}-r)} \frac{\Gamma(L-1-r)}{\Gamma(L-1)} \frac{1+(2r+1)\beta^2}{(1-\beta^2)^{r+2}}$$

243 where  $\beta = |\gamma| \cos(\Delta\phi - \Delta\phi_0)$ , expected interferometric phase  $\Delta\phi_0 = E\{\Delta\phi\}$ , gamma function  
 244  $\Gamma(L) = \int_0^\infty t^{L-1} e^{-t} dt$ , for  $L \in R$  and  $D$  a finite summation term. Note that  $D$  vanishes for  
 245 single-look datasets ( $L=1$ ).  
 246  
 247 The 10,000 realizations/samples of decorrelation noise of each interferogram (used in section  
 248 2.4) is simulated by generating a distribution given by equation (S15) with corresponding  
 249 coherence  $\gamma$  and number of looks  $L$ . One example with  $\gamma = 0.1$  and  $L = 3 \times 9$  is shown below.



250  
 251 **Figure S12.** Sampling the decorrelation noise based on phase PDF of distributed scatterers.  
 252 Blue bars: normalized histogram of sampled decorrelation noises. Orange and green solid line:  
 253 phase PDF and cumulative distribution function.



255

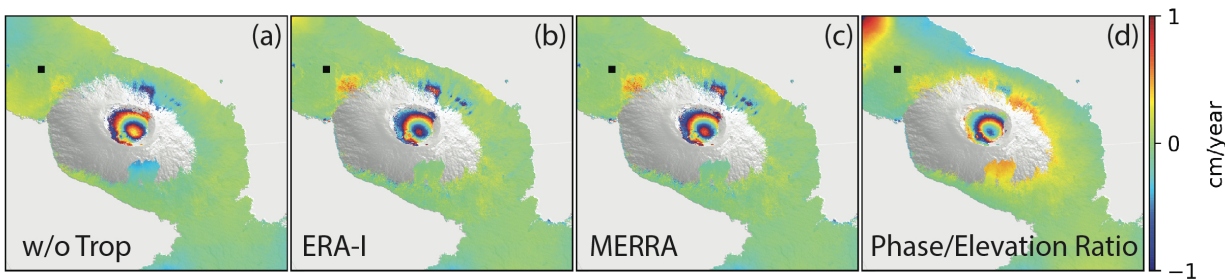
256 **Figure S13.** Time-series configuration for simulation. (a) Perpendicular baseline history from  
 257 the 98 Sentinel-1 images of section 5. (b) Specified time-dependent displacement used in section  
 258 2.4 and 3.2.

## 259 S4. Additional software features

### 260 S4.1 Customized workflow beyond `smallbaselineApp.py`

261 Most scripts in MintPy are stand-alone (summarized in Table S4). Users can apply any phase  
 262 correction at any time to evaluate the impact. Fig. S14 shows an example, where we use  
 263 individual scripts ([link on GitHub](#)) to compare velocities estimated from displacement time-  
 264 series with different tropospheric delay correction methods on Alcedo volcano.

265



266

267 **Figure S14.** Deformation velocity maps on Alcedo volcano from Sentinel-1 (a) without  
 268 tropospheric correction, with tropospheric correction using (b) ERA-Interim, (c) MERRA-2 and  
 269 (d) the empirical phase-elevation ratio method.

270

271 **Table S4.** Stand-alone scripts in MintPy

<code>add.py</code>	Generate the sum of multiple input files
<code>asc_desc2horz_vert.py</code>	Project ascending and descending displacement in LOS

	direction to horizontal and vertical direction
dem_error.py	DEM error (topographic residual) correction
diff.py	Generate the difference of two input files
generate_mask.py	Generate mask file from input file
geocode.py	Resample radar-coded files into geo coordinates, or vice versa.
ifgram_inversion.py	Invert network of interferograms into time-series.
image_reconstruction.py	Reconstruct network of interferograms from time-series
image_math.py	Basic mathematic operation of input file(s)
info.py	Display metadata / structure of input file
load_data.py	Load a stack of interferograms into HDF5 files
load_hdf5.py	Load the binary file(s) into an HDF5 file
local_oscillator_drift.py	Correct local oscillator drift for Envisat data
mask.py	Mask input data file with input mask file by setting values on the unselected pixels into Nan or zero.
match.py	Merge two or more geocoded files which share common area into one file.
modify_network.py	Modify the network setting of an ifgramStack HDF5 file.
multilook.py	Multilook input file.
plot_coherence_matrix.py	Plot the coherence matrix of one pixel, interactively.
plot_network.py	Plot the network configuration of an ifgramStack HDF5 file.
prep_gamma.py	Prepare metadata file for GAMMA files.

<code>prep_giant.py</code>	Prepare metadata file for GIAN T files.
<code>prep_isce.py</code>	Prepare metadata file for ISCE files.
<code>prep_roipac.py</code>	Prepare metadata file for ROI_PAC files.
<code>reference_date.py</code>	Change the reference date of a time-series HDF5 file.
<code>reference_point.py</code>	Change the reference pixel of an input file.
<code>remove_ramp.h5</code>	Remove phase ramps for input file.
<code>save_gmt.py</code>	Save input file in GMT *.grd file format.
<code>save_hdfeos5.py</code>	Save input time-series into HDF-EOS5 format.
<code>save_kmz.py</code>	Save input file into Google Earth raster image.
<code>save_kmz_timeseries.h5</code>	Save input file into Google Earth points, interactively.
<code>save_roipac.py</code>	Save input file into ROI_PAC style binary file format.
<code>select_network.py</code>	Select interferometric pairs from input baseline configurations
<code>smallbaselineApp.py</code>	Routine time series analysis for small baseline InSAR stack.
<code>spatial_average.py</code>	Calculate average in space domain.
<code>spatial_filter.py</code>	Spatial filtering of input file.
<code>subset.py</code>	Generate a subset of (crop) input file.
<code>temporal_average.py</code>	Calculate average in time domain.
<code>temporal_derivative.py</code>	Calculate the temporal derivative of displacement time-series.
<code>temporal_filter.py</code>	Smooth time-series in time domain with a moving Gaussian window

<code>timeseries2velocity.py</code>	Invert time-series for the average velocity.
<code>timeseries_rms.py</code>	Calculate the root mean square for each acquisition of the input time-series file.
<code>transect.py</code>	Generate/plot an transect/profile along a line of the input file.
<code>tropo_phase_elevation.py</code>	Correct stratified tropospheric delay based on the empirical phase/elevation ratio method.
<code>tropo_pyaps.py</code>	Correct tropospheric delay estimated from global atmospheric model (GAM) using PyAPS software (Jolivet et al., 2011; 2014).
<code>tsview.py</code>	Interactive time-series viewer.
<code>unwrap_error_bridging.py</code>	Correct phase-unwrapping errors with bridging method.
<code>unwrap_error_phase_closure.py</code>	Correct phase-unwrapping errors with the phase closure method.
<code>view.py</code>	2D matrix viewer.

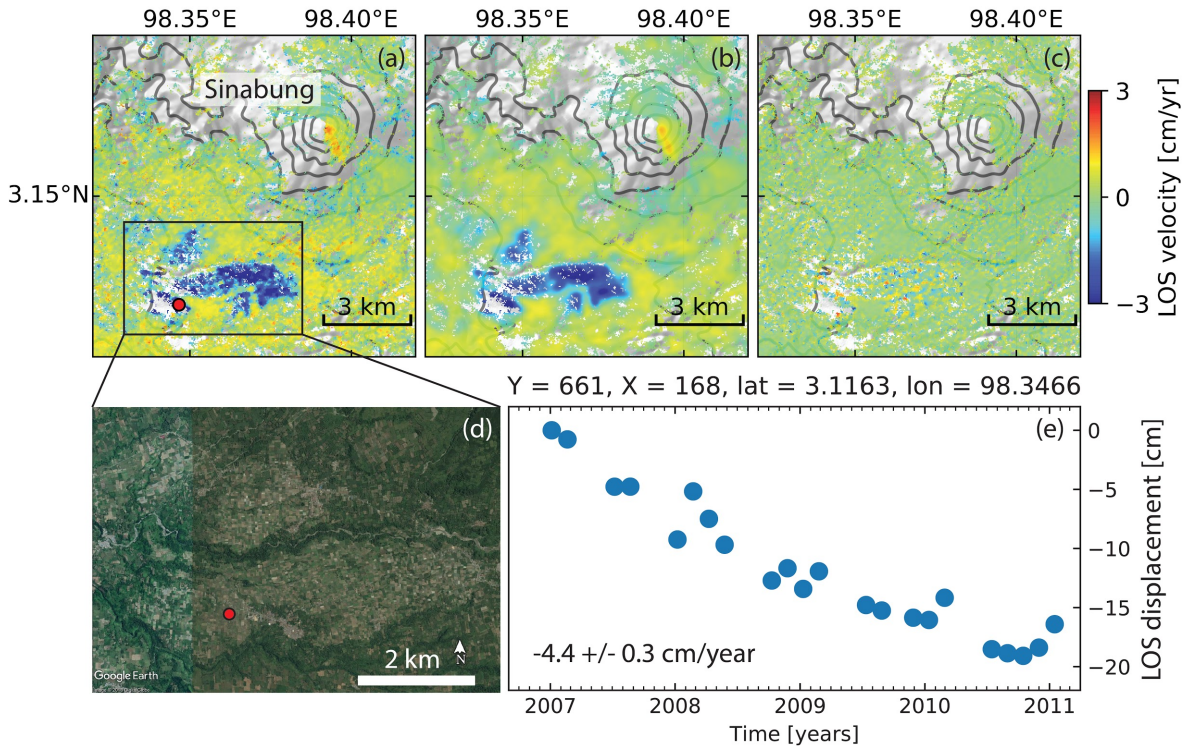
272

## 273 **S4.2 Filters tools in space and time domain**

274 The software supports filters in space or time domain built on skimage (van der Walt et al.,  
275 2014). Although filtering is not applied in the routine workflow, it is a useful tool to examine the  
276 deformation signal because it allows removing undesired signals. Fig. S15 shows an example,  
277 where we use spatial Gaussian filtering to confirm a patchy, rapid subsidence signal.

278





279

280 **Figure S15.** Illustration of the spatial filtering. The LOS velocity from ALOS-1 ascending track  
 281 495 acquired over Sinabung volcano, Indonesia during January 2007 to January 2011 is used.

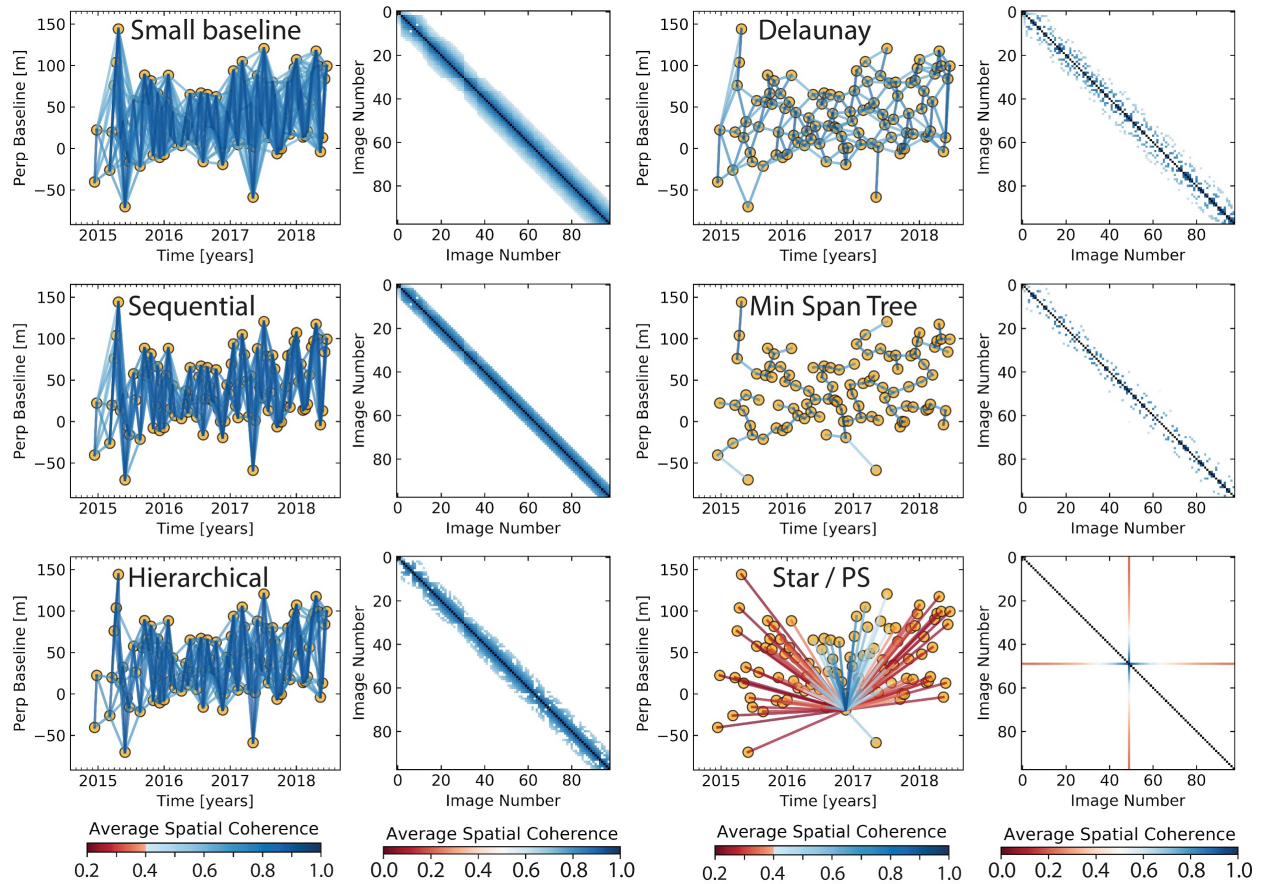
282 (a) Original velocity in LOS direction, (b and c) velocities after lowpass and highpass Gaussian  
 283 filtering with the standard deviation of 3.0. (a) is the sum of (b) and (c). The lowpass filtering  
 284 eliminated the very short spatial wavelength features, thus, highlighted the relatively long spatial  
 285 wavelength deformation features, such as the volcanic deformation along the Sinabung's  
 286 southeast flank and an undocumented patchy, rapid subsidence area (up to  $-5.6$  cm/year) is  
 287 found  $\sim 6$  km to the southwest of the volcano. The spatial pattern of the subsidence signal  
 288 correlates well with the agricultural land use, suggesting that subsidence is caused by  
 289 groundwater extraction (Chaussard et al., 2013). Reference point is a pixel at  $[E98.4999^\circ,$   
 290  $N3.1069^\circ]$  outside of this figure. (d) Google Earth image for the marked rectangle area. (e) LOS  
 291 displacement time-series for pixel marked by red circle in (a) at  $[E98.3466^\circ, N3.1163^\circ]$ .

292

293 **S4.3 Interferometric pairs selection**

294 The software supports several interferometric pairs selection methods to facilitate the pre-  
 295 processing, such as small baseline, sequential, hierarchical, Delaunay triangulation, minimum  
 296 spanning tree and star/PS-like methods, as shown in Fig. S16.

297



298

299 **Figure S16.** Illustration of interferometric pairs selection. The temporal and perpendicular  
 300 baselines are from Sentinel-1 dataset of section 5. For each method, network configuration on  
 301 the left and the corresponding coherence matrix on the right. The spatial coherence calculation  
 302 is described in section S3.1 with decorrelation rate of 200 days and long-term coherence of 0.2.  
 303 The small baseline method selects interferograms with temporal and perpendicular baseline  
 304 within the predefined thresholds (120 days and 200 m; Berardino et al., 2002). The sequential

305 *method selects for each acquisition with a predefined number (5) of its nearest neighbors back in*  
 306 *time (Reeves and Zhao, 1999). The hierarchical method specifies a predefined list of temporal*  
 307 *and perpendicular baselines as [6 days, 300 m; 12 days, 200 m; 48 days, 100 m; 96 days, 50 m],*  
 308 *each pair of temporal and perpendicular thresholds selects interferograms the same as small*  
 309 *baseline method (Zhao, 2017). The Delaunay triangulation method generates triangulations in*  
 310 *the temporal and perpendicular baseline domain and selects interferograms within the*  
 311 *predefined maximum temporal and perpendicular baseline (120 days and 200 m; Pepe and*  
 312 *Lanari, 2006). The minimum spanning tree method calculates a spatial coherence value based*  
 313 *on its simple relationship with the temporal and perpendicular baseline and selects N-1*  
 314 *interferograms that maximizes the total coherence (Perissin and Wang, 2012). The star-like*  
 315 *method selects network of N-1 interferograms with single common reference acquisition (usually*  
 316 *in the center of the time period; Ferretti et al., 2001).*

317

#### 318 **S4.4 Local oscillator drift correction for Envisat**

319 Data from Envisat’s Advanced Synthetic Aperture Radar instrument include a phase ramp in  
 320 range direction due to timing errors. We correct this local oscillator drift using the empirical  
 321 model given by Marinkovic and Larsen (2013).

322

$$323 \quad \phi_{LOD}^i = \frac{-4\pi}{\lambda} 3.87 \times 10^{-7} r(t_i - t_1) \quad (S16)$$

324

325 where  $(t_i - t_1)$  represents the time difference in years between SAR acquisition  $t_i$  and  $t_1$  (see  
 326 also Fattahi and Amelung, 2014). Since this model is independent of the InSAR phase  
 327 measurement, this correction should be applied before any InSAR data-dependent phase  
 328 corrections.

329 **Supplemental references**

330 Chaussard, E., F. Amelung, H. Abidin, and S.-H. Hong (2013), Sinking cities in Indonesia:  
331 ALOS PALSAR detects rapid subsidence due to groundwater and gas extraction, *Remote*  
332 *Sensing of Environment*, 128(0), 150-161, doi:10.1016/j.rse.2012.10.015.

333 Du, Y., L. Zhang, G. Feng, Z. Lu, and Q. Sun (2017), On the Accuracy of Topographic  
334 Residuals Retrieved by MTInSAR, *IEEE Transactions on Geoscience and Remote Sensing*,  
335 55(2), 1053-1065, doi:10.1109/TGRS.2016.2618942.

336 Marinkovic, P., and Y. Larsen (2013), Consequences of long-term ASAR local oscillator  
337 frequency decay - An empirical study of 10 years of data, paper presented at *Proceedings of*  
338 *the Living Planet Symposium (abstract)*, European Space Agency, Edinburgh, U. K.

339 Reeves, S. J., and Z. Zhao (1999), Sequential algorithms for observation selection, *IEEE*  
340 *Transactions on Signal Processing*, 47(1), 123-132, doi:10.1109/78.738245.

341 van der Walt, S., J. L. Schönberger, J. Nunez-Iglesias, F. Boulogne, J. D. Warner, N. Yager, E.  
342 Gouillart, and T. Yu (2014), scikit-image: image processing in Python, *PeerJ*, 2, e453,  
343 doi:10.7717/peerj.453.

344 Zhao, W. (2017), Small Deformation Detected from InSAR Time-Series and Their Applications  
345 in Geophysics, Dissertation thesis, 153 pp, University of Miami, Miami, FL.

346